2015

Advancements in evaluation of air-coupled impact-echo test method

Ji Lu
Iowa State University

Advancements in evaluation of air-coupled impact-echo test method

by

Ji Lu

A thesis submitted to the graduate faculty
in partial fulfillment of the requirements for the degree of
MASTER OF SCIENCE

Major: Civil Engineering (Geotechnical Engineering)

Program of Study Committee:
Jeramy C. Ashlock, Major Professor
Igor Beresnev
Kejin Wang

Iowa State University
Ames, Iowa
2015

TABLE OF CONTENTS

LIST OF TABLES

LIST OF FIGURES

ACKNOWLEDGMENTS

I would like to thank my advisor, Dr. Jeramy Ashlock, for his guidance, support, patience and his wisdom throughout my graduate study. His action shows me what an excellent advisor and dedicated researcher are. I am honored to be one of his students.

I would also like to thank Professors Igor Beresnev and Kejin Wang for serving on my thesis committee.

I would also like to thank Shibin Lin for his friendship, help and considerate suggestions for this study.

Much thanks to my parents, Yandong Lu and Yunzhi Liu for their great love, support and understanding.

This study was supported by the Mid-America Transportation Center, for which I am appreciative.

ABSTRACT

This report presents a study and accompanying laboratory work to investigate a recently-developed air-coupled impact-echo (IE) nondestructive testing (NDT) method, in which microphones replace the traditional physically-coupled IE sensors. To develop an optimum testing system and verify the new method, two concrete plates were tested in the laboratory, one of which was a solid concrete slab, and the other was a model of a reinforced concrete bridge deck with artificial defects. An IE testing system was developed using an Omega OMB-DAQ-3000 data acquisition module and a custom program written in LabVIEW. A measurement microphone was utilized as a sensor for the air-coupled test method, and two piezoelectric accelerometers were utilized for the traditional physically-coupled IE sensors. Prior to performing the IE tests, P-wave speeds were measured using the accelerometers according to ASTM specifications. The accuracy and feasibility of the air-coupled test method to determine the concrete structure's solid thickness and to detect defects or flaws, such as delaminations or voids, were verified by comparing test results obtained via the air-coupled and physically-coupled sensors.

The air-coupled IE method thus has the potential to increase the efficiency of IE testing of bridge decks and other concrete structures, by eliminating the need to physically couple and uncouple sensors for each test. However, when using the air-coupled IE method in practice, ambient noise generated by wind, traffic, and machinery will be sensed by the microphones and therefore reduce the signal to noise ratio of the data. Additionally, a portion of the acoustic energy generated by the impacts during testing will be lost due to the mismatch in acoustic impedance between concrete and air. To address these problems, a parabolic reflector and a sound isolation enclosure were studied and found to improve the quality of recorded signals

compared to using a microphone alone. Additionally, filtering techniques including band-pass, high-pass, and adaptive filters were implemented in MATLAB for post-processing the test data. Finite element method (FEM) based numerical simulations were conducted using COMSOL Multi-physics software to understand the mechanics of the air-coupled IE test, study the optimum geometry for the parabolic reflector, and investigate the effects of the microphone height. Finally, two-dimensional (2D) IE scanning tests were conducted on the bridge deck with artificial defects to locate the defect positions by the air-coupled and physically coupled test methods. Results obtained by these two methods are in good agreement, demonstrating the accuracy and feasibility of the air-coupled IE test method.

CHAPTER 1. INTRODUCTION

1.1 Overview of Impact-Echo Testing Method

Among various nondestructive testing (NDT) methods for concrete and masonry, the impact-echo (IE) method has become one of the most widely used for evaluating a structure's physical condition. The IE testing method is based upon the application of transient stress waves, where the main objective is to measure the thickness of concrete slabs or pavements, and locate cracks, voids, or delaminations in concrete structures such as bridge decks, post-tensioned structures, or foundation slabs. The basic notion behind IE testing is simple and straightforward; transient surface motions caused by transient resonance are excited by multiple reflections of stress waves between the testing surface and an external boundary. These reflections are recorded by vibration transducers and then transformed into the frequency domain to determine a structure's thickness (Sansalone and Carino 1986; Carino et al. 1986b; Sansalone and Streett 1997; Sansalone 1997; Carino 2001).

Dating back to the 1980s, the early success of the IE testing method benefited from four breakthroughs. First, two-dimensional models simulated by the finite element method (FEM) were employed to understand the mechanics of wave propagation during impact-echo tests of concrete structures, such as plate-like slabs or thick circular plates with and without artificial flaws (Sansalone et al. 1987a, 1987b; Sansalone and Carino 1987; Cheng and Sansalone 1993a). Second, qualified stress waves were generated by tapping a small steel sphere against a structure's surface with a short duration impact (15 to 80 ms). Such impact-generated stress waves have the desired frequency range and sufficient energy to

penetrate concrete structures, which can go to 1.5m (Sansalone and Carino 1986; Carino et al. 1986b; Sansalone 1997). Third, in the early development of the IE testing method, using a sensitive receiving transducer with a broadband frequency range developed by Proctor (1982) was able to detect surface motions caused by stress waves. Fourth, the final breakthrough resulted from an interpretation of testing results in the frequency domain instead of the time domain. A Fourier transform is employed to transform the time domain signal into a frequency domain. It was determined interpreting test results in the frequency domain was much easier than in the time domain due to the complexity and inherent difficulties of time domain waveforms (Carino et al. 1986b).

Theoretical research by Gibson and Popovics (2005) indicated the transient resonance of the IE test is actually related to leaky lamb waves with the S_1 mode, which have zero-group-velocity in the air field. Furthermore, there are studies by Zhu and Popovics (2002), Zhu et al. (2004), Zhu (2005), Ryden et al. (2006), and Zhu and Popovics (2005) that demonstrated physically-coupled sensors can be replaced by air-coupled sensors in IE testing. Although the physically-coupled testing method is determined as an accurate and reliable method, it is a time-consuming, labor-intensive method due to the requirement of coupling the sensor to testing surface. Studies by Zhu (2005) and Zhu and Popovics (2007) showed equivalent and sometimes even superior results can be obtained by utilizing the air-coupled testing method. For example, the air-coupled sensor microphone with a broadband frequency range is more capable of detecting shallow delaminations compared with the physically-coupled sensor accelerometer. Additionally, acoustic energy will be lost due to mismatched acoustic impedance between air and

concrete. Meanwhile, ambient noise will become involved when the air-coupled testing method is utilized. In terms of acoustic energy loss and ambient noise, lab testing by Dai et al. (2011) and the finite element method (FEM) based on a numerical simulation analysis by Kee et al. (2012) proved the parabolic reflector can enhance a signal's quality by focusing energy at its focal point and blocking the ambient noise as well.

1.2 Scope of This Study

As mentioned previously, the physically-coupled IE testing method is relatively time-consuming and labor-intensive. The efficiency of the IE test can be greatly improved and a signal's quality can be enhanced when the air-coupled testing method is used in conjunction with a parabolic reflector. To advance the technique for the air-coupled impact-echo (ACIE) testing system, the goal of this study is to evaluate the accuracy and feasibility of the air-coupled, impact-echo testing method by comparing test results of defect-free concrete plates and concrete plates with artificial defects using the physically-coupled testing method.

Equipment used to implement physically, air-coupled testing is described in Chapter 2. Additionally, written in LabVIEW for data acquisition a custom-built computer program is introduced as well. Chapter 3 reports a comprehensive understanding of the basic theory behind the impact-echo's test. Signal processing issues, such as crosstalk during data acquisition and solution, are also reported. Chapter 4 provides a computationally, finite element method (FEM) based numerical simulation analysis completed in COMSOL Multiphysics software. This aims to understand an air-coupled impact-echo's response to a parabolic reflector and develop the optimum geometry for the

parabolic reflector. Chapter 5 reports the test results obtained by the air-coupled testing method on both test concrete plates. The same tests were conducted by the physically-coupled testing method for comparison purposes. By using the air-coupled testing method to locate the position of artificial defects in the concrete plate, a two-dimensional (2D) scan test was completed. For verification accuracy and feasibility of the air-coupled testing method, half of the defects were scanned using the physically-coupled sensor accelerometer. Additionally, application of a filtering technique to signal processing of impact-echo's test is discussed. Chapter 6 concludes with a discussion of the conclusions and recommendations for future studies.

CHAPTER 2. EXPEERIMENTAL SETUP AND EQUIPMENT

2.1 Accelerometers for Physically-Coupled Impact-Echo Tests

The development of a specialized broadband piezoelectric sensor with a conical tip to record the displacement of the concrete surface during testing was one of the major breakthroughs in the development of the impact-echo method in the 1980s (Sansalone 1997, Proctor 1982). More recently, several researchers have also used conventional off-the-shelf piezoelectric accelerometers with good results. For measuring the P-wave speed of the concrete, transducers for IE testing should have high sensitivity and low noise to be able to detect small displacements normal to the surface, caused by the Poisson effect for P-waves with particle displacements parallel to and propagating along the surface. As required by ASTM C 1383, individual tests are deemed invalid if the sensor signals contain excessive electrical noise.

Figure 2.1. PCB model 621B51 (left) and 353B33 (right) piezoelectric accelerometers used in this study.

For this study, PCB model 621B51 and 353B33 piezoelectric accelerometers were used to record signals for both the P-wave speed measurement test and the traditional

impact-echo test with physically-coupled sensors (Figure 2.1). The accelerometers are connected by special low-noise, low-capacitance cables (PCB model 003C) to a PCB model 480B21 battery-powered signal conditioner, which in turn is connected by RG-58 coaxial cable with BNC connectors to the data acquisition device. Both of these accelerometers have low electrical noise and fixed voltage sensitivity, which provides a stable signal output for data recording and signal processing. The main performance characteristics of these two accelerometers are summarized in Table 2.1.

Table 2.1. Main performance characteristics of accelerometers.

	Model Number			
	621B51		**353B33**	
Characteristic	**ENGLISH**	**SI**	**ENGLISH**	**SI**
Sensitivity: (±5%)	100mV/g	10.2mV/(m/s^2)	100mV/g	10.19mV/(m/s^2)
Frequency Range: (±5%)	2.4 – 10,000 Hz	2.4 – 10,000 Hz	1 – 4000 Hz	1 – 4000 Hz
Frequency Range: (±3 dB)	0.8 – 20,000 Hz	0.8 – 20,000 Hz	0.35 – 12,000 Hz	0.35 – 12,000 Hz
Measurement Range	±50g	±490m/s^2	±50g	±490m/s^2
Electrical Connector:	10 – 32 Coaxial Jack	10 – 32 Coaxial Jack	10 – 32 Coaxial Jack	10 – 32 Coaxial Jack

The procedures of ASTM C 1383 were followed for P-wave speed measurements using the setup shown in Figure 2.2. For the P-wave speed measurement test, the two accelerometers are attached to the concrete surface 0.3 m apart. The vertical accelerations due to the impact of a small steel sphere 0.15±0.01 m from the first accelerometer are then

recorded and the travel time between the two accelerometers is determined from the P-wave first arrival times. While both accelerometers were used for the P-wave speed measurement tests, the model 621B51 has a higher frequency range and it was therefore used in the impact-echo tests.

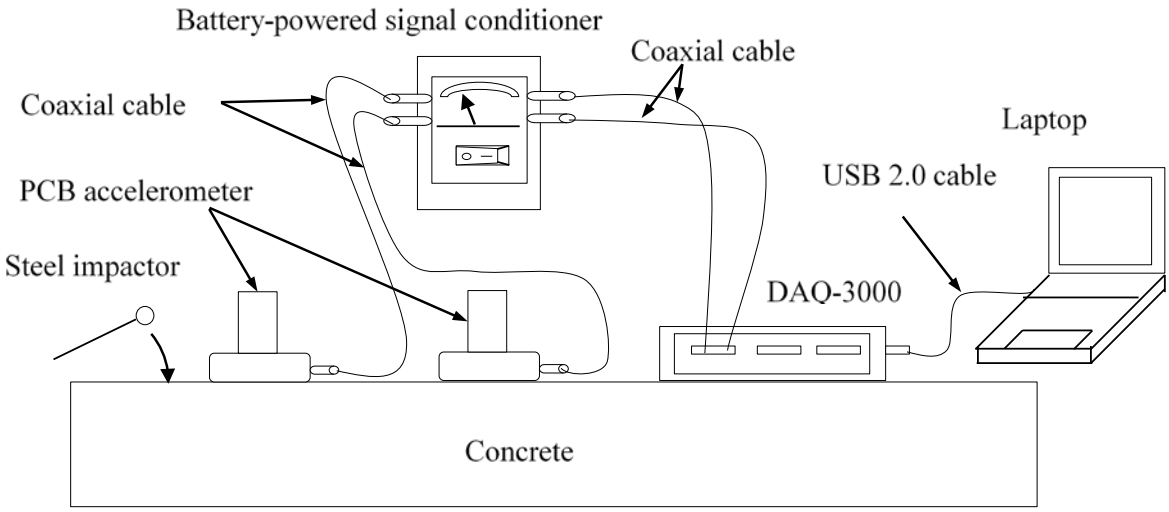

Figure 2.2. Schematic diagram of P-wave speed measurement test using physically-coupled accelerometers.

For traditional impact-echo tests, only one accelerometer needs to be physically coupled to the testing specimen's surface. As specified in ASTM C 1383, it should be located from the impactor a distance less than 40% of the estimated nominal thickness of the concrete slab. Small vertical displacements caused by multiple reflections of stress waves within the specimen due to the impactor are then recorded. The same data acquisition system used for the P-wave speed measurement was used for the impact-echo tests. Figure 2.3 shows the schematic diagram for using a single physically-coupled accelerometer for the traditional impact-echo test.

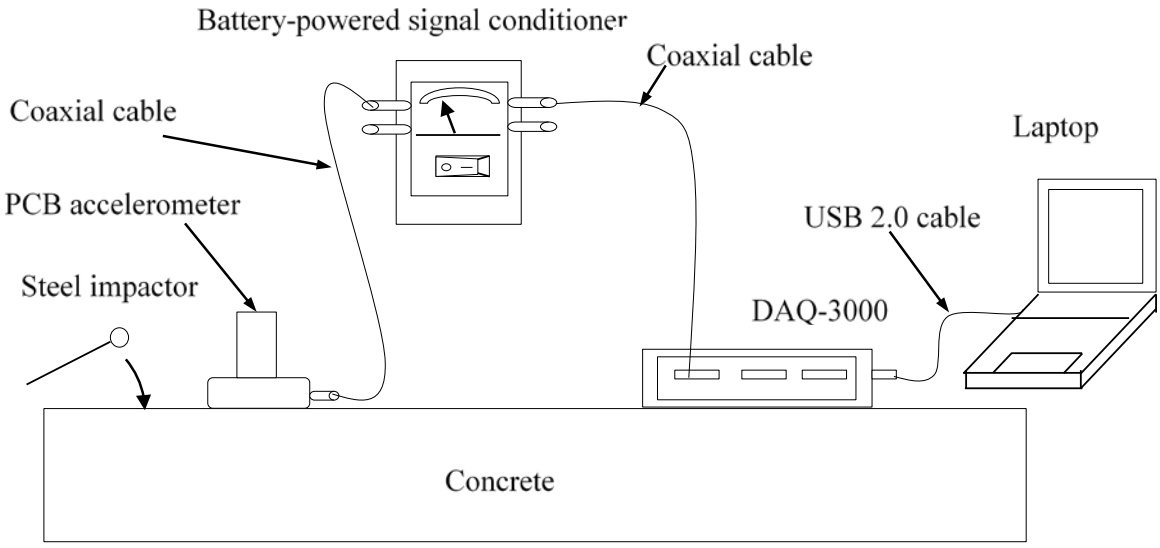

Figure 2.3. Schematic diagram of traditional impact-echo test with physically-coupled accelerometer.

As discussed in this section, sensors are typically physically coupled to the surface of the concrete structure for impact-echo testing. However, the selected mounting technique can directly affect the accuracy of testing results. A small, void-free contact interface is required between the base of the sensor and testing surface to detect wave propagation along the concrete surface. Therefore, using an appropriate materials and methods for coupling can significantly affect the success of the tests. Coupling can be achieved in several ways, including using hand probes, adhesive mounting, and stud mounting. For the physically-coupled sensors in this study, an adhesive mounting method using high vacuum grease was utilized. The high vacuum grease provides good coupling and void-sealing ability and can be easily removed by a rag or paper towel. A small amount of high vacuum grease was applied uniformly to the sensor's base, then the sensor was directly mounted on the testing surface (Figure 2.4).

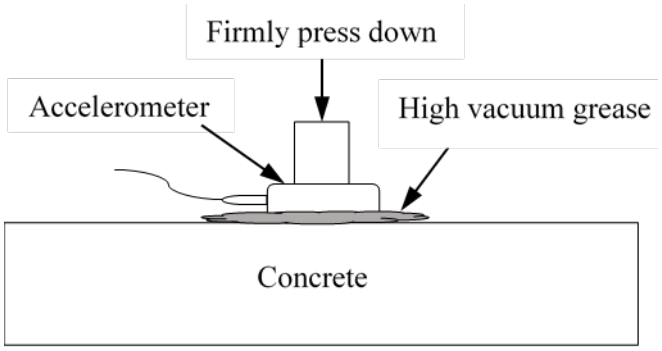

Figure 2.4. Adhesive mounting method using high vacuum grease for physically-coupled accelerometers.

2.2 Microphone for Air-coupled Impact-Echo Tests

The physically-coupled testing method described in the previous section is relatively inefficient and labor-intensive because the sensor must be physically coupled to the desired point on the surface of the testing specimen, then uncoupled and moved for the next test. The air-coupled impact-echo (ACIE) testing method, previously developed for improving the efficiency of impact-echo tests, was further investigated in this study by computational and experimental approaches.

Application of air-coupled sensors for contactless nondestructive testing was established for testing of metal plates in the 1970s (e.g., Luukkala and Meriläinen 1973). Recently, the air-coupled testing method for IE test on concrete can be achieved with high-quality acoustic transducers that have high accuracy and broadband frequency range. However, signals and results obtained by the technique were not always consistent and reliable because of significant loss of acoustic energy resulting from huge acoustic impedance difference between concrete and air as well as the limited sensitivity of air-coupled sensors (Zhu and Popovics 2002, Kee et al. 2012). Recent studies proved, in theory, that the transient resonance of the impact-echo's test was related to leaky S_1 mode

Lamb waves, which have zero-group-velocity (referred as S_1 ZGV) in the airfield. These waves can be detected through an air-coupled sensor, such as a microphone (Gibson and Popovics 2005, Zhu 2005).

A high-accuracy PCB model 378C01 pre-polarized free-field measurement microphone with preamplifier was employed as an air-coupled sensor for impact-echo tests in this study (Figure 2.5). The microphone is 0.25 in. (6.4 mm) in diameter and 2.07 in. (52.6 mm) in length, and has a nominal open circuit sensitivity of 2.0 mV/Pa and dynamic range greater than 162 dB. The microphone is powered by the PCB model 480B21 battery-powered signal conditioner detailed in the following section, and connected by RG-58 coaxial cable with BNC connectors. It has a broadband frequency range from 4 to 80,000 Hz at ±2 dB to provide highly accurate measurements of the acoustic pressure caused by the leaky S_1 mode Lamb waves in impact-echo testing. Figure 2.6 shows the schematic diagram for using the microphone as the sensor for the air-coupled impact-echo test.

Figure 2.5. PCB model 378C01 microphone used as air-coupled sensor.

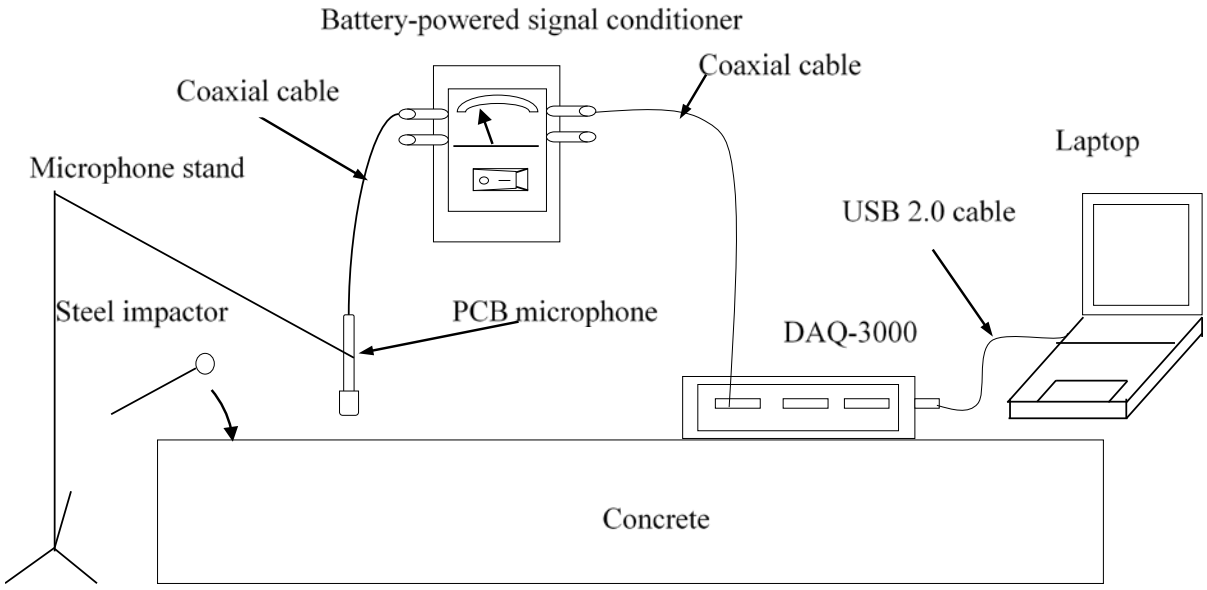

Figure 2.6. Schematic diagram of using microphone for air-coupled impact-echo test.

Zhu (2005) demonstrated that a broadband microphone could successfully be used in impact-echo tests to detect shallow delaminations in concrete in accordance with the higher frequencies recorded. Although use of an air-coupled sensor in impact-echo testing offers several advantages, it also creates several other problems. First, ambient environmental noise such as wind or traffic noise can be recorded along with and overshadow the desired acoustic signal. As a result, identification of the appropriate peak in the frequency domain corresponding to the concrete or defect depth becomes more difficult (Tinkey and Olson 2010, Dai et al. 2011). Additionally, the low acoustic impedance of air relative to concrete results in loss of energy of the leaky waves emitted from the concrete surface and captured by the air-coupled sensor (Kee et al. 2012).

The air-coupled impact-echo testing results for a solid concrete slab used for calibration and a concrete slab with artificial defects will be reported and analyzed in the experimental results section of this thesis.

2.3 Data Acquisition System

The data acquisition system is composed of both hardware and software to acquire, record, process, and export data recorded by the accelerometers and microphone. The system consists of a PCB battery-powered sensor signal conditioner, an Omega 1-MHz 16-bit data acquisition module (commonly referred to as a DAQ), and a program developed for this study using LabVIEW software. Detailed descriptions of each component of the data acquisition system are provided in the ensuing sections.

2.3.1 Battery-powered sensor signal conditioner

As mentioned previously, a PCB Model 480B21 battery-powered signal conditioner (Figure 2.7) served as a constant current excitation source, voltage amplifier, and signal conditioner for both the piezoelectric accelerometers and microphone in this study. The signal conditioner connects to the sensors and DAQ through RG-58 coaxial cables with BNC connectors. It is powered by three 9-volt batteries which also provide the 2 mA constant current necessary for powering the piezoelectric sensors. In addition to indicating the battery status, the meter at the top of the unit also indicates the presence of a short circuit condition in the red zone, or an open circuit in the yellow zone. In addition, amplification factors can be adjusted to 1, 10, and 100 using the voltage gain position selector switch.

Figure 2.7. PCB model 480B21 battery-powered sensor signal conditioner.

2.3.2 Data Acquisition Module

A model OMB-DAQ-3000 USB data acquisition system manufactured by OMEGA Engineering Inc. featuring a 16-bit resolution and 1 MHz maximum sampling rate was used for data acquisition (Figure 2.8). The device was controlled by the custom-built program written in LabVIEW. Although the DAQ can be powered via the laptop's USB port, an optional external power supply can be used if adequate power cannot be supplied by the laptop's USB port. The DAQ provides 16 single-ended or 8 differential analog inputs and 2 analog voltage outputs. The single-ended or differential modes can be selected in the LabVIEW program. In single-ended mode, the voltage is measured between one input channel and common ground voltage. In differential mode, voltage is measured between two input channels and ground. Although the single-ended mode is easier to set up and

saves connector space, the differential mode configuration is preferred in this study because it can help reduce common-mode electrical noise caused by ground current.

Triggering is one of the most critical aspects for any data acquisition system intended to capture short duration transient phenomena. In this study, both P-wave speed measurements and impact-echo tests make use of hardware analog triggers in the OMB-DAQ-3000. In the custom-built LabVIEW program, any of the analog input channels of the DAQ can be assigned as a trigger channel. The trigger configuration, such as trigger type, polarity, and threshold, can also be specified.

Although noise can be reduced to some level by using differential mode, another type of noise should be noted and suppressed in the P-wave speed measurement test, which is crosstalk. Crosstalk is a type of interference caused by signal leakage from one channel into an adjacent channel. It is related to the source impedance and capacitance of the multiplexed DAQ channels. One method to reduce crosstalk is to use oversampling, whereby samples are recorded at a much higher rate than needed and then averaged. However, this method could not be used in this study, because it was necessary to retain the maximum sampling rate possible. As an alternative method to reduce the crosstalk between the two accelerometer channels during P-wave speed measurement, a third additional channel was shorted to ground and scanned between the two accelerometer channels, with all three channels wired in differential mode. This solution comes at a cost of reducing the effective sampling rate for the two accelerometers from 500 kHz to 333.3 kHz per channel. More details on the crosstalk issue and methods used to suppress its effects will be presented in Chapter 3.

Figure 2.8. Omega OMB-DAQ-3000 1-MHz, 16-bit data acquisition system.

2.3.3 LabVIEW Control Program

As mentioned previously, a custom-built program was written in LabVIEW for this study. The program is used to acquire, process, and export testing data, and to configure the acquisition parameters such as the sampling rate, sampling length, trigger type, and trigger level. The front panel for this program, shown in Figure 2.9, is divided into the settings section on the left side and the data display section on the right. Acquisition parameters such as scan rate, total scans to acquire, analog input channel numbers, and trigger channel can be set and assigned in the settings section. Once acquisition parameters are set and a test is performed, the signal's waveform captured by the sensor will be presented in the display section, including the time domain representation and frequency

domain representation (magnitude and phase). Additionally, a vertical toggle switch and an indicator on the front panel are designed to allow for easily converting from P-wave speed measurement to impact-echo testing.

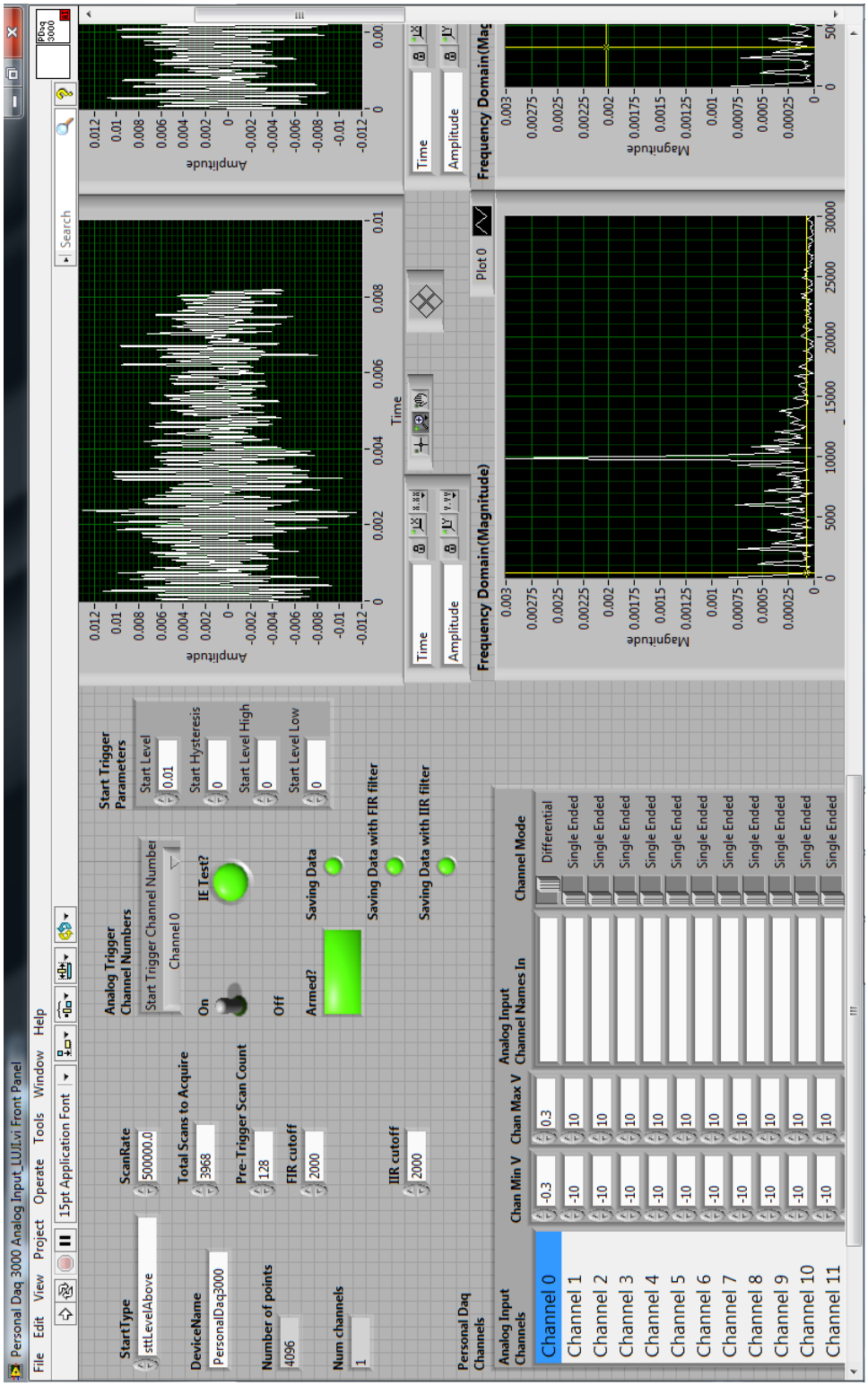

Figure 2.9. Front panel of the LabVIEW control program for the impact-echo test.

2.4 Impactors

Both the P-wave speed measurement and the impact-echo test make use of impact-generated stress waves. Tapping small steel spheres of different sizes against the surfaces of concrete can generate elastic stress waves with characteristics useful for impact-echo testing of structural members up to 1.5 m thick (Sansalone and Streett 1997). The properties of the stress waves, including the impulse duration and frequency range possessing sufficient energy for impact-echo measurement are a function of the size of the impactor. Specifically, the diameter of the steel sphere is inversely proportion to the maximum useful frequency of the impact-generated elastic stress waves (Sansalone 1986, Sansalone and Carino 1986). As a result, selection of a steel sphere with an appropriate diameter determines the accuracy of the testing results. The theory of stress waves propagating through a solid will be elaborated in Chapter 3.

A set of small steel spheres of various diameters with attached spring-steel rods were used to generate the elastic stress waves for both P-wave speed measurement and impact-echo tests in this study (Figure 2.10). The diameters of the spheres range from 3 to 8 mm for the smaller set and 10 to 19 mm for the larger set. For reference, the diameters of commonly-used ball bearings for impact-echo tests typically ranges from 4 to 15 mm (Sansalone and Streett 1997).

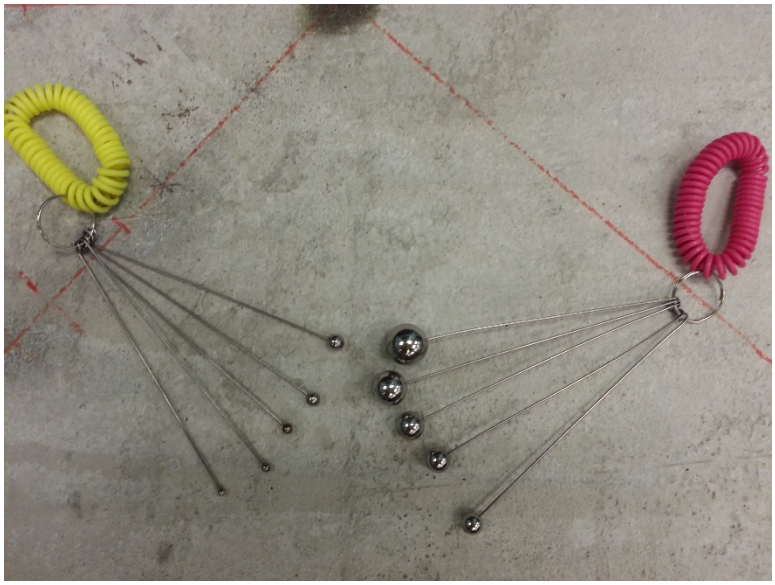

Figure 2.10. Steel spheres of different diameters used for impact-echo tests in this study.

2.5 Parabolic Reflector and Sound Isolation Enclosure

A parabolic dish was recommended for use as a reflector for microphones at high frequencies starting in 1930 (Olson and Wolff 1930). Later, Wahlström (1985) showed that plane acoustic waves can be amplified at the focus of parabolic reflectors and studied the directivity and influence of material type on performance.

As discussed in the preceding section, when performing air-coupled impact-echo tests in the field, undesirable ambient noise will be captured along with the desired signals. On one hand, the mathematical and physical theories indicate that any incident acoustic waves which are parallel to the axis of symmetry will be gathered at the focus after being reflected by the parabolic reflector's surface. Therefore if the reflector alone is aimed at the concrete surface and the microphone's sensing diaphragm placed at the reflector's focus, the signal obtained by the microphone due to the leaky waves can be amplified. On the other hand, recent studies demonstrated that surrounding the space between the

reflector and test surface with foam can reduce acoustic energy loss as well as ambient noise. Energy carried by leaky waves can then be sustained relatively longer because of multiple reflections produced between the reflector and testing surface (Dai et al. 2011, Kee et al. 2012). As a result, well-defined waveforms can be obtained in the air-coupled impact-echo test. Finally, studies by Zhu and Popovics (2007) showed that good results can be obtained when a simple sound isolation enclosure is employed. Thus, use of either a parabolic reflector with foam or a sound isolation enclosure can successfully suppress and block acoustic noise and direct acoustic waves from ambient sources (Zhu 2005, Zhu and Popovics 2007, Dai et al. 2013).

Equipment used to reduce ambient noise in this study is shown in Figure 2.11. This includes an off-the-shelf parabolic reflector fitted with a custom-fabricated microphone mount (Figure 2.11a), a noise-blocking foam annulus (Figure 2.11b), and a separate sound isolation enclosure constructed of stiff rubber pads surrounded by foam blocks (Figure 2.11c and 2.11d). The parabolic reflector is placed on the top of the foam annulus and secured using silicon sealant. The microphone mount is attached to the reflector using threaded spring-steel rods, which are in turn welded to a central ring through which three plastic-tipped steel setscrews are threaded to secure the microphone. Air-coupled impact-echo testing results using this equipment will be presented in Chapter 5.

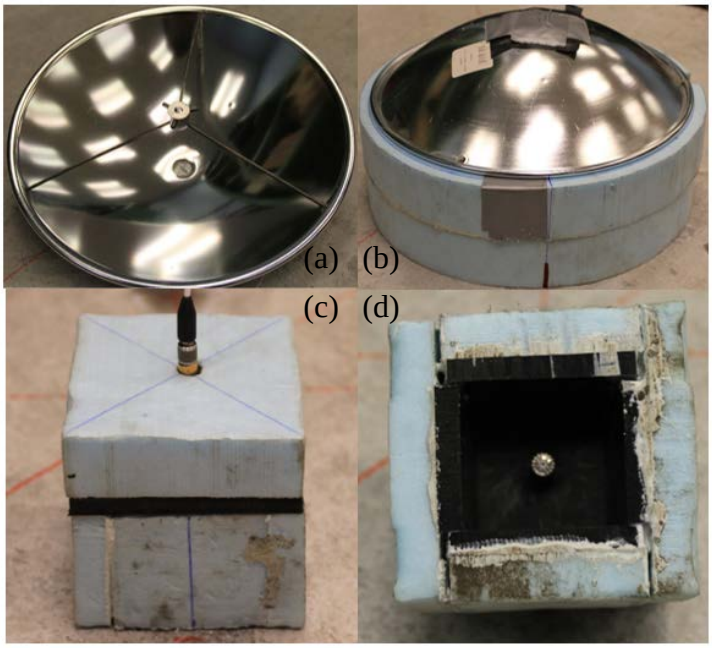

Figure 2.11. Equipment used to reduce noise: (a) parabolic reflector with microphone mount; (b) parabolic reflector with foam annulus; (c) and (d): rubber and foam sound isolation enclosure.

CHAPTER 3. THEORY OF IMPACT-ECHO TEST METHODS

Since its introduction in the 1980s, impact-echo (IE) testing has become one of the most widely used nondestructive testing (NDT) methods (Carino et al. 1986b, Sansalone 1997). IE testing is typically performed on concrete and masonry structures to detect delaminations or voids according to the behavior of transient stress waves. An understanding of the fundamentals of wave propagation is indispensable for proper interpretation of test results. This chapter is aimed at introducing the mechanics of the generation and propagation of stress waves in impact-echo testing. Furthermore, this chapter also presents aspects of signal processing necessary for proper instrument configuration, and procedures to minimize crosstalk in the data acquisition system. Frequency analyses, including the Fast Fourier Transform (FFT) and two different numerical integration methods, are discussed and compared as well. The information in this chapter provides a good understanding of the testing configuration and the recorded impact-echo response in the time and frequency domains.

3.1 Propagation of Transient Stress Waves

In impact-echo testing, surface motion caused by transient resonance excited by multiple reflections of stress waves within plate-like structures is used to determine the structure's thickness, or indicate the presence and depth of internal flaws (Sansalone and Carino 1986). Generation of stress waves with the appropriate energy and frequency content is a key determinant of whether impact-echo testing can be performed successfully. Classical impact theory considers the collision of any two or more rigid bodies. However, this theory is inappropriate for the description of transient stresses and deformations in

elastic bodies (Goldsmith 1965), such as those caused by impacts of steel balls against large concrete plates with suitably short impact durations of 15 to 80 ms (Sansalone and Carino 1986, Sansalone and Streett 1997, Sansalone 1997).

For an impact-echo test, the elastic stress waves are typically generated by tapping hardened steel spheres with diameters ranging from 3 to 8mm against the surface of concrete. Once such an impact is performed, body waves and surface waves will propagate along spherical and cylindrical wave fronts, respectively. Body waves include compression waves (primary or P-waves) and shear waves (secondary or S-waves). For an impact normal to the surface, Rayleigh waves (R-waves) will also propagate near the surface. A schematic representation of the P-, S-, and R-waves caused by tapping a steel sphere against the surface of a solid is shown in Figure 3.1. The particle motion is parallel to the direction of wave propagation for P-waves, and perpendicular to the direction of wave propagation for S-waves. For R-waves, the particle motion has both vertical and horizontal components, which result in an elliptical particle motion that is retrograde at the surface and transitions to prograde below some depth.

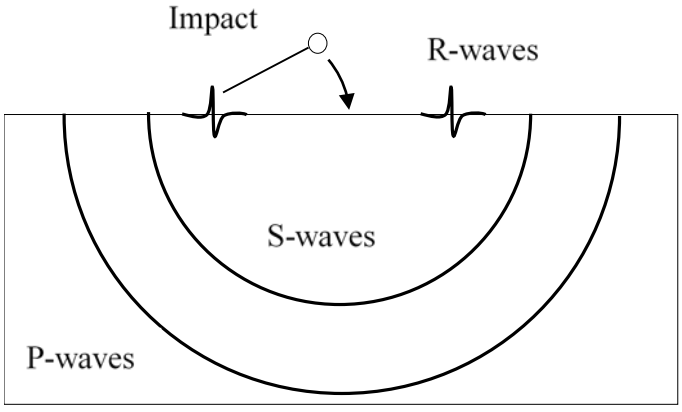

Figure 3.1. Schematic representation of stress waves due to impact propagating in concrete plate (after Carino 2001)

Previous studies have demonstrated that directly under the impact point, the resonant vertical surface displacements caused by multiple reflections of the P-waves from the boundaries are greater than the displacements caused by S- and R-waves in impact-echo tests (Sansalone and Carino 1986, Sansalone and Streett 1997, Schubert and Köhler 2008). A snapshot of stress waves propagating in a concrete plate due to an impact at the upper surface is shown in Figure 3.2, obtained from a finite element method (FEM) simulation performed for this study using COMSOL Multiphysics software. In the figure, the initial P-wave front has just been reflected by the lower surface and is returning to the upper surface. Low-reflecting boundaries were used on the left and right sides to model a plate of infinite width by minimizing reflections. In the snapshot, the S-waves are still propagating towards the lower surface and side boundaries, and R-waves are propagating near the concrete surface.

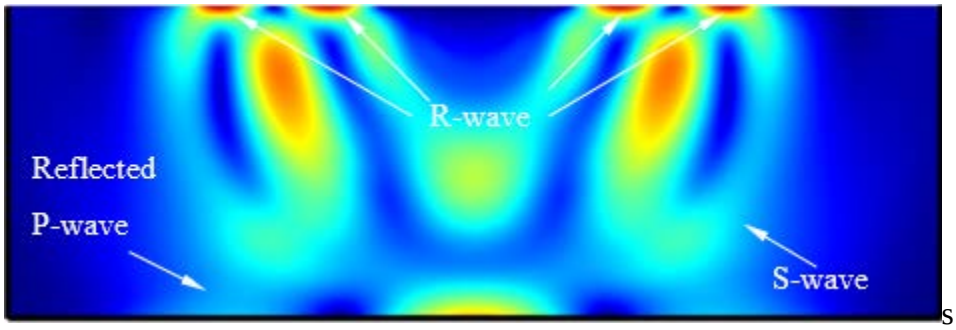

s

Figure 3.2. Snapshot of impact-echo response of concrete plate by FEM simulation (von Mises stress shown).

In general, the wavelength, wave speed, and frequency of propagating waves can be related through the expression:

$$C = f \cdot \lambda \tag{3.1}$$

where C is the wave speed (phase velocity), f is the frequency, and λ is the wavelength.

For stress waves propagating through a homogeneous, infinite, elastic body, the wave speeds can be expressed as a function of three elastic properties, such as Young's modulus, mass density, and Poisson's ratio (Krautkrämer and Krautkrämer 1990). The P-wave speed is denoted C_p, and can be expressed as

$$C_p = \sqrt{\frac{E(1-\nu)}{\rho(1+\nu)(1-2\nu)}} \tag{3.2}$$

where E is the Young's modulus of elasticity, and ν and ρ are the Poisson's ratio and mass density of the body, respectively. The S-wave speed C_s can be expressed as

$$C_s = \sqrt{\frac{G}{\rho}} \tag{3.3}$$

where G is the shear modulus, which can be related to the Young's modulus through

$$G = \frac{E}{2(1+\nu)} \tag{3.4}$$

Using Eqs. (3.2) and (3.3), the S-wave speed can also be expressed as

$$C_s = \sqrt{\frac{E}{2\rho(1+\nu)}} \tag{3.5}$$

From Ens. (3.2) and (3.5), the ratio between S- and P-wave speeds can be expressed as a function of Poisson's ratio:

$$\frac{C_s}{C_p} = \sqrt{\frac{1-2\nu}{2(1-\nu)}} \tag{3.6}$$

The Rayleigh wave speed is smaller than the S-wave speed. For a given Poisson's ratio, one can solve for the roots of the characteristic Rayleigh wave equation, or use the following closed-form approximation (Viktorov 1967):

$$\frac{C_R}{C_S} = \frac{0.87+1.12\nu}{1+\nu} \tag{3.7}$$

A commonly used value of Poisson's ratio for concrete is 0.18 (Lin and Sansalone 1997, Sansalone and Streett 1997), which can be substituted into Eqs. (3.6) and (3.7) to determine the relative P-, S-, and R-wave speeds. For ν=0.18, these equations indicate that the S-wave speed is 62% of the P-wave speed, and the R-wave speed is 91% of the S-wave speed, which is equivalent to 57% of the P-wave speed. Therefore, the P-wave propagates in the solid at the maximum speed and arrives at the sensor first, followed by the S-waves and R-waves.

When impact-generated stress waves propagate through solids, the waves may encounter interfaces between two media having dissimilar properties, such as a solid/air interface, or solid/soil interface. When the stress waves strike the interface, reflected and

refracted waves are produced. According to Snell's law, the relationship between the incident and refracted waves can be written as:

$$\frac{\sin\theta_i}{\sin\theta_{rfr}} = \frac{C_1}{C_2} \tag{3.8}$$

where θ_i is the angle between the incident wave and the normal to the interface, θ_{rfr} is the angle of the refracted wave, C_1 is the speed of the incident wave, and C_2 is the speed of the refracted wave, as shown in Figure 3.3a.

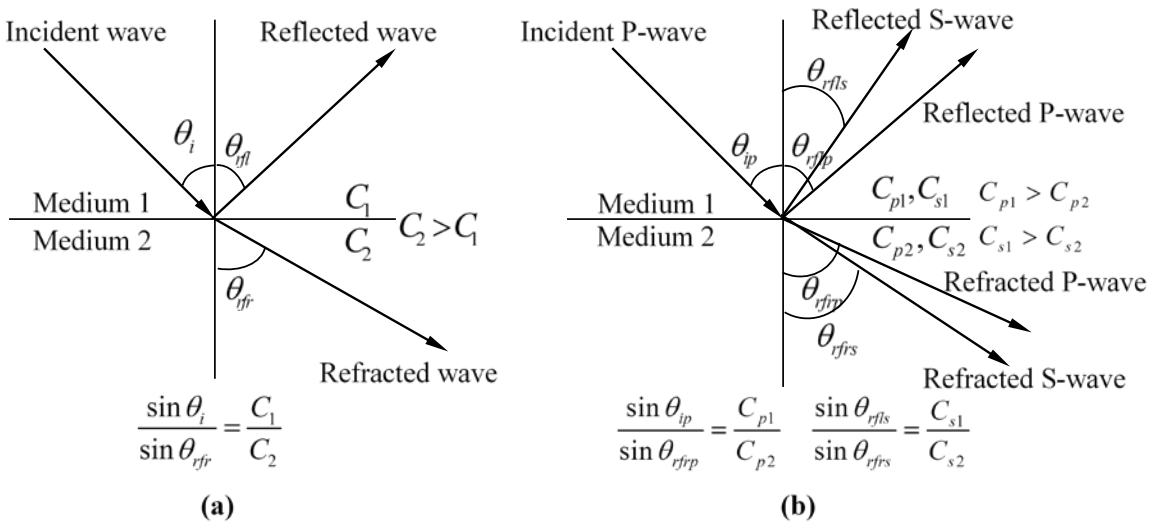

Figure 3.3. Schematic illustration of Snell's law: (a) incident wave striking interface between dissimilar media; (b) mode conversion whereby incident P-wave results in reflected and refracted P- and S-waves.

As mentioned previously, the impact-echo testing method is mainly dependent upon propagation and multiple reflections of P-waves in solids. When a P-wave is incident on the interface, it will produce both reflected and refracted P- and S-waves in the two media as shown in Figure 3.3b (see e.g., Burger et al. 2006), which can be related through

$$\theta_{rflp} = \theta_{ip} \tag{3.9}$$

$$\frac{\sin\theta_{ip}}{\sin\theta_{rfrp}} = \frac{C_{p1}}{C_{p2}} \tag{3.10}$$

$$\frac{\sin\theta_{rfls}}{\sin\theta_{rfrs}} = \frac{C_{s1}}{C_{s2}} \tag{3.11}$$

and

where θ_{ip} is the angle of the incident P-wave, θ_{rflp} is the angle of the reflected P-wave, θ_{rfls} is the angle of the reflected S-wave, θ_{rfrp} is the angle of the refracted P-wave, θ_{rfrs} is the angle of the refracted S-wave, C_{p1} and C_{p2} are the P-wave speeds in medium 1 and 2, respectively, and C_{s1} and C_{s2} are the corresponding S-wave speeds in the two media. Similarly, an incident vertically polarized S-wave (SV-wave) will lead to reflected and refracted SV- and P-waves, but an incident horizontally polarized SH-wave will result in only reflected and refracted SH-waves, with no mode conversion to P-waves. Note that a surface impact on a plate in air will lead to multiple reflections and mode conversions along ray paths inclined from the axis normal to the upper and lower interfaces, but the P-waves incident normal to the interfaces are of primary interest in impact-echo testing.

For an incident P-wave, Zoeppritz's (1919) equations can be used to quantify the amplitudes of reflected and refracted P- and S-waves relative to that of the incident P-wave. A simplified form of Zoeppritz's equation can be derived for the case of a P-wave incident

normal to the interface. The amplitude of the reflected wave is largest for this case, because no S-waves will result (Sheriff and Geldart 1995). The reflection coefficient R and the transmission (refraction) coefficient T are introduced to denote relationships between the amplitudes of the incident and reflected or refracted waves (Sheriff and Geldart 1995):

$$R = \frac{Z_2 - Z_1}{Z_2 + Z_1} \tag{3.12}$$

$$T = \frac{2Z_1}{Z_2 + Z_1} \tag{3.13}$$

where Z_1 and Z_2 are the acoustic impedance of mediums 1 and 2, respectively. The sign of the reflection coefficient, R can be either positive or negative, representing the phase change relative to the incident wave. The acoustic impedance is the product of mass density and wave speed;

$$Z = \rho C \tag{3.14}$$

Once the reflection coefficient and transmission coefficients are calculated, the amplitudes of reflected and refracted P- and S-waves can be determined as follows:

$$A_{rfl} = A_i R \tag{3.15}$$

$$A_{rfr} = A_i T \tag{3.16}$$

where A_i is the amplitude of the incident wave and A_{rfl} and A_{rfr} are the amplitudes of reflected and refracted waves, respectively. Additionally, the reflection energy coefficient, E_R, and transmission energy coefficient, E_T, are used to relate the energy of incident and reflected/refracted waves. The relationships may be expressed as (Sheriff and Geldart 1995)

$$E_R = R^2 \tag{3.17}$$

$$E_T = \frac{Z_2}{Z_1} T^2 \tag{3.18}$$

where the sum of E_R and E_T is 1.

Values of acoustic impedance for some common materials, as given in Table 3.1, determine whether the incident P-wave is reflected at different material interfaces (Sansalone and Carino 1990; Cheng and Sansalone 1993b, Sansalone and Streett 1997, Carino 2001). The concrete/air interface is the situation most commonly encountered in impact-echo testing, where $Z_2 << Z_1$, i.e., the acoustic impedance of concrete is almost 10^7 times that of air. For this case, there is practically only reflection occurring at the concrete/air interface as nearly 100% of the energy from the incident wave is converted to reflected wave energy. This is the reason why the impact-echo method can be successfully applied to detect the thickness of concrete structures, as well as the presence of internal delaminations or voids. Moreover, the R-value is negative, which means an incident compressive P-wave will be reflected as a tensile P-wave and vice-versa.

For the case of a concrete/steel interface, $Z_2 > Z_1$ and both reflection and refraction occur at the interface whereas the sign of reflection coefficient R does not change, which means an incident compressive P-wave will result in a reflected compressive P-wave. This case can also occur at the concrete/rock interface in tunnels, as the acoustic impedance of rock is higher than concrete.

Table 3.1 Values of acoustic impedance for commonly used materials (from Sansalone and Carino 1991).

Material	**Acoustic Impedance kg/(m^{2}s)**
Air	0.4
Water	0.5×10^6
Soil	0.3×10^6 to 4×10^6
Concrete	7×10^6 to 10×10^6
Steel	47×10^6

Diffraction is another phenomenon that occurs in impact-echo testing when the incident P-wave encounters the edge of openings or cracks within concrete structures. This gives rise to a longer traveling distance of stress waves propagating in the concrete, which generally causes a lower peak frequency and lower peak amplitude in the frequency domain (Sansalone and Carino 1986, Cheng and Sansalone 1993a, Sansalone and Streett 1997).

In an impact-echo test, the transducer adjacent to the impact point senses the displacements caused by multiple reflections of the P-wave at the testing surface. At this point, Eq. (3.1) can be applied:

$$C_p = \frac{1}{t} \times 2d \tag{3.19}$$

where C_p is the P-wave speed of the concrete, t is the period of the characteristic displacement, which is also equal to the reciprocal of the dominant frequency (f) of the sensor signal's Fourier transform, d is the solid thickness, and $2d$ is the wavelength, equal to the distance the P-wave travels in one period. Equation (3.19) can be rewritten as

$$d = \frac{C_p}{2f} \tag{3.20}$$

This is the basic equation for determining the thickness (d) of solid concrete structures using the impact-echo method. However, previous research consisting of experiments and numerical simulations has demonstrated there should be a shape factor, β, which is a function of the geometry of the tested structure, to convert the P-wave speed from Eq. (3.2) or the P-wave speed test to the apparent P-wave speed measured in the impact-echo test (Lin et al. 1996, Lin and Sansalone 1997, Sansalone and Streett 1997). For plate-like concrete structures, the shape factor is equal to 0.96, and Eq. (3.20) can be written as

$$d = \frac{0.96C_p}{2f} \tag{3.21}$$

where f is termed the solid thickness frequency, and corresponds to the fundamental mode of vibration due to vertically propagating P-waves in the plate.

3.2 Frequency Analysis

Historically, impact-echo test data was first analyzed in the time domain (e.g., Sansalone and Carino 1986a). Analyzing the results in the frequency domain instead of the time domain was one of the major breakthroughs in the development of the impact-echo method (Sansalone and Carino 1986, Carino et al. 1986b, Sansalone 1997). Since the waveforms in the time domain are rather complex due to the multiple reflections in concrete structures, the Fourier transform is used for converting the signals into the frequency domain. Multiple reflections between the upper concrete surface and either internal flaws or the lower concrete surface then give rise to dominant frequency peaks. As a result, it is much easier to interpret the testing results in the frequency domain.

In the Fourier series, any periodic signal can be expressed as an infinite sum of simple harmonic sine and cosine functions (e.g., Kuo et al. 2013). The amplitude and phase of each harmonic component in the Fourier series can be calculated using well-known formulas, but it is more common in signal processing to use Fourier transforms rather than Fourier series. The Continuous Time Fourier Transform (CTFT) of a continuous signal, $x(t)$, over an infinite range is defined as

$$X(f) = \int_{-\infty}^{\infty} x(t) e^{-i2\pi ft} dt, \qquad -\infty < f < \infty, \tag{3.22}$$

where $i = \sqrt{-1}$ is the imaginary unit, f is frequency in Hertz, and t is time in seconds. The inverse of the CTFT is

$$x(t) = \int_{-\infty}^{\infty} X(f) e^{i2\pi ft} df, \qquad -\infty < t < \infty. \tag{3.23}$$

In practice, it is impossible to measure a signal over an infinite time range, so the CTFT can be estimated over a finite time range as

$$X(f) = \int_{0}^{T} x(t) e^{-i2\pi ft} dt, \qquad 0 < t < T, \tag{3.24}$$

where T is the duration of the measurement. Additionally, computers can only store and process discrete rather than continuous signals. If the data is sampled at the discrete times $t_n = n\,\Delta t$ where $n = 0,1,2,..,N$ and $\Delta t = T/N$, the finite-range CTFT can be estimated as

$$X(f,T) \approx \Delta t \sum_{n=0}^{N-1} x_n e^{-i2\pi f t_n}, \tag{3.25}$$

which is simply a numerical integration of Eq. (3.24) in which the frequencies f can be freely chosen and need not be related to T. However, the convention is to choose to calculate Eq. (3.25) at the discrete frequencies

$$f_k = \frac{k}{T} = \frac{f_s \,\mathrm{k}}{N}, \;\; k = 0,1,2,...,\mathrm{N}-1. \tag{3.26}$$

where $f_s = N/T = 1/\Delta t$ is the sampling rate. Using the chosen frequencies f_k in Eq. (3.25) gives the Discrete Fourier Transform (DFT)

$$X_T\left(f_k\right) = \Delta t \sum_{n=0}^{N-1} x_n e^{-i2\pi\frac{kn}{N}}, \tag{3.27}$$

Which is typically implemented using the recursive Fast Fourier Transform (FFT) algorithm, in which the processed number of recorded data points, N, should be a power of 2 for optimum efficiency.

$$X_k \equiv \frac{X_T(f_k)}{\Delta t} = \sum_{n=0}^{N-1} x_n e^{-i2\pi\frac{kn}{N}}, \quad k = 0,1,2,...,\mathrm{N}-1, \tag{3.28}$$

where X_k are the FFT components. It can be seen that the FFT in Eq. (3.28) and DFT in Eq. (3.27) are periodic modulo N, i.e. $X_{k+N} = X_k$, so the last half of the FFT vector can be viewed as corresponding to negative frequencies because $X_{N-k} = X_{-k}$. Additionally, for real-valued x_n, only half of the FFT vector is unique due to the symmetry $X_k = X_{-k}^* = X_{N-k}^*$, where * denotes the complex conjugate. Due to this symmetry, the 1-sided FFT spectrum, defined as

$$X_k^{o.s.} = \begin{cases} X_k, & k = 0 \\ 2X_k, & k = 1,2,...,N/2 \end{cases} \tag{3.29}$$

is commonly used in practice, corresponding to the frequency range $0 \le f_k \le f_s/2$. It can be shown that the FFT is equivalent to representing the sampled time-history by an *N*-term Fourier series.

Since the frequency resolution (frequency interval Δf) in the FFT is fixed for a given record length N and sampling rate, f_s, the resolution with which the frequency spectrum can be displayed is limited. For impact-echo tests, this means that the dominant resonant frequency can only be estimated to the nearest integer multiple of Δf .To obtain a smoother frequency spectrum and try to more accurately identify the peak frequencies, direct numerical integration of the DTFT in Eq. (3.25) was used instead of the FFT in this study. A comparison of the results between the FFT and direct numerical integration of the DTFT are presented in the following sections. Effects of the time record length, T , as well as crosstalk issues for the DAQ experienced during testing are also discussed later in this chapter.

Before comparing results of impact-echo testing processed by FFT with numerical integration, a simple numerical example is given here to verify the correctness of the numerical integration method. The time-domain waveform for a simple periodic signal is given and the frequency domain spectra obtained by the FFT and direct integration methods are plotted for comparison. The periodic signal is composed of two sinusoids with amplitudes of 0.5 and 1 at frequencies of 5 and 10 kHz, respectively;

$$x(t) = 0.5\sin(2\pi f_1 t) + \sin(2\pi f_2 t) \tag{3.30}$$

where $f_1 = 5$ kHz and $f_2 = 10$ kHz are the frequencies for each component, and t is time in seconds.

The time domain waveform was sampled using a sampling rate of $f_s = 500$ kHz (sampling interval $\Delta t = 2$ μs) and $N = 1024$ samples, which gives a total sampling period length of $T = 2048$ μs (Figure 3.4a). According to the Nyquist criterion, the sampling rate should be at least twice the highest frequency of interest, which means the maximum frequency displayed in the frequency spectrum should be half of the sampling rate, or 250 kHz in this case. Figure 3.4b shows only the initial 50 kHz portion of the frequency spectrum for this waveform, obtained by both the FFT and numerical integration methods in MATLAB.

By using the FFT method, the frequency resolution $\Delta f = 1/T = f_s / N$ is equal to 488 Hz in this case. However, by using the numerical integration of the DFT based upon Eq. (3.25), the frequency interval can be assigned any desired number, and 50 Hz was selected for this example. From Figure 3.4b, it can be seen that the numerical integration method improves the accuracy of the peak frequencies at the expense of amplitude errors in the form of spectral leakage evidenced by the appearance of sidelobes. However, for this case (in which the selected frequency interval of 50 Hz is a perfect integer divisor of f_1 and f_2), the peak frequencies obtained by the numerical integration method are exactly equal to the correct values of f_1 and f_2. Because identification of the correct peak frequencies is more important than the relative amplitude of the frequency spectra in impact echo testing, direct numerical integration of the DTFT will be used instead of the FFT for analyzing the impact-echo tests in this study.

To compare the FFT and numerical integration of DTFT methods for an actual IE test, the time domain waveform and corresponding frequency spectrum for a physically-coupled impact-echo test are shown in Figure 3.5a and 3.5b, respectively. This test was performed on a solid concrete plate with a 152.4mm (6in.) nominal thickness, using a sampling rate of 500 kHz and 2048 samples. An accelerometer was used to record the time domain signal due to impact-generated stress waves, which was then converted into the frequency domain by the FFT and numerical integration methods. The P-wave speed measured for this plate ranges from 4348 to 4545m/s. Based on Eq. (3.21), the dominant frequency corresponding to the measured solid thickness of the concrete plate therefore ranges from 13.69 to 14.32 kHz.

As mentioned previously, the maximum frequency in the spectrum should be half of the sampling rate, or 250 kHz for this case. However, the maximum frequency shown in Fig. 3.5b is limited to 20 kHz because this is the frequency range of the accelerometer at ±3 dB sensitivity variation. The frequency resolutions are 244 Hz for the FFT method and 50 Hz for the numerical integration method. The dominant frequency peaks shown in Fig. 3.5b are 14.16 kHz for the FFT method and 14.2 kHz for the numerical integration method and provide a thickness of 154.1mm (6.06in.) and 153.6mm (6.05in), respectively, based on Eq. (3.21). Results obtained from the numerical integration method are in good agreement with the FFT method. However, the frequency interval (resolution) Δf can be adjusted using the numerical integration method without varying the sampling rate and number of samples.

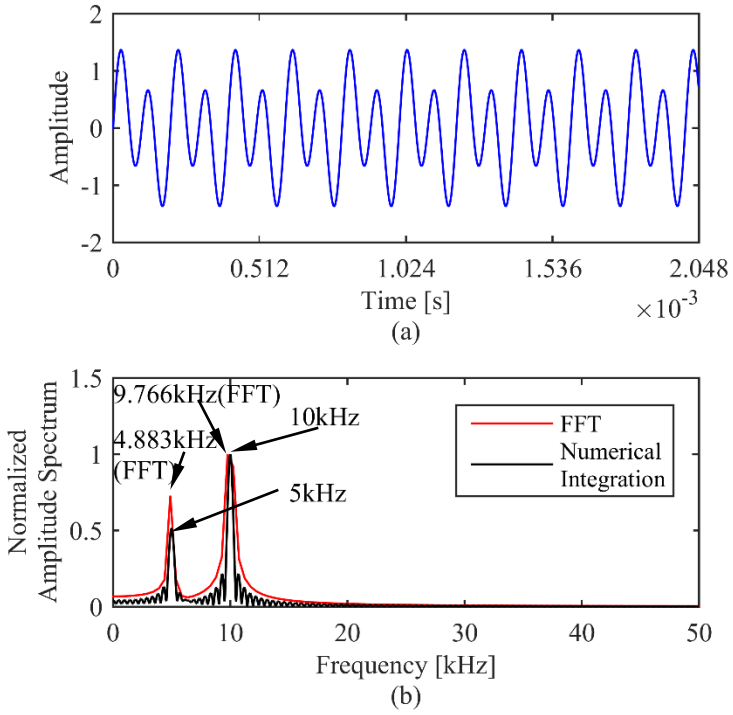

Figure 3.4. Numerical example of frequency spectra calculated by FFT vs. numerical integration of DTFT: (a) time domain waveform; (b) frequency spectra.

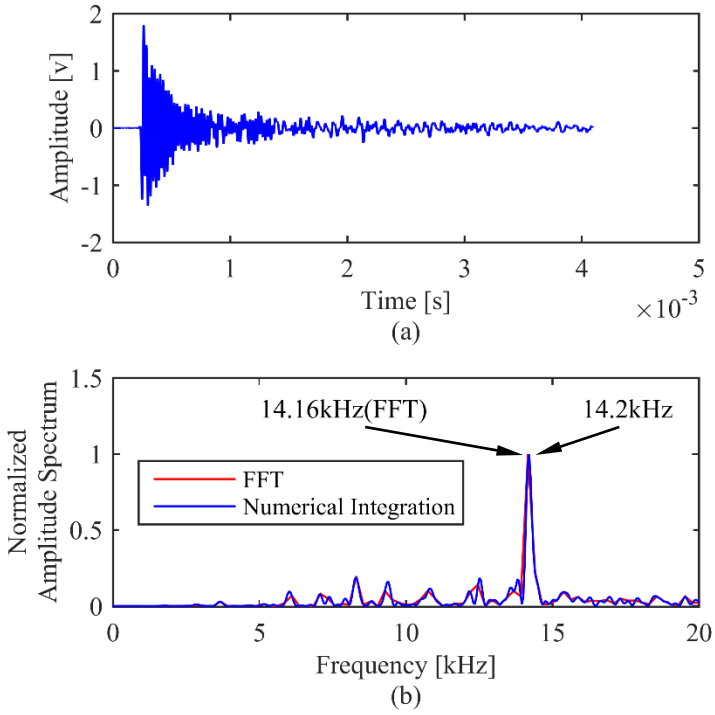

Figure 3.5. Test results from impact-echo test on solid 152.4-mm (6 in.) thick plate: (a) time domain waveform and (b) frequency spectra.

3.3 Data Acquisition and Signal Processing Considerations

As discussed in Chapter 2, the Omega OMB-DAQ-3000 was used as one part of the data acquisition system to sample the analog output signals from impact-echo sensors for later analysis. In addition to the channel configuration and voltage range, there are two important parameters to be selected for signal processing; the sampling rate f_s and sampling period T. According to the Nyquist criteria, the sampling rate should be at least twice the maximum frequency of interest. However, as a rule of thumb, the data acquisition system should actually provide a sampling rate at least ten times the maximum frequency of interest for best accuracy (e.g., Sansalone and Carino 1986, Sansalone and Streett 1997). Since previous studies showed that the maximum frequency of interest seldom exceeds 50

kHz in impact-echo testing, a sampling rate of 500 kHz was chosen in this study. The sampling period also has a substantial effect on the test results, because the impact-echo test is based on transient resonance excited by stress waves. The effect of sampling period on IE test results will be discussed next. Additionally, crosstalk caused by the DAQ encountered during testing and its solution will be presented as well.

3.3.1 Effect of Sampling Period

The sampling period T is the ratio of the number of samples N to the sampling rate f_s. For the transient motion recorded in IE tests, different sampling periods will give rise to various results in the frequency spectrum. For instance, as sampling period increases, undesirable reflections between the impact surface and lateral boundaries may be involved in the time domain waveform. As a result, several peaks will appear in the frequency spectrum and the dominant peak will no longer be clear (Sansalone and Streett 1997). Therefore, choosing an appropriate sampling period is significant for capturing a dominant solid thickness frequency. To examine this issue, IE test results using four different sampling periods on the same specimen are shown in Figure 3.6, including time domain waveforms and the corresponding frequency spectra. Tests were performed at the same point of a solid concrete plate with a 152.4mm (6in.) nominal thickness. Surface accelerations due to impact-generated stress waves were captured by a physically-coupled accelerometer, and the time domain waveform was converted to the frequency spectrum by the DTFT numerical integration method discussed previously. The measured P-wave

speed ranged from 4348 to 4545m/s for this plate, and the corresponding theoretical range of dominant thickness frequency is 13.69 to 14.32 kHz calculated via Eq. (3.21).

Four separate tests were performed with a sampling rate of 500 kHz and sampling periods of 2048 μs, 4096 μs, 8192 μs, and 16384 μs. The time-domain waveforms and frequency spectra are shown in Fig. 3.6. The first three sampling periods provide a distinct solid thickness frequency at 14.3 kHz, 14.2 kHz, and 14.1 kHz, respectively (Figs. 3.6 b, 3.6d, and 3.6f). However, the longest sampling period of 16384 μs (Fig. 3.6g) no longer produces a single dominant thickness frequency, because multiple reflections between the impact surface and the external boundaries contribute to the measured waveform and create several peaks in the frequency domain. Therefore, there is a tradeoff between increased resolution and undesirable noise when increasing the sampling period.

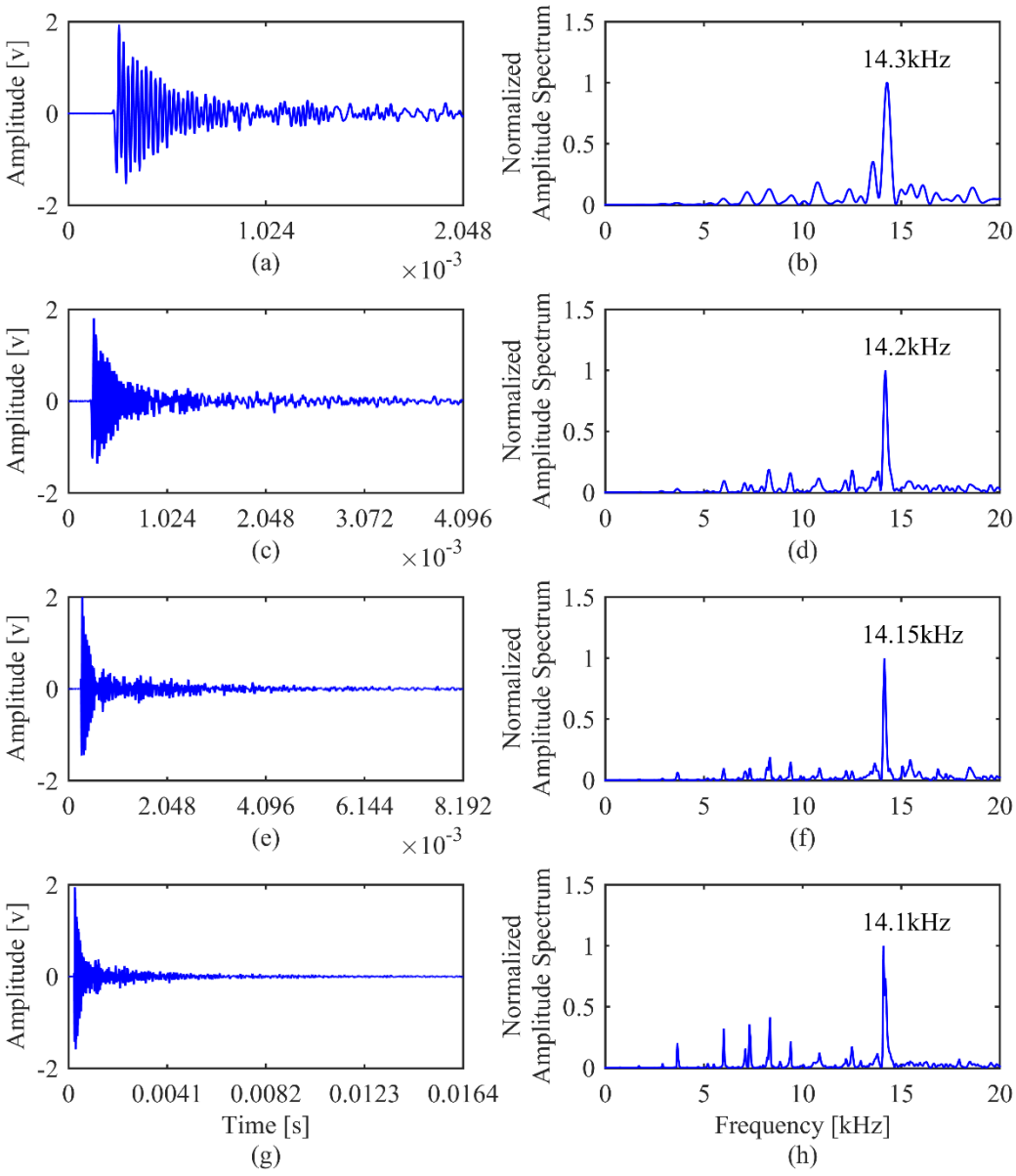

Figure 3.6. Impact-echo time-domain waveforms and frequency spectra using four different record lengths: (a) and (b) 2048 μs; (c) and (d) 4096 μs; (e) and (f) 8192 μs; (g) and (h) 16,384 μs.

3.3.2 Crosstalk

As mentioned in Chapter 2, crosstalk occurs when performing the two-channel P-wave speed measurement tests using the Omega OMB-DAQ-3000. The crosstalk is caused

by signal leakage from the first channel recording large voltages when the wave passes the first accelerometer, to the second channel which should still be recording zero volts. Due to crosstalk, the second channel records an erroneous signal proportional to that of the first channel even though the P-wave has not arrived yet. To measure the P-wave speed, the first arrivals must be clearly distinguishable and the crosstalk must therefore be minimized or eliminated.

To clearly identify the first P-wave arrival for both accelerometers, the crosstalk can be suppressed by several techniques suggested in the *Personal Daq/3000 User's Guide*, which include separating the two measurement channels by one channel, using differential connections and connecting the low-side of each channel to ground, connecting the grounds of all measured channels together, and also shorting the high and low sides and scanning the channel placed between the two measurement channels. However, by scanning a third channel between the two measurement channels, the maximum sampling rate will be decreased from 500 kHz for two channels to 333.3 kHz for three channels.

Figure 3.7 shows the time-domain waveforms of testing results from P-wave speed measurement tests before and after implementing the measures to reduce the crosstalk. Waveforms on the right-side (parts (b), (d) and (f)) of this figure show expanded views of the initial portion of the corresponding full waveforms shown on the left-side (parts (a), (c), and (e)). The waveforms in part (a) of Figure 3.7 are obtained by scanning two adjacent channels at a sampling rate of 500 kHz per channel, which clearly results in crosstalk as seen in part (b). Waveforms in part (c) are obtained by scanning two channels at a sampling rate of 333.3 kHz per channel, and by implementing all suggested crosstalk reducing

methods, except for scanning a shorted channel in between. It is clear from part (d) that crosstalk still exists in this circumstance. Finally, by including the shorted channel between the two measurement channels in the scanning group (parts (e) and (f)), the crosstalk is practically eliminated. This comes at a cost of reducing the sampling frequency from 500 kHz as recommended in ASTM C1383 (1998) to 333.3 kHz, but allows the P-wave arrival times to be clearly identified for calculation of the P-wave speed.

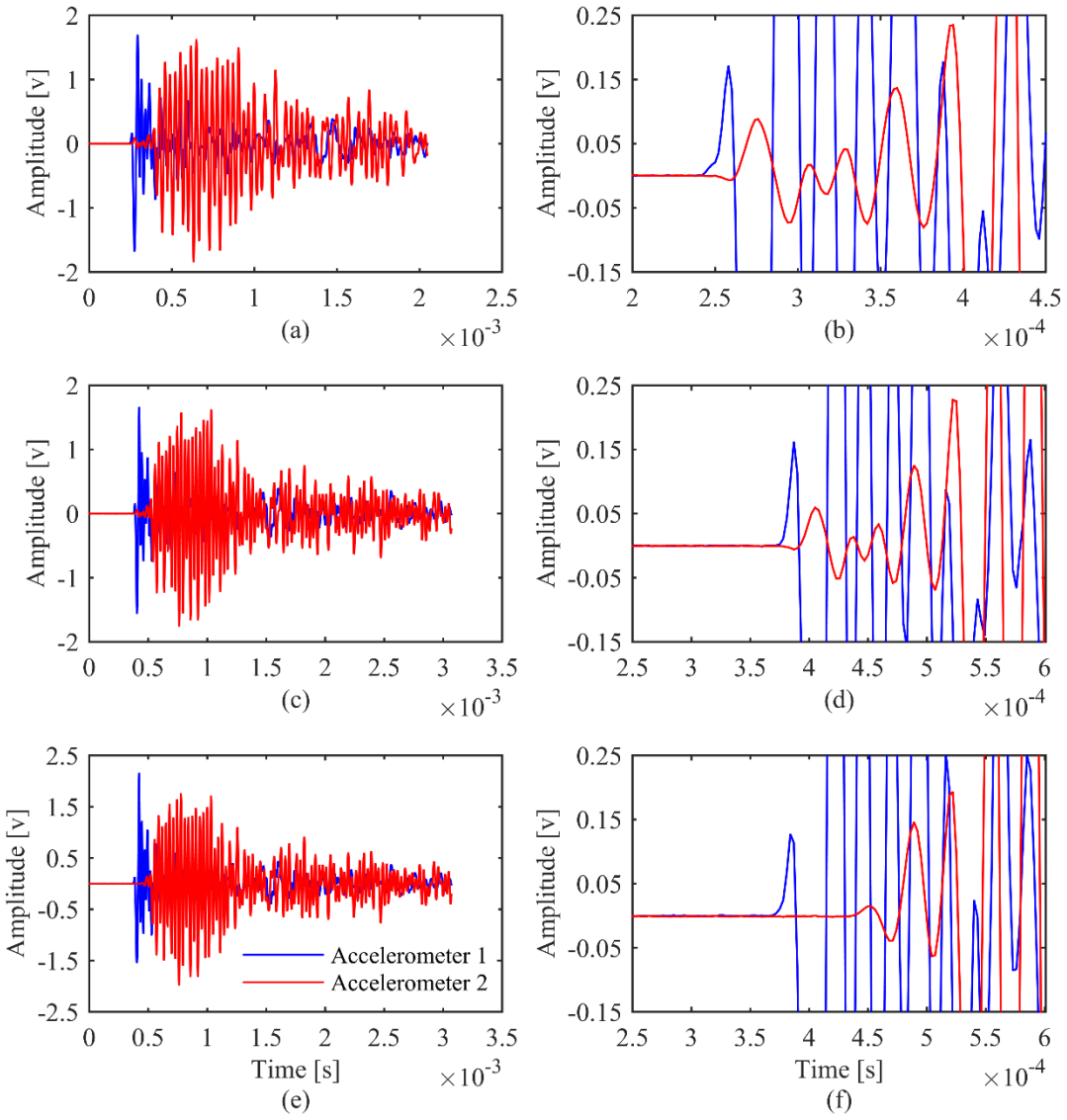

Figure 3.7. Results from P-wave speed measurement tests: (a) and (b) waveforms with crosstalk by scanning two channels at 500 kHz per channel; (c) and (d) waveforms with crosstalk by scanning two channels at 333.3 kHz per channel; (e) and (f) crosstalk eliminated by scanning three channels at 333.3 kHz per channel, with shorted middle channel.

CHAPTER 4. NUMERICCAL SIMULAATION OF THE IMPACT-ECHO TEST

4.1 Introduction

In practice, engineers have commonly used the finite element method (FEM) to solve complex problems that are not possible to solve analytically. As the first breakthrough in impact-echo research, the FEM has been widely used as an effective numerical simulation method to investigate the behavior of impact-generated stress waves in concrete structures (Sansalone et al. 1987a, 1987b, Sansalone and Carino 1987, Cheng and Sansalone 1993a, Sansalone 1997). Moreover, FEM simulations have recently been employed to study the acoustic-structure interaction and effect of parabolic reflectors in air-coupled impact-echo tests (e.g., Dai et al. 2011, Kee et al. 2012). As mentioned in Chapter 2, a microphone is used as the sensor for the air-coupled impact-echo test method, and parabolic reflectors have been used to improve the signal quality. To gain a better understanding of how the geometric parameters of a parabolic reflector affect test results, and determine an optimum testing configuration, FEM simulations of acoustic-structure interaction in ACIE testing were conducted using COMSOL Multiphysics software (COMSOL 4.4 2014) in this study. This chapter will present the process of building the FEM model and results of the simulations.

4.2 FEM Simulation of Air-Coupled Impact-Echo Tests

COMSOL Multiphysics is a commercial Finite Element program that enables coupled analysis of a wide range of electrical, chemical, fluid, and mechanical physical phenomena. The program also allows one to easily add their own governing linear or

nonlinear partial and ordinary differential equations and define aspects such as geometry and loading conditions using parametric equations, then perform automated parametric sweeps. In any FEM-based software, one must assign material properties and specify constitutive relations and boundary conditions prior to solving problems. Hundreds of pre-defined materials can be specified and boundary conditions delineated, and the governing partial differential equations are generated automatically once the physics are determined.

As with any other FEM-based software, the first step is to build the geometry of the structure for analysis. Figure 4.1 shows the geometry of the modeled air-coupled impact-echo system in a two-dimensional (2D) plane, which includes a solid field, an air field, and a parabolic reflector. The lateral dimension of the concrete plate is the same as the air region, which is 0.3 m. The thickness of the concrete plate and air region are 0.1 m and 0.35 m, respectively. To investigate the effects of the geometry of the parabolic reflector on the ACIE measurements, four parabolic reflectors with different geometries were analyzed in this study. As specified in ASTM C 1383, the impact-echo test is only valid for a concrete plate for which the ratio of lateral dimension to the thickness is at least 6. However, to reduce computational complexity and time, impedance matched low-reflecting boundary conditions (also referred to as silent boundaries) were assigned to left and right sides of the concrete plate, which simulates a plate of infinite lateral extent by eliminating stress wave reflections. To reduce the time needed to generate the models with different geometries, equations were defined in the program for several parameters related to the structure's geometry and the impact load functions.

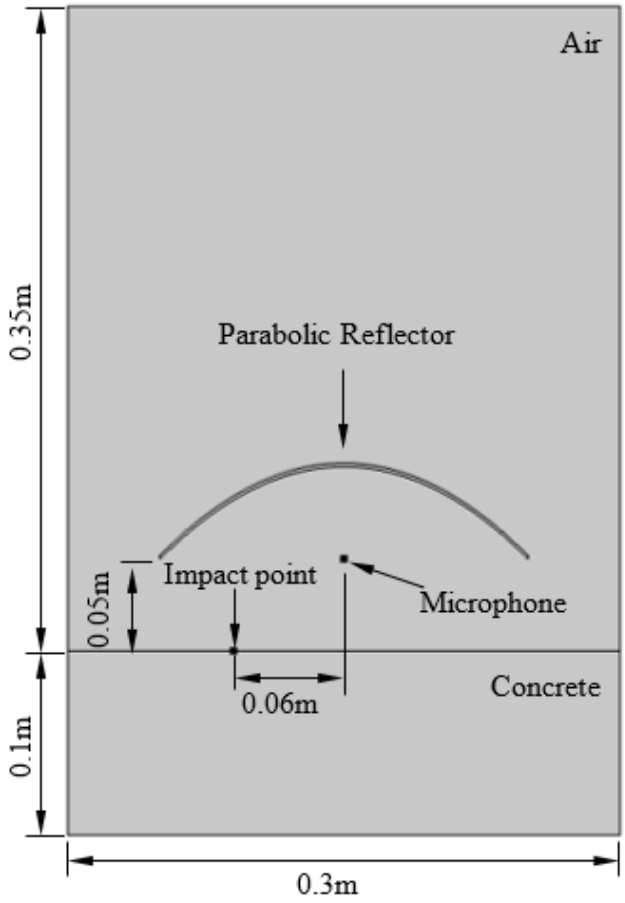

Figure 4.1. Geometry of modeled system in 2D plane simulated in COMSOL.

After defining the geometry of the model, materials are specified and assigned to each domain. The concrete and reflector materials used in the simulation are assumed homogeneous and linear-elastic. As discussed in Chapter 3, the speed of the stress waves in a homogeneous, elastic solid is a function of Young's modulus, mass density, and Poisson's ratio. The material parameters used for the concrete are listed in Table 4.1. Using these values in Eqs. (3.2), (3.5), and (3.7), the P-, S-, and R-wave speeds were calculated as 4100, 2511, and 2289 m/s, respectively. The theoretical thickness frequency given by Eq. (3.21) is then determined to be 19.68 kHz.

Table 4.1. Material parameters used for concrete.

Property	Symbol	Value	Unit
Density	ρ	2.5×10^{3}	kg/m^3
Young's modulus	E	37.823×10^{9}	Pa
Poisson's ratio	v	0.20	None

An Acoustic-Solid Interaction, Transient (astd) physics interface was utilized for simulation of the impact-echo test in COMSOL. The Acoustic-Solid Interaction interface couples the pressure acoustics in the fluid domain with the solid mechanics in the solid domain. Once the fluid and solid domains are specified, the interface will automatically identify the fluid-solid interfaces and apply the coupling compatibility conditions to them. For simulating effective impact-generated stress waves, previous studies showed the impact force vs. time function can be represented by a half-cycle sine curve (Carino et al. 1986b). Therefore, a downward point load was applied 6 mm from the center of the model on the concrete surface for simulation in COMSOL. The point load was defined by the simple piecewise sine curve:

$$\begin{aligned} &for\ 0 < t < t_c: \\ &\qquad F(t) = -F_{amp}\left[\sin(\pi t / t_c)\right]^2, \\ &for\ t > t_c: \\ &\qquad F(t) = 0. \end{aligned} \tag{4.1}$$

where t is the time in seconds; F_{amp} is the amplitude of the impact force in Newtons, t_c is the contact duration of impact in seconds. The negative sign means that the direction of impact force is downward. Figure 4.2 shows the force-time function used to model impacts

in the FEM simulation. A maximum impact force of 250 N was used, with a contact duration of 30 μs . This impact is similar to that produced by a steel sphere 7 mm in diameter, which is a common size used in impact-echo testing.

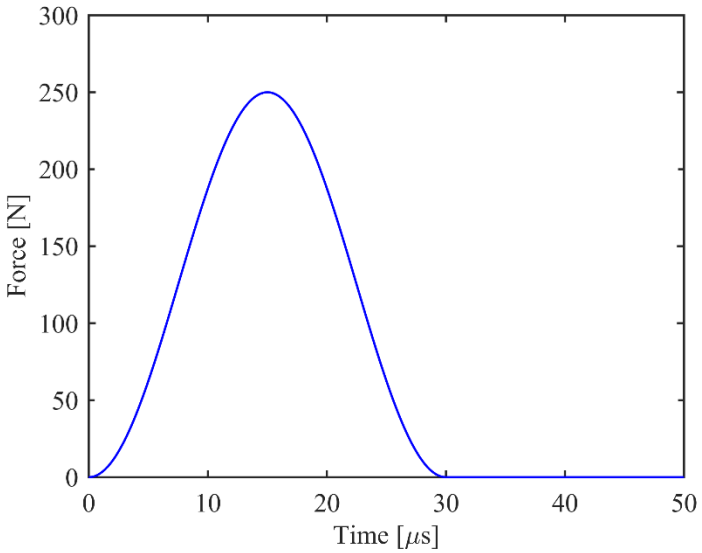

Figure 4.2. Time-force function of impact used in COMSOL FEM simulation.

As mentioned previously, to diminish reflections of stress waves from the left and right boundaries, low-reflecting boundaries should be specified on both left and right sides of the concrete plate. Meshing the model geometry is the last step to complete prior to computing. For transient analysis, a sufficiently fine mesh should be used to resolve the waveforms of the smallest wavelength of interest, which usually requires manually tuning the mesh. A maximum element size of 2 mm was used for simulation in this study. Figure 4.3a shows the finite element mesh of the entire modeled domain corresponding to the system shown in Fig. 4.1. Figure 4.3b shows a close-up view of the extremely fine mesh for the concrete, parabolic reflector, and surrounding air. To model the transient wave problem, a sufficiently small time step should be specified that can resolve highest

frequency of interest. A time step of $1\ \mu s$ (sampling rate of 1 MHz) was used for simulation in this study. The maximum frequency of interest is 40 kHz, which meets the recommendation of being at least 10 times smaller than the sampling rate for time-domain analyses.

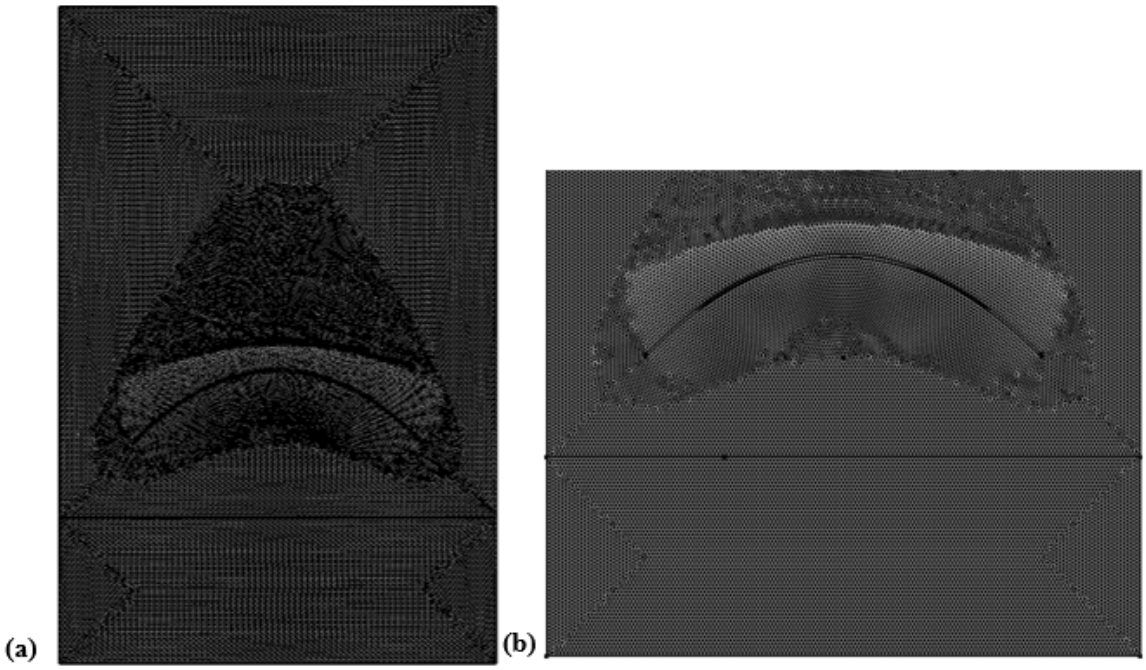

Figure 4.3. Finite element mesh of modeled system in 2D plane simulated in COMSOL: (a) entire mesh, (b): close-up of concrete, reflector, and surrounding air domains.

4.3 Numerical Simulation Results

The simulation results of impact-echo testing are presented in this section. First, for the purpose of investigating the effects of a parabolic reflector, impact-echo testing with and without a parabolic reflector were simulated using COMSOL. Then, the simulation results were exported and analyzed using MATLAB, in the form of time-domain waveforms and corresponding frequency spectra. Next, four parabolic reflectors with different geometries were modeled using COMSOL to determine the optimum geometry

of the parabolic reflector for the air-coupled impact-echo test. Finally, the effects of the reflector and microphone height from the concrete test surface were studied.

4.3.1 Effect of parabolic reflector on measurements

As discussed in Chapter 2, parabolic reflectors have been used to amplify acoustic waves dating back to at least 1930. Recent studies also showed that parabolic reflectors can be utilized in conjunction with the air-coupled impact-echo testing approach to reduce acoustic energy loss and enhance the measured signals (Zhu 2005, Dai et al. 2011, Kee et al. 2012).

To gain a better understanding of the acoustic-structure interaction between the concrete, air, and reflector, a parabolic reflector was defined by a symbolic parametric mathematical expression in COMSOL. By changing the values of the parameters, different reflector geometries could efficiently be generated, meshed, and analyzed. Figure 4.4 shows a schematic representation of the parabolic reflector with a rim angle of 90° (Fig. 4.4b) analyzed in this section, as well as three others analyzed in the next section. The width of all four parabolic reflectors is 0.2 m, and for the rim angle of 90°, the depth is 1/4 of the width (0.05 m). For all reflectors, the impact point was 0.06 m to the left of the focus of the parabola, which was taken to be the microphone position as shown in Fig. 4.2.

Simulation results with and without the parabolic reflector are compared in Fig. 4.5. The sampling rate for the simulation was 1 MHz and the sampling period was $2048\ \mu s$, which means 2048 discrete time steps were analyzed. As shown in Fig. 4.5a, the parabolic reflector magnifies the time-domain signal due to: (1) the vertically-incident acoustic energy over the reflector's entire projected area being reflected to the focus (in actual tests,

the microphone will obscure some of the reflector's area), and (2) multiple reflections between reflector and test surface (see Dai et al. 2011, Kee et al. 2012). As a result, the amplitude spectrum for the test with the parabolic reflector is much larger than without the reflector. As noted above, the theoretical solid thickness frequency for the modeled concrete slab is 19.68 kHz. For the simulation, two single sharp peaks are clearly visible in Fig. 4.5b at 19.96 kHz without the reflector and 20.25 kHz with the reflector, which are greater than the theoretical frequency by 1.4% and 2.9%, respectively.

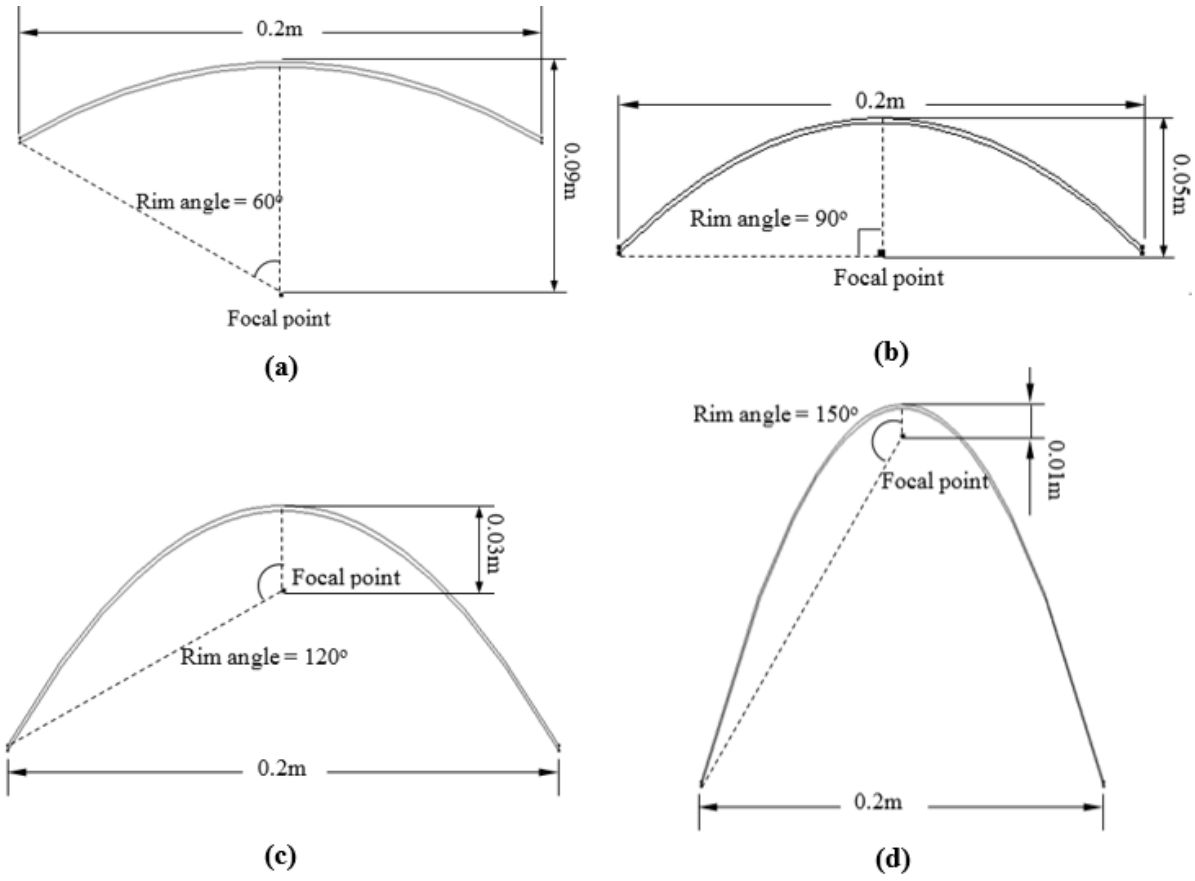

Figure 4.4. Parabolic reflector geometries studied in FEM simulation, with rim angles of 60° (a); 90° (b); 120° (c); and 150° (d).

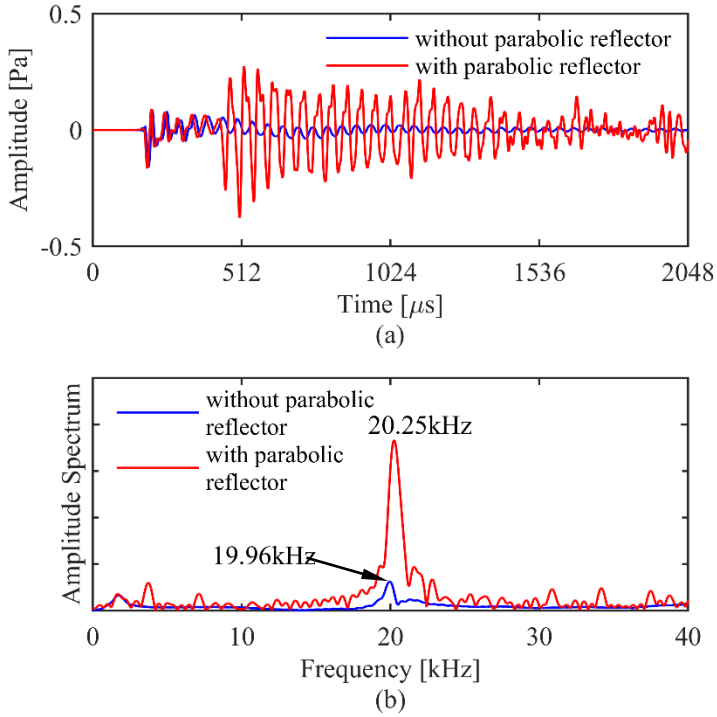

Figure 4.5. Pressure at microphone location in impact-echo test simulations with and without parabolic reflector: (a) time domain waveforms and (b) frequency spectra.

For a better understanding of the acoustic pressure in the presence of the parabolic reflector, snapshots of the total acoustic pressure field 500 μs after the impact are presented in Fig. 4.6 for tests with and without the reflector. As discussed in Chapter 3, Rayleigh waves will propagate along the concrete surface at a velocity of 2289 m/s for this case. However, some of the energy from R-waves will leak into the air and propagate with a characteristic angle, as shown in Fig. 4.6a. A direct acoustic wave will also emanate from the impact point and propagate along a spherical wavefront in the air, at a slower velocity of 343.6 m/s (at 20°C in dry air).

In Fig. 4.6a, a series of wavefronts can also be seen propagating in the air approximately parallel to the concrete surface. These are leaky Lamb waves from the first-order symmetric (S_1) Lamb mode in the plate, which have zero-group-velocity and are referred to as S_1 ZGV waves (Gibson and Popovics 2005). The S_1 ZGV waves are stationary (resonant) waves that do not propagate along the direction of the plate, and therefore dominate the response at a fixed location in the air. Because these waves are reflected to the focus by the parabolic reflector, it is clearly seen that the acoustic energy at the measurement point is much greater when the reflector is used (Fig. 4.6b). Based on these simulation results, the signal for the air-coupled impact-echo test method can be greatly enhanced under the action of the parabolic reflector, although additional minor peaks in the frequency spectrum are induced by multiple reflections (Fig. 4.5b). Despite this fact, these simulation results agree with the findings of Dai et al. (2011) that using a parabolic reflector will result in a “solid thickness frequency” (actually demonstrated by Gibson and Popovics (2005) to be the S_1 ZGV frequency) that is more easily identified in the frequency spectrum.

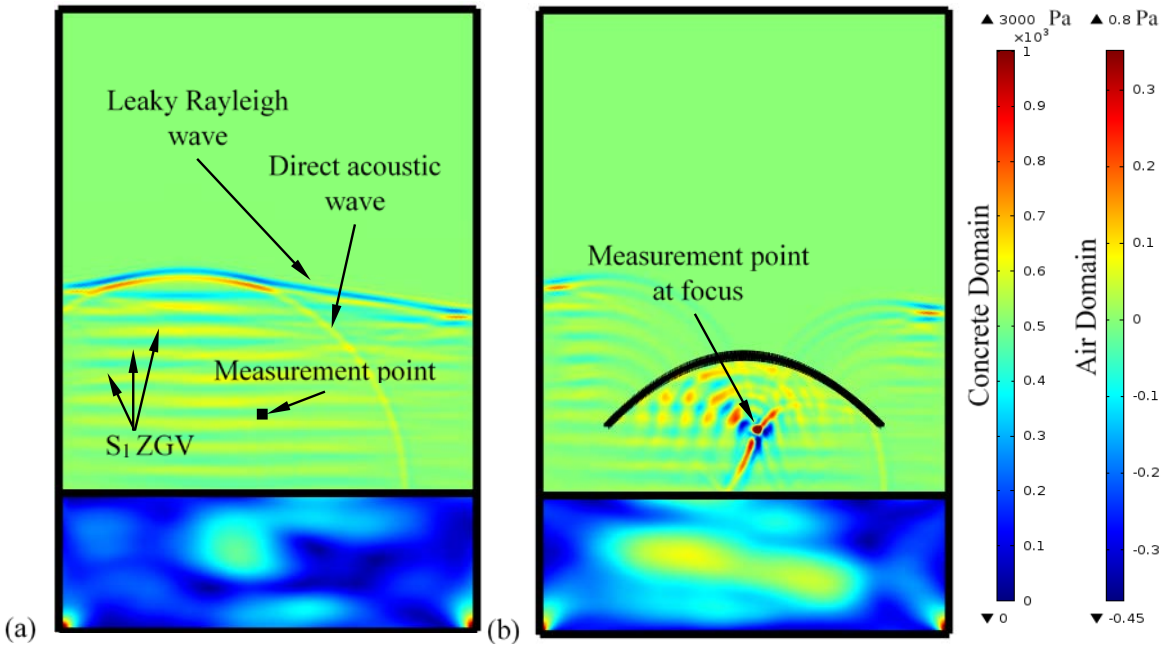

Figure 4.6. Snapshots of total acoustic pressure field from FEM simulation at $t = 500$ μs due to impact defined in Fig. 4.2: (a) without parabolic reflector; (b) with parabolic reflector.

4.3.2 Effect of parabolic reflector geometry

Since it was demonstrated in the previous section that a parabolic reflector can reduce the acoustic energy loss, determining the optimum geometry of the reflector is indispensable for air-coupled impact-echo testing. Because parabolic reflectors with various geometries are not readily available commercially, the plan for this study was to identify the optimum geometry, then manufacture a reflector using a 3D printer. The four parabolic reflectors shown in Fig. 4.4 with different geometries and rim angles of 60°, 90°, 120°, and 150° were simulated in COMSOL. All have the same width of 0.2 m, and different distances from the focal point to top. Figure 4.7 shows the geometry and relative positions of these reflectors superimposed on one another. The reflectors with rim angles of 90°, 120°, and 150° all have the same distance of 0.01 m from the rim to the concrete

test surface, while the reflector with the 60 ^{o} rim angle has the same top position as the 120^{o} reflector. Distances from the focal points of the 60 ^{o}, 90^{o}, 120^{o}, and 150^{o} reflectors to the test surface are 0.01, 0.01, 0.07, and 0.18 m, respectively.

Simulations were completed for these four reflectors using the impact load defined in Fig. 4.2, with a contact duration of 30×10^{-6}s . The impact was located at the interface between the air/concrete media and 0.06 m left of the center of the reflectors. Simulation results including time domain waveforms and corresponding frequency spectra for the four reflectors are shown in Fig. 4.8. The time step was again set to 1 μs (sampling rate of 1 MHz) with a total sampling period of 2048μs . The reflectors with rim angles of 60^{o} and 90^{o} have the same first arrival time for the leaky Rayleigh waves because they have the same height from the focal point to the test surface (Fig. 4.8a). The other two reflectors have a first arrival time that increases in proportion to their focal distance from the concrete surface. The theoretical frequency corresponding to the solid thickness mode of the concrete plate is 19.68 kHz. The simulation results shown in Fig. 4.8b indicate that although extra minor frequency peaks appear in all four frequency spectra, the solid thickness frequencies obtained in each case can be easily identified as 19.25, 20.15, 20.55, and 20.25 kHz, respectively. Comparing these spectra, it is clear that the parabolic reflector with a rim angle of 90^{o} produces the optimum spectra and the closet solid thickness frequency to the theoretical value of 19.68 kHz. These results agree with the findings of Kee et al. (2012), who reported that the maximum spectral amplification ratio was achieved with a 90^{o} rim angle.

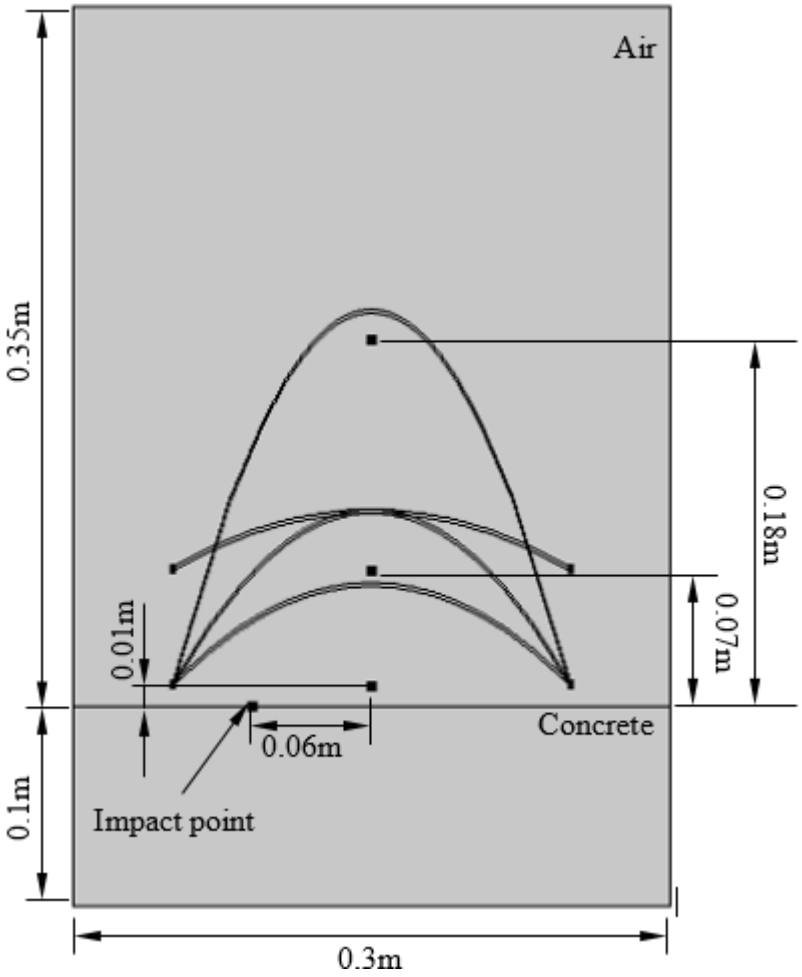

Figure 4.7. Composite view of parabolic reflector geometries and positions used in FEM simulations.

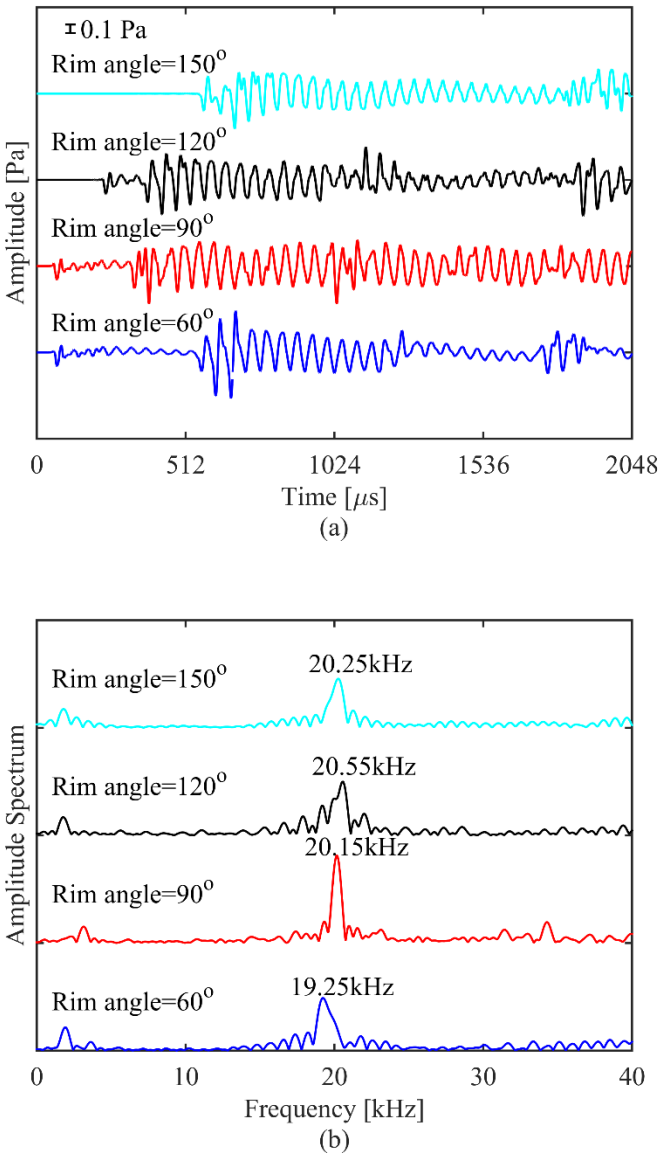

Figure 4.8. Pressure at parabolic reflector focal points from impact-echo test simulations with different rim angles: (a) time domain waveforms; (b) frequency spectra.

4.3.3 Effect of reflector focus height

Previous studies have demonstrated that an appropriate height from the air-coupled sensor to the test surface is required to avoid acoustic energy loss and sensor damage (Zhu and Popovics 2007). To determine the optimum height for a parabolic reflector with a rim

angle of 90°, FEM simulations were performed in which the height of the focal point was varied from 0.05 to 0.25 m in 0.05 m increments. A composite view of the five different reflector heights studied is shown in Fig. 4.9. The point load with a $30\ \mu s$ contact duration shown in Fig. 4.2 was applied 0.06 m to the left of the reflector axis, as shown in Fig. 4.9. For all simulations, a $1\ \mu s$ time step (1 MHz sampling rate) was used. To capture a sufficient length of signal as the height increases, the sampling period for all simulations was $8192\ \mu s$.

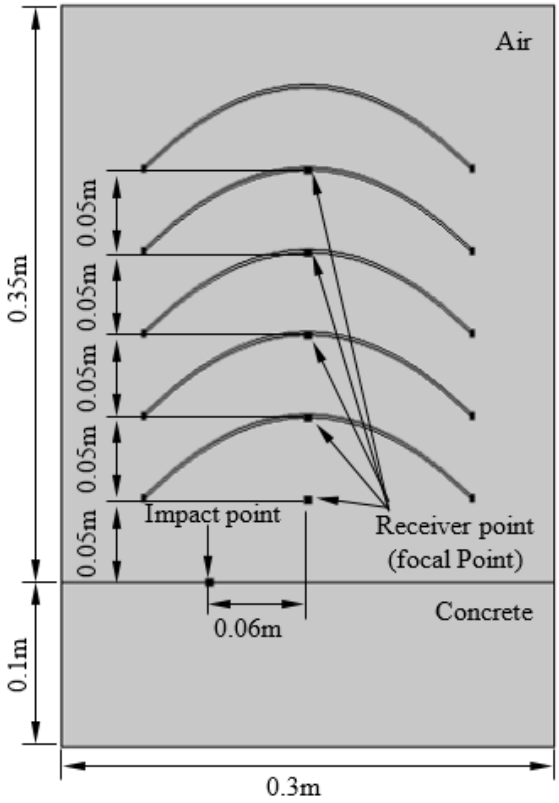

Figure 4.9. Composite view of reflectors with 90° rim angle and different focus heights studied in FEM simulations.

The time-domain waveforms and frequency spectra for the different focus heights are shown in Fig. 4.10. The frequency spectra exhibit clear solid-thickness frequencies for

each focus height, except for the 0.05 m case. Because the frequency spectrum for the 0.05 m focus height is dominated by multiple reflections between the reflector and test surface, it is difficult to discern the solid-thickness (or more precisely, S_1 ZGV) frequency (Fig. 4.10b). The remaining four focus heights give the same dominant S_1 ZGV peak frequency of 20.15 kHz, which is within 3% of the theoretical value of 19.68 kHz using the conventional β factor of 0.96 in Eq. (3.21), or more precisely, 19.56 kHz using β=0.953 for a Poisson's ratio of 0.2 as explained in Gibson and Popovics (2005). Possible reasons for the small discrepancy between the theoretical and FEM simulation frequencies are that the simulation was 2D rather than 3D, and it is subject to the discretization error, modeling error, and truncation error inherent to the finite element method. Based on the results of Fig. 4.10b, a focus height of 0.15 m is recommended, with a free-field microphone pointing upwards towards the reflector, provided that the microphone is small enough to be oriented in this direction without touching the concrete.

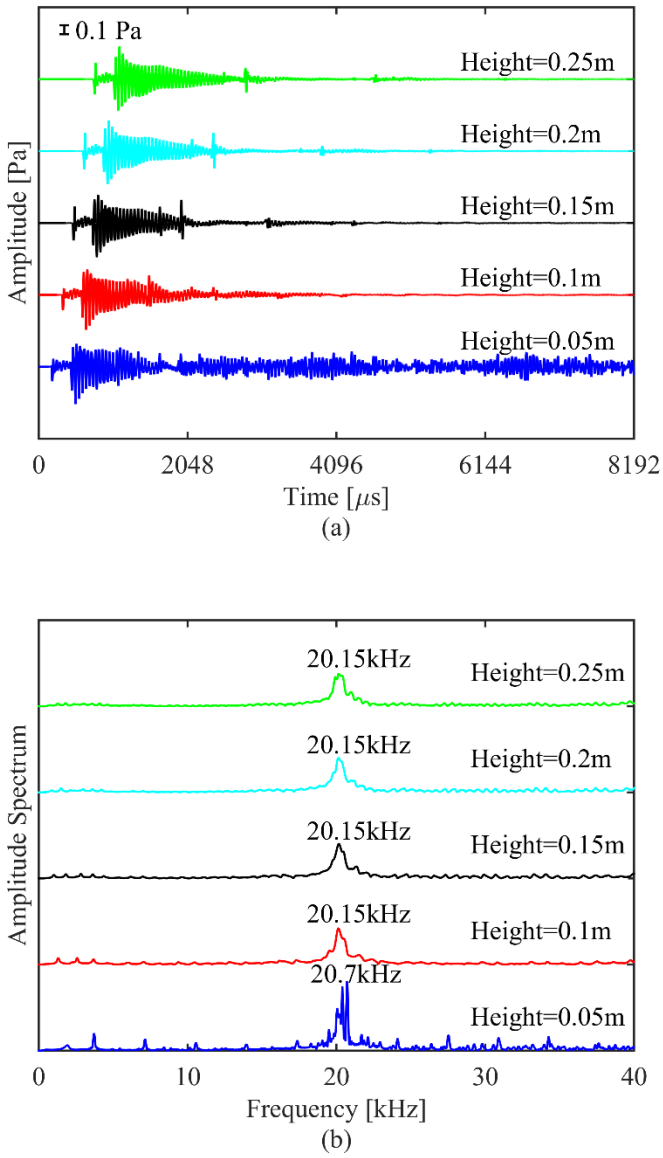

Figure 4.10. Pressure at parabolic reflector focal points from impact-echo test simulations with different focal point heights (90^{o} rim angle): (a) time domain waveforms; (b) frequency spectra.

4.4 Summary

In this chapter, a series of FEM-based numerical simulations of the air-coupled impact-echo testing method were conducted using COMSOL Multiphysics software. The beneficial effects of using a parabolic reflector to enhance the signal to noise ratio were

investigated via comparing the simulation results with and without the reflector. By comparing time domain waveforms and frequency spectra, it was verified that the parabolic reflector could significantly improve the quality of the time domain signal by amplifying it. As a result, the historically named “solid thickness frequency”, which was later demonstrated to actually be the leaky Lamb-wave S_1 ZGV frequency, can be more easily identified in the frequency domain. To determine the optimum geometry, four parabolic reflectors with different rim angles were investigated, and the optimum rim angle was found to be 90°, which agrees with results by other investigators . Finally, simulations of a 0.2 m wide, 90° reflector were conducted to determine the optimum focal point height. Results showed that the S_1 ZGV frequency peak can be clearly identified and are in good agreement with theoretical values for focus heights between 0.1 and 0.25 m.

Based on all simulation results, however, a common phenomenon was observed when using the parabolic reflector; spurious peaks appeared in the frequency spectrum due to multiple reflections between the reflector and concrete surface. The spurious peaks may lead to misidentification of the S_1 ZGV frequency. Based on the results herein, a focus height of 0.1 to 0.25 m can be recommended (0.15 m if possible), with a free-field measurement microphone aimed upward towards the reflector and placed with the measurement diaphragm at the reflector’s focus.

CHAPTER 5. EXPERIMENTAL RESULTS

5.1 Introduction

This chapter presents the experimental results for this study. First, data for the P-wave speed measurement tests on both a defect-free concrete plate and a laboratory mockup of a reinforced concrete bridge deck with artificial defects will be presented. Then, data from physically-coupled and air-coupled impact-echo tests will be combined with the P-wave speed data to quantify the deck thickness and depths of various artificial defects. Additionally, results from two-dimensional (2D) scans to locate the position of artificial defects will be discussed. Finally, application of passive filtering techniques for air-coupled impact-echo tests will be presented. Test results before and after filtering will be analyzed and compared to illustrate the effectiveness of the filtering technique in isolating the thickness frequency and minimizing ambient noise.

5.2 Measurements on Defect-Free Concrete Calibration Plate

A 36.0 in. × 36.0 in. × 6.0 in. (914.4 mm × 914.4 mm × 152.4 mm) solid concrete plate was constructed in the laboratory to verify the correct operation of the custom built impact-echo testing system and LabVIEW program, examine various reflector arrangements, and develop an optimum testing system configuration for the lab and in-situ tests. The concrete plate was cast using steel forms and a normal strength concrete mix with limestone aggregate. The nominal maximum size for the limestone was 1 in. Schematic diagrams of the solid concrete plate are shown in Fig. 5.1, and a photo of the as-built concrete plate is shown in Fig. 5.2. The plate is simply supported by two wooden blocks resting on the ground.

5.2.1 P-Wave speed measurement test

P-wave speed measurement tests were conducted on the surface of the concrete plate using the DAQ system and custom-built LabVIEW program detailed in Chapter 2. The two PCB piezoelectric accelerometers and battery-powered signal conditioner were used to measure the P-wave speed using the test setup shown in Fig. 2.2. The accelerometers were used to record the vertical surface accelerations due to the impact generated by a small steel sphere in diameter of 6.34 mm. As required by ASTM C 1383, the accelerometers were attached to the concrete plate a distance of 0.3 m apart, and the impact was performed 0.15 m from the first accelerometer. To be able to clearly identify the P-wave first arrival times for both accelerometers, the cross-talk minimizing measures presented in Chapter 3 were implemented.

Results for the P-wave speed measurement test are shown in Fig. 5.3. The time-domain waveforms for the accelerometers are shown in Fig. 5.3a, and an expanded view of the initial portion is shown in Fig. 5.3b. The maximum sampling rate of the DAQ is 1 MHz, however, three channels needed to be scanned to eliminate crosstalk, therefore each channel was scanned at 333.3 kHz. For each channel, 1024 discrete data points were recorded, resulting in a sampling period of $3072\ \mu s$. Since the travel distance, L, of the P-wave is known, the P-wave speed can be determined by:

$$C_p = \frac{L}{\Delta t} \tag{5.1}$$

where Δt is the travel time difference between the first arrival times of each waveform. The first arrival of the waveform is defined in ASTM C 1383 as the first point for which

the voltage changes from the baseline value. However, it can be difficult to determine this point precisely, and the arrival time could therefore easily be taken a few sample points to the left or right (e.g., see Fig. 5.3b). As a result, the ASTM standard specifies that P-wave speeds and thicknesses should be reported as ranges of values because of systematic errors between the measured and true values. For the data of Fig. 5.3b, the travel time difference Δt was determined to be between 66 and 69 μs. Consequently, the P-wave speed for the calibration plate is within the range 4348 to 4545 m/s, which is reasonable as concrete typically has a P-wave speed between 3000 and 5000 m/s.

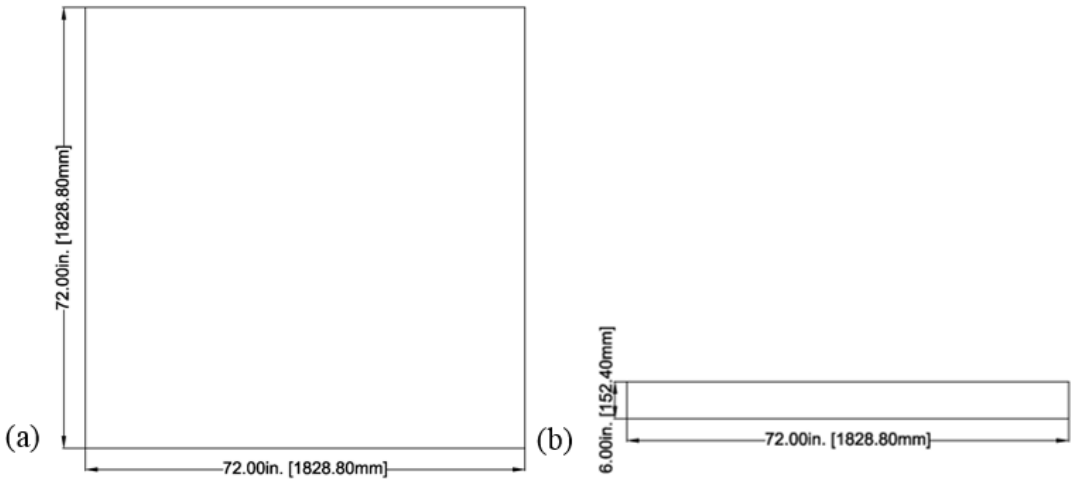

Figure 5.1. Schematic diagram of concrete plate: (a) plan view; (b) elevation view.

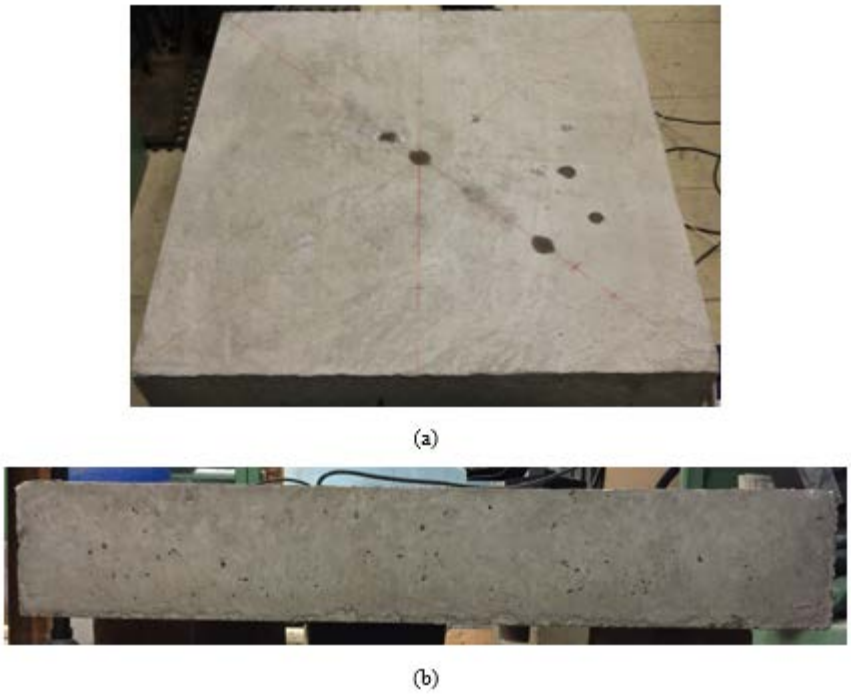

Figure 5.2. Photograph of 36×36×6 in. solid concrete plate used for calibration tests: (a) plan view; (b) side view.

5.2.2 Physically-coupled impact-echo test

Once the P-wave speed measurement test was completed, the high-frequency model 621B51 piezoelectric accelerometer was employed as a physically-coupled sensor to perform impact-echo tests on the surface of the concrete calibration plate using the test set-up shown in Fig. 2.3. Since the measured P-wave speed ranges from 4348 to 4545 m/s and the measured thickness is 6.00 in., the theoretical solid thickness frequency from Eq. (3.21) ranges from 13.69 to 14.32 kHz. As mentioned in Chapter 2, the frequency range of the model 621B51 accelerometer is 0.8–20,000 Hz for a ±3 dB variation in sensitivity. Therefore, this accelerometer is suitable for use as a physically-coupled sensor for the impact-echo tests on the calibration plate for frequencies below 20 kHz. Above this

frequency, the sensitivity will deviate beyond 3 dB and the readings should show a peak at the accelerometer's natural resonant frequency, which is approximately 35 kHz.

Test results from the physically-coupled impact-echo test are shown in Fig. 5.4. The test was performed using a sampling rate of 500 kHz since only one channel is involved and crosstalk is therefore not an issue, and 2048 discrete data points were recorded for a sampling duration of 4096 μs. Based on these test results, the solid thickness frequency is 14.2 kHz, which corresponds to a solid concrete plate with a thickness of 5.79 to 6.05in. (147 to 154 mm) for the measured P-wave speed range of 4348 to 4545 m/s. The test results are in good agreement with the theoretical frequency range (13.69–14.32 kHz) corresponding to the measured solid thickness of 6.00 in. (152 mm).

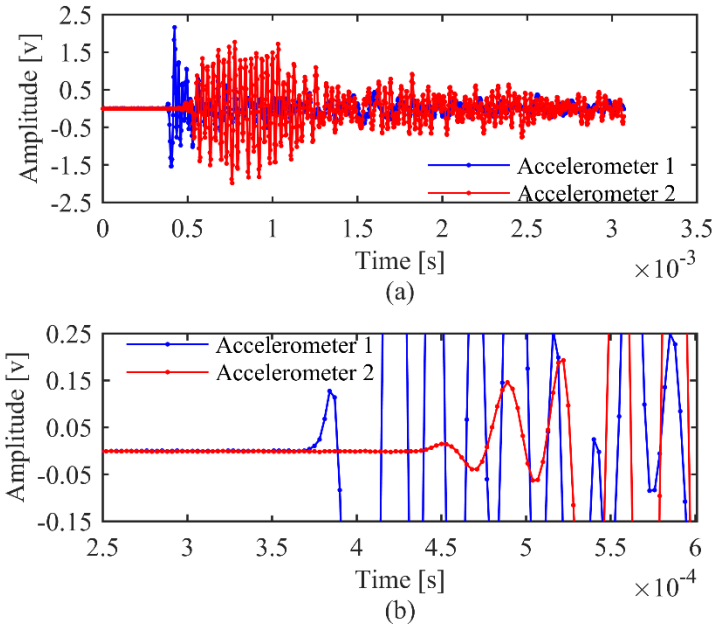

Figure 5.3. Test results for P-wave speed measurement test performed on defect-free concrete calibration plate: (a) time-domain waveforms; (b) expanded view of initial portion showing P-wave first arrivals.

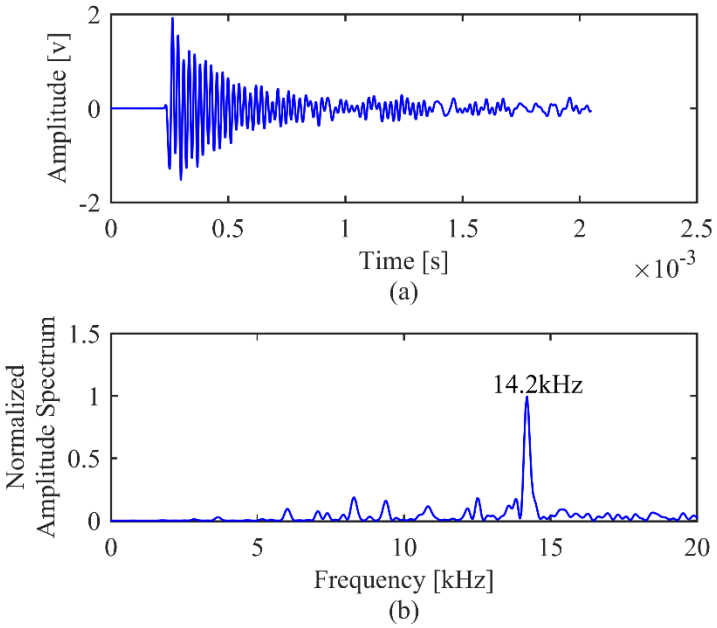

Figure 5.4. Test results for physically-coupled impact-echo test performed on defect-free concrete calibration plate: (a) time-domain waveform; (b) frequency spectrum.

5.2.3 Air-coupled impact-echo test

Compared with the air-coupled test method, the physically-coupled test method is time-consuming and labor-intensive, due to the requirement of coupling the sensor to the surface of the test structure at each measurement point. Additionally, recent studies demonstrated that accurate acoustic sensors with a broadband frequency range can be utilized for air-coupled impact-echo testing in theory and practice (e.g., Gibson and Popovics 2005, Zhu 2005).

As mentioned in Chapter 2, a PCB model 378C01 measurement microphone was used as the air-coupled sensor for impact-echo testing in this study. The microphone has a small diameter of 0.25 in. (6.4 mm) and a length of 2.07 in. (52.6 mm). It can provide highly-accurate measurements over its broadband frequency range of 4 to 80,000 Hz at ±2

dB. Although the air-coupled test method can reduce testing time and improved efficiency of 2D scans, some challenges must be overcome before the method can be implemented in practice. These challenges include ambient noise caused by traffic or wind, and acoustic energy loss due to the large mismatch in acoustic impedance between concrete and air. As previously discussed, prior studies have already proven that parabolic reflectors can greatly amplify the signal, or a sound insulation enclosure can be used to block and minimize ambient noise. Using one of these two methods can enhance the signal-to-noise ratio and reduce acoustic energy loss for the air-coupled impact-echo test (e.g., Zhu and Popovics 2007, Dai et al. 2011). Therefore, a sound isolation enclosure and a parabolic reflector (see Figs. 2.8c and 2.8d) were separately examined to minimize ambient external noise in air-coupled impact-echo tests in this study. Furthermore, filtering techniques were studied to remove traffic noise and enhance the air-coupled impact-echo frequency spectrum during signal post-processing. Results from these tests will be presented next.

The air-coupled impact-echo test set-up used is shown in Fig. 2.6. For comparison purposes, test results obtained using a microphone alone are compared in Fig. 5.5 to test results using a sound isolation enclosure, parabolic reflector, and parabolic reflector with foam annulus. For each of these four situations, the sampling rate was 500 kHz and 2048 discrete data points were collected for a sampling period of 4096 μs. Comparing the time-domain waveforms in Fig. 5.5a and the corresponding frequency spectra in Fig. 5.5b, it is clear that the signal as well as some noise is amplified at the focal point of the parabolic reflector.

To help reduce the outside noise which results in several spurious small peaks in the frequency domain, the foam annulus was added under the reflector. However, it can be seen in Fig. 5.5b that the foam reduces the magnitude of the noise, but also reduces the amplitude of the main peak. This is likely because the horizontal distance between the impact point and receiver point had to be increased when the foam was added. For all other configurations of the microphone with the reflector or enclosure, the impact-to-receiver distance was 2 in. This distance is less than 40% of the nominal thickness of the concrete plate (6 in.), as specified in ASTM C 1383 for good quality test data. Since the foam has a radius of 6 in., the impact-to-receiver distance had to be increased to 6.5 in. when the foam annulus was added, which may explain the additional peaks in the frequency spectrum in Fig. 5.5b.

As demonstrated by previous studies and proven by the numerical simulations in this study, a parabolic reflector can amplify as well as sustain the acoustic energy longer due to the multiple reflections between the reflector and test surface. As a result, the spectrum amplitude is increased when using the parabolic reflector, but extra peaks produced by the multiple reflections also appear in the frequency spectrum. The solid thickness frequencies for the test configurations shown in Fig. 5.5b are in the range 13.50–14 kHz, which agrees well with the theoretical range of thickness frequencies reported in Section 5.2.2 (i.e., 13.69–14.32 kHz) based on the measured range of P-wave speed.

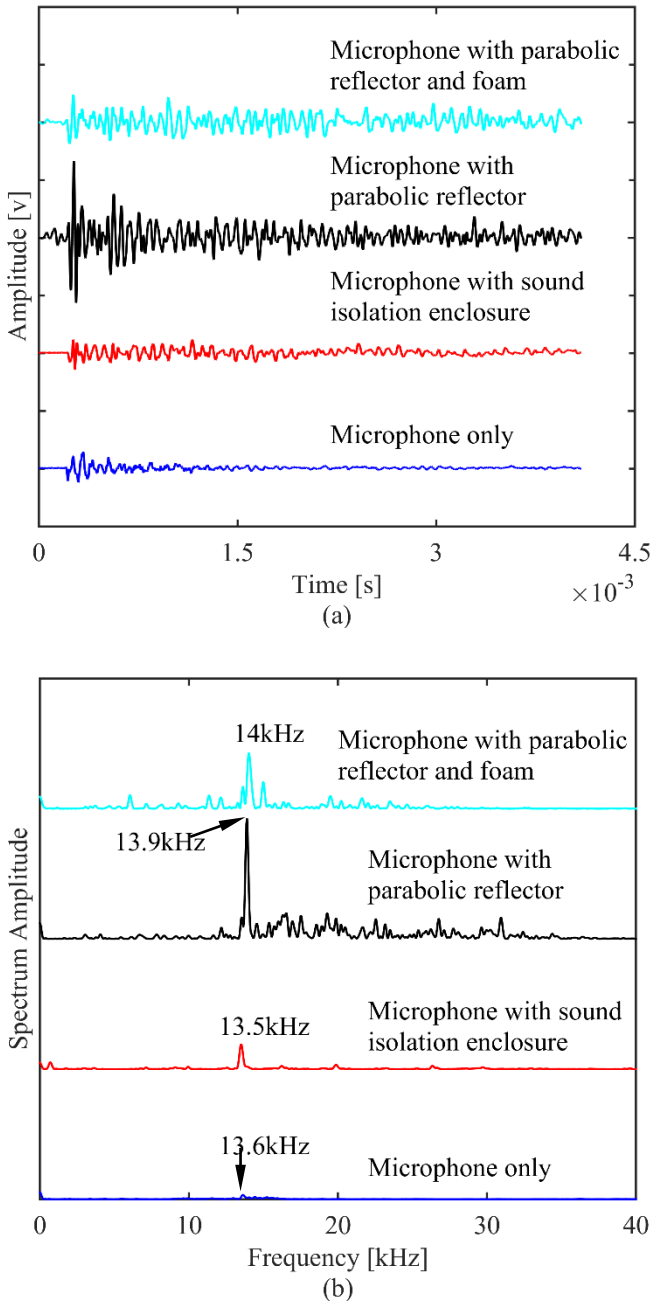

Figure 5.5. Test results for air-coupled impact-echo tests with noise-minimization measures performed on defect-free concrete calibration plate: (a) time-domain waveforms; (b) frequency spectra.

5.2.4 Comparison between physically-coupled and air-coupled impact-echo tests

As verified in the previous section, the air-coupled testing approach is suitable for use in the impact-echo test method. However, the consistency of results from the physically-coupled and air-coupled test methods should also be proven. For this purpose, a comparisons of the test results for physically-coupled and air-coupled impact-echo test methods is shown in Fig. 5.6. For all cases, the sampling frequency was 500 kHz and 2048 discrete data points were recorded for a sampling period of 4096 μs. The amplitudes of all waveforms are normalized by their maximum values to compare their relative signal-to-noise ratios. The waveforms from the accelerometer appear to be more harmonic than those from the microphone, as the physically-coupled test method is less sensitive to the effects of ambient noise than the air-coupled method. The solid-thickness frequencies obtained by both methods are in an appropriate range of 13.50–14.2 kHz, which agrees well with the theoretical range of 13.69–14.32 kHz reported in Section 5.2.2 based on the measured range of P-wave speed. Although the accelerometer works for measuring the 6 in. thickness of the test slab, depth measurements of shallow defects may fall beyond the accelerometer's maximum useful frequency of 20 kHz as will be shown below. Considering the microphone's maximum useful frequency of 80 kHz, the air-coupled method is likely to be a better approach for quantifying the depth of shallow defects.

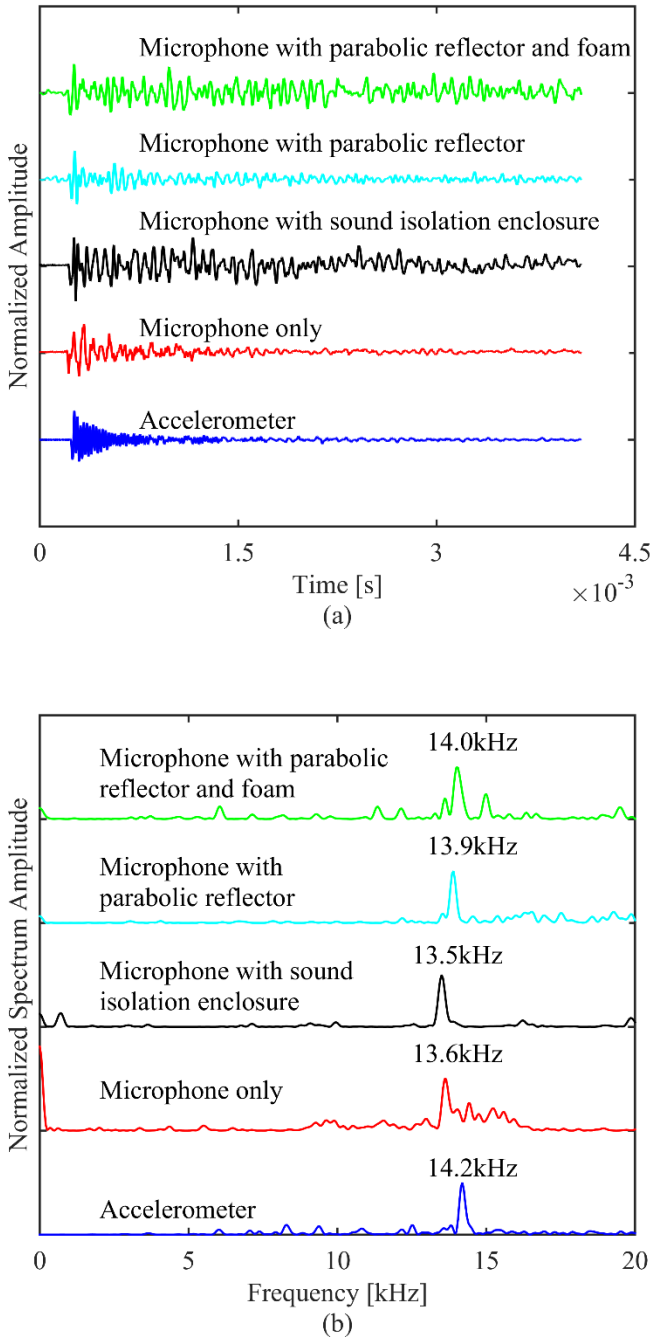

Figure 5.6. Comparison of test results for physically-coupled and air-coupled impact-echo tests performed on defect-free concrete calibration plate: (a) normalized time-domain waveforms; (b) normalized frequency spectra.

5.3 Measurements on Mock-Up Bridge Deck Section with Artificial Defects

In the previous section, physically-coupled and air-coupled impact-echo tests were successfully completed on a solid concrete plate of known thickness. In several of the prior studies, large concrete slabs having artificial defects were also tested in the laboratory, but most had either no reinforcing or only small wire mesh reinforcing, which are not representative of actual concrete bridge decks. The presence of significant rebar cages as used in typical bridge deck designs can complicate the propagation of stress waves in impact-echo testing. To experimentally validate the capabilities of the air-coupled impact-echo testing method for known defects and more realistic conditions, a mock-up reinforced concrete bridge deck section with artificial defects was constructed in the lab. A typical bridge deck design from a Federal Highway Administration design guide by Wassef et al. (2003) was used. The mock-up bridge deck section was cast with a dimensions of 96.0×72.0×8.0 in. (2.44×2.44×2.03 m) using steel formwork and Iowa Department of Transportation (IDOT) M-4 normal strength concrete mix with limestone aggregate.

The bridge deck was designed with one solid defect-free zone in the center, surrounded by a total of eight defects with different sizes and depths simulated by two techniques. Two plastic sheets with a thickness of 0.25 in. (6.35 mm) were cut to size, and baling wire was placed between the sheets running around the outside perimeter to create an air gap, then the edges were sealed with duct tape. The plastic sheets were used to simulate shallow and deep delaminations by varying their embedment depths at predetermined locations. Two circular discs of extruded polystyrene foam board insulation with a thickness of 2 in. were also used to simulate voids within the concrete structure. The

double-layered plastic sheets and foam discs were secured to the rebar cage using rebar ties and baling wire to ensure that they stayed in place during the concrete pouring and vibrating operations. The detailed locations and sizes, as well as types and materials of the defects are summarized in Table 5.1. A photo of the rebar cage and formwork with artificial defects before casting is shown in Fig. 5.7. The as-built plan view and cross-sections are shown in Fig. 5.8.

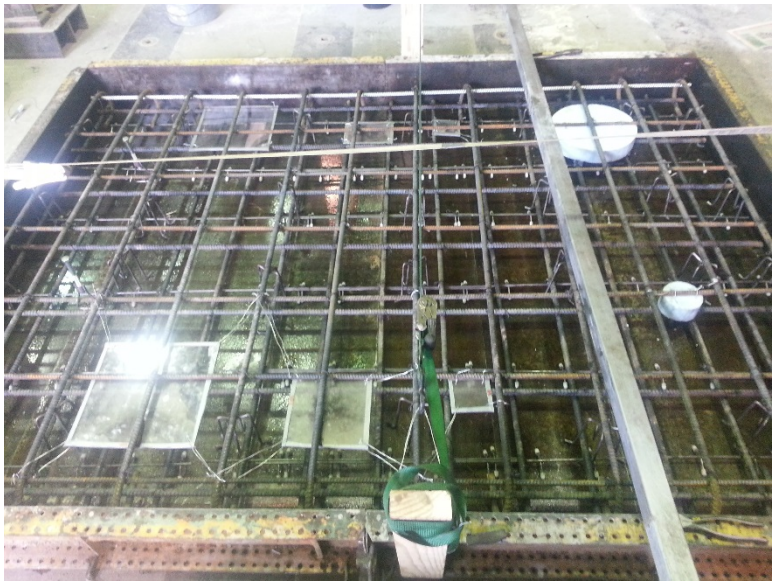

Figure 5.7. Photo of formwork and rebar cage for mock-up bridge deck containing artificial defects before casting.

Table 5.1 Summarization of detailed information of artificial defects

Test Zone	Defect Type	Material Type	Size (in.)	Depth of Defect (in.) (from concrete surface to top of defect)
1	Shallow delamination	Double layered plastic sheet	12 × 12	3.28
2	Deep delamination	Double layered plastic sheet	12 ×12	5.35
3	Shallow delamination	Double layered plastic sheet	8 × 8	3.29
4	Deep delamination	Double layered plastic sheet	7.6 × 5.8	5.91
5	Shallow delamination	Double layered plastic sheet	4 × 4	3.29
6	Deep delamination	Double layered plastic sheet	4 × 4	5.94
7	Void	Foam disc	Dia. = 4	3.44
8	Void	Foam disc	Dia. = 12	3.27
9	None (solid reference zone)	-	48 × 12	8.03

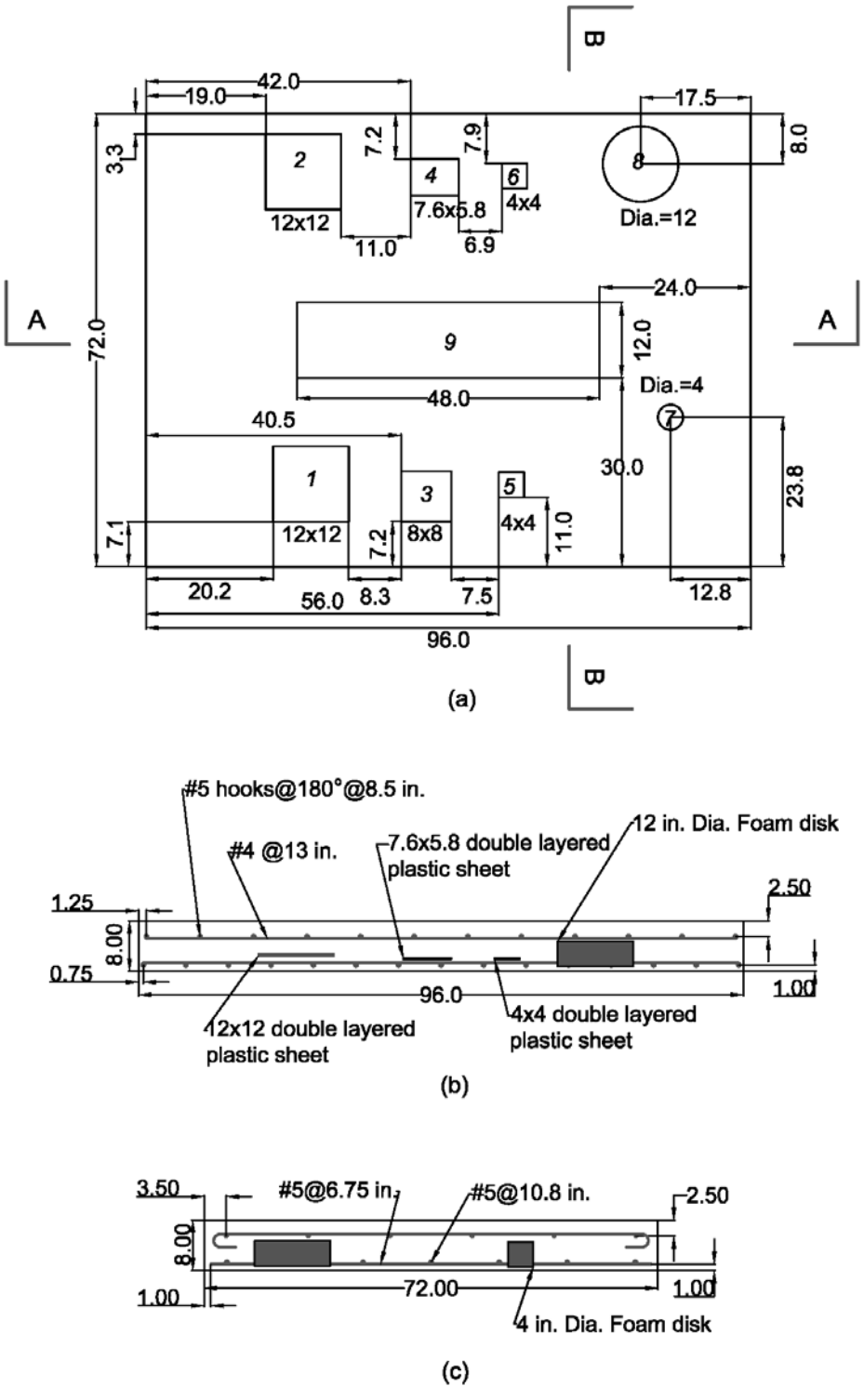

Figure 5.8. Mock-up reinforced concrete bridge deck with artificial defects: (a) as-built plan view; (b) cross-section A-A; (c) cross-section B-B (all dimensions in inches).

5.3.1 P-wave speed measurement test

P-wave speed measurement tests were performed on the surface of the central solid zone 28 days after casting the concrete (Zone No. 9 in Table 5.1). As required by ASTM C 1383, the accelerometers were attached to the concrete plate 0.3 m apart, and accelerations due to the impact of a 6.34 mm diameter steel sphere 0.15 m from the first accelerometer were recorded. The DAQ sampling rate was 1 MHz, and three channels were scanned at effective sampling rates of 333.33 kHz each to eliminate crosstalk as discussed in Chapter 3. A total of 1024 discrete data points were recorded for a sampling period of 3072 μs. The time-domain waveforms and the expanded view of the initial portion of waveforms recorded by the accelerometers are shown in Fig. 5.9. From these measurements, the P-wave travel time ranges from 69 to 72 μs. Therefore, the P-wave speed calculated by Eq. (5.1) ranges from 4167 to 4348 m/s. The actual thickness of the deck was measured with calipers at 16 locations around the perimeter 28 days after casting, and the average value was 8.03 in. Using this thickness and the measured range of P-wave speeds results in a theoretical solid thickness frequency range of 9.81 to 10.23 kHz.

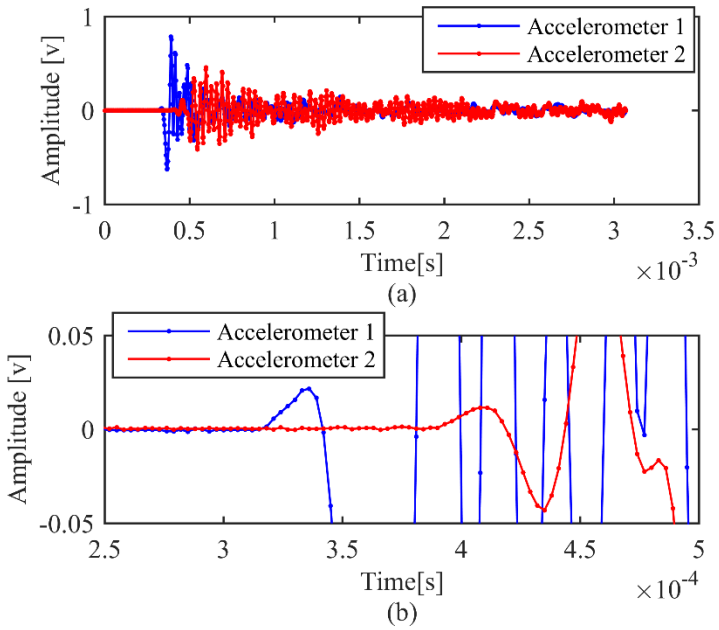

Figure 5.9. Results of P-wave speed measurement test performed on defect-free zone of mock-up reinforced concrete bridge deck: (a) time-domain waveforms; (b) expanded view of initial portion.

5.3.2 Physically-coupled and air-coupled impact-echo tests

Test results for physically-coupled and air-coupled impact-echo tests performed on the solid defect-free and artificial defect zones are shown in Figs. 5.10–5.18. Since the theoretical solid thickness frequency range of 9.81–10.23 kHz falls below the high-frequency accelerometer's maximum usable frequency of 20 kHz, the accelerometer is valid for impact-echo tests on the solid zone. For all physically-coupled and air-coupled impact-echo tests on the bridge deck, the sampling rate was 500 kHz, and 2048 discrete data points were recorded for a sampling duration of 4096 μs. The time-domain signals were converted to the frequency domain by the DTFT numerical integration method discussed in Chapter 3. Test results for the two impact-echo test methods performed on the solid zone are shown in Fig. 5.10. Solid thickness frequencies of 10 kHz and 9.9 kHz were

obtained using the physically-coupled and air-coupled methods, respectively. Substituting these frequencies along with the measured P-wave speed range of 4167–4348 m/s into Eq. 3.21 gives estimated deck thickness ranges of 7.87–8.22 in. and 7.95–8.30 in. for the physically-coupled and air-coupled test methods, respectively. These values are in good agreement with the measured thickness of 8.03 in.

Test results for the 4×4 in. shallow delamination are shown in Fig. 5.11. Compared with the frequency spectrum for the solid defect-free zone shown in Figure 5.10a, one distinct lower-frequency peak exists below 10 kHz in the frequency spectrum for the physically-coupled test method in Fig. 5.11a. This lower-frequency, high-amplitude peak is caused by the flexural mode of vibration of the thin layer above the delamination (Cheng and Sansalone 1993a, Sansalone and Streett 1997). Similarly, a distinct lower-frequency peak is also captured by the air-coupled test method due to the flexural mode of vibration (Fig. 5.11b). These shifted thickness frequencies of 7.875 kHz for the flexural mode of vibration in Fig. 5.11 are in perfect agreement for the accelerometer and microphone. The higher frequency range of the microphone also enables it to capture a high-frequency, low-amplitude peak at 23.15 kHz in Fig. 5.11b, which is beyond the frequency range of the accelerometer. According to Eq. (3.21), this frequency gives a delamination depth of 3.40–3.55 in., which is close to the embedment depth of 3.29 in. measured before pouring the concrete (Table 5.1).

Similar test results for the 8×8 and 12×12 in. shallow delaminations are shown in Figs. 5.12 and 5.13, respectively. For the 8×8 in. defect, two distinct lower-frequency peaks corresponding to the first and second flexural modes of vibration can be seen in the

frequency spectrum of Fig. 5.12. Comparing these shifted thickness frequencies with the ones shown in Fig. 5.11 for a 4×4 in. shallow delamination, the frequencies for the 8×8 in. defect are lower. This behavior is consistent with theory and experiments which indicate that the shifted thickness frequencies corresponding to flexural modes of vibration will decrease as the lateral dimensions of a shallow delamination increase (Cheng and Sansalone 1993a, Lin and Sansalone 1997, Sansalone and Streett 1997). This trend was observed to continue for the 12×12 in. shallow delamination, which gave the lowest shifted thickness frequency of 2.725 kHz (Fig. 5.13b). Additionally, the flexural modes of vibration have been reported to be more easily excited as the lateral dimensions of a delamination increase. However, the data of Fig. 5.11b, 5.12b, and 5.13b appear to indicate that the S_1 ZGV modes actually become more excitable than the flexural modes, as evidenced by the amplitudes of the peaks near 23.5 kHz increasing relative to those of the low-frequency peaks as delamination size increases.

For the 8×8 and 12×12 in. shallow delaminations, the measured higher peak frequencies corresponding to the depth of the delaminations were 23.2 and 23.15 kHz, respectively (Figs. 5.12b and 5.13b). The depth ranges of these two shallow delaminations can be calculated as 3.39–3.54 in. and 3.40–3.55 in., respectively. Both ranges are in reasonable agreement with the as-built depths of 3.29 and 3.28 in. reported in Table 5.1. Results similar to those described above for the shallow delaminations were also observed for the three deep delaminations and two foam-filled voids. Test data for these impact-echo tests are shown in Figs. 5.14–5.18.

The time-domain waveforms and frequency spectra for the 4×4 in. deep delamination are presented in Fig. 5.14 for both test methods. The measured S_1 ZGV (thickness) peak frequencies corresponding to the depth of the upper concrete-delamination interface are 14.15 and 13.4 kHz for the accelerometer and microphone, respectively. The corresponding depth ranges using Eq. (3.21) are 5.57–5.81 in. and 5.88–6.13 in., respectively, which agree well with the as-built depth of 5.94 in. reported in Table 5.1. No flexural-mode frequencies are apparent in the spectra, because (1) the bending stiffness increases with the second moment of area of the flexural section, which is proportional to the cube of the defect depth, and (2) the excitability of the flexural mode will decrease as the lateral defect dimension decreases or defect depth increases. However, significant additional energy between 6 and 14 kHz can be observed in the frequency spectrum of the accelerometer. This energy is caused by the R-waves, whose time-domain waveforms are much larger than those of the P-waves. One method to minimize the effect of the R-waves is to clip the time-domain signal to remove the R-wave portion (Carino et al. 1986b). Similar test results for the 7.6×5.8 in. and 12×12 in. deep delaminations are shown in Figs. 5.15 and 5.16. Each frequency spectrum has a single, distinct peak frequency corresponding to the depth of the delamination.

The impact-echo response for the two foam-filled voids is similar to that of the shallow delaminations; one high-amplitude, low-frequency flexural-mode peak, and one low-amplitude, high-frequency peak for the S_1 ZGV mode between the concrete surface and upper layer of the void can be seen in the microphone frequency spectra. Likewise, the frequency of the flexural mode decreases as the diameter of the void increases. Based on

the high-frequency peaks, the depth of voids with different diameters can also be determined from Eq. (3.21). Test results for the measured defect depths and solid thickness of the concrete plate are summarized in Table 5.2. All test results are in good or reasonable agreement with the as-built measured defect depths.

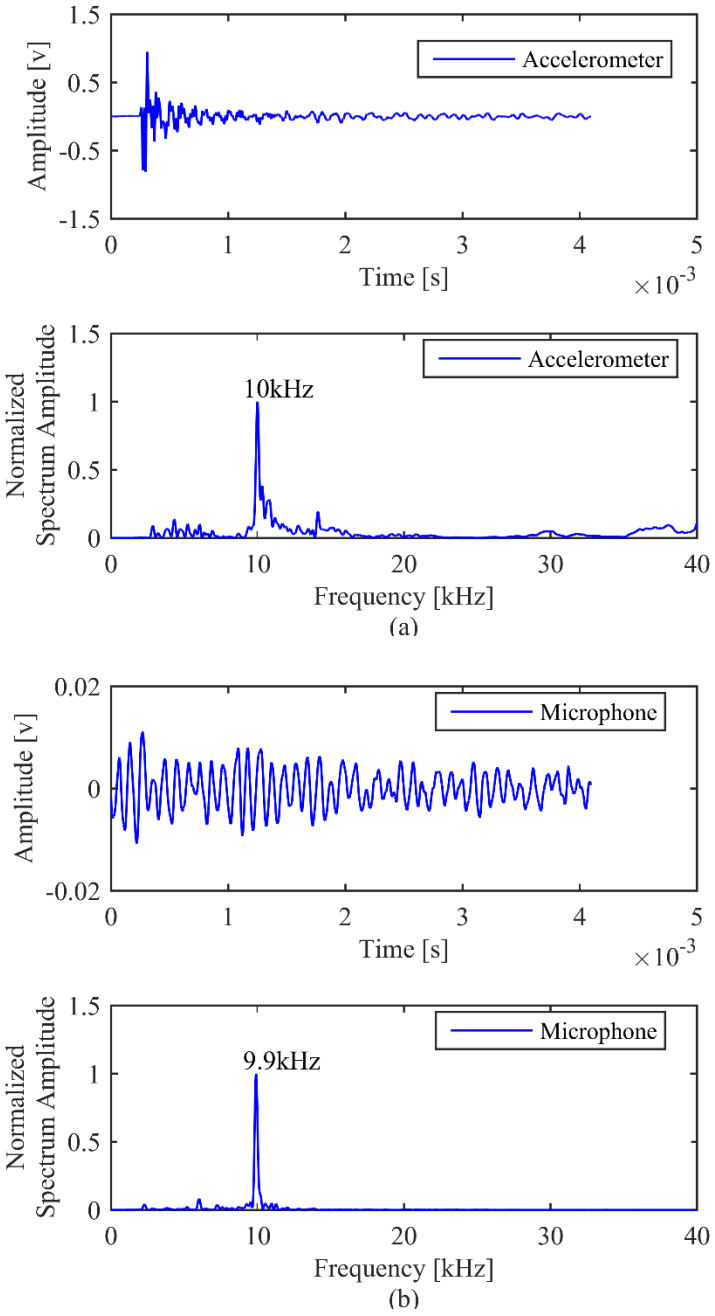

Figure 5.10. Results for impact-echo test on solid defect-free zone of mock-up bridge deck: (a) time-domain waveform and frequency spectrum obtained by accelerometer; (b) time-domain waveform and frequency spectrum obtained by microphone with enclosure.

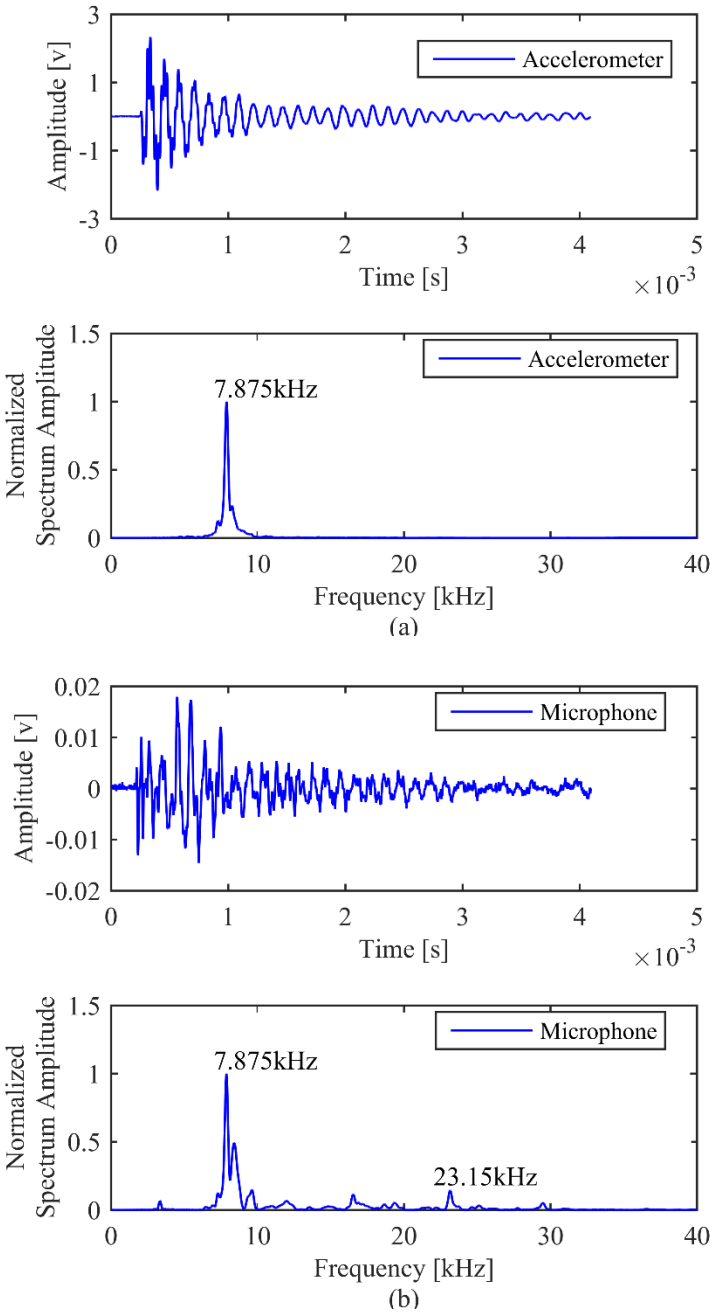

Figure 5.11. Results for impact-echo test on 4×4 in. shallow delamination: (a) time-domain waveform and frequency spectrum obtained by accelerometer; (b) time-domain waveform and frequency spectrum obtained by microphone with enclosure.

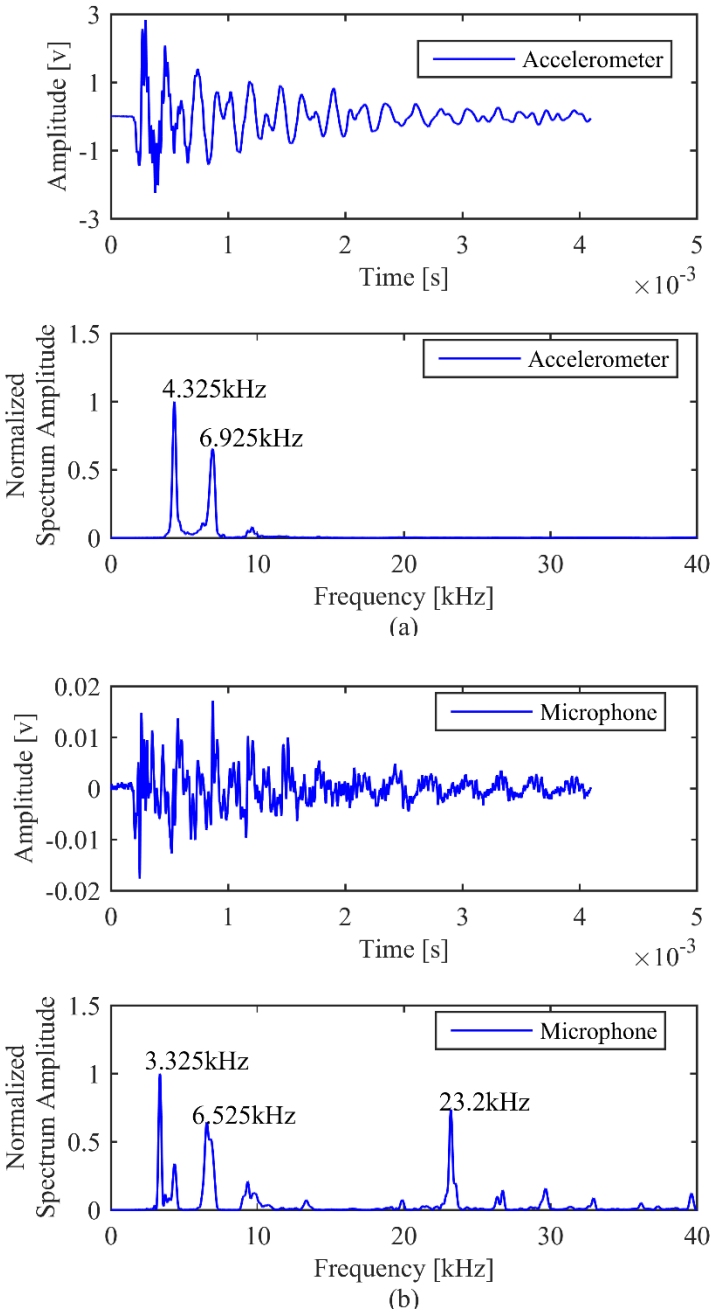

Figure 5.12. Results for impact-echo test on 8×8 in. shallow delamination: (a) time-domain waveform and frequency spectrum obtained by accelerometer; (b) time-domain waveform and frequency spectrum obtained by microphone with enclosure.

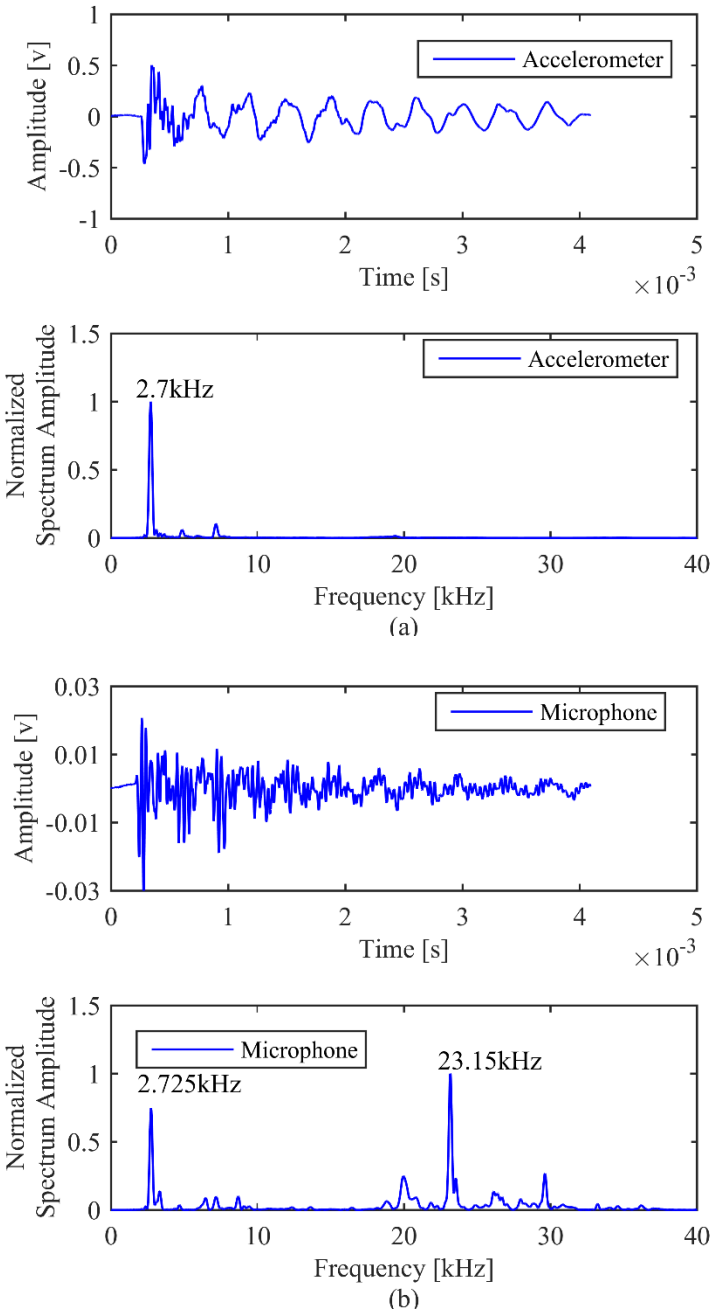

Figure 5.13. Results for impact-echo test on 12×12 in. shallow delamination: (a) time-domain waveform and frequency spectrum obtained by accelerometer; (b) time-domain waveform and frequency spectrum obtained by microphone with enclosure.

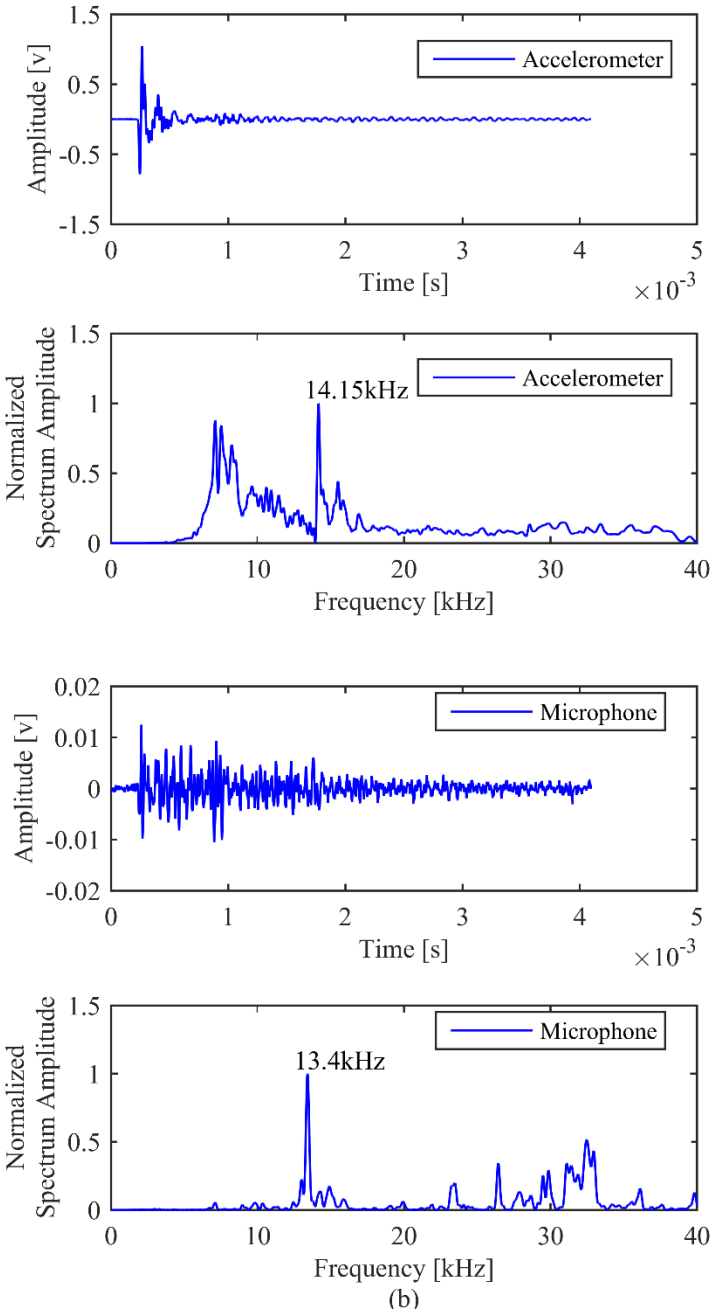

Figure 5.14. Results for impact-echo test on 4×4 in. deep delamination: (a) time-domain waveform and frequency spectrum obtained by accelerometer; (b) time-domain waveform and frequency spectrum obtained by microphone with enclosure.

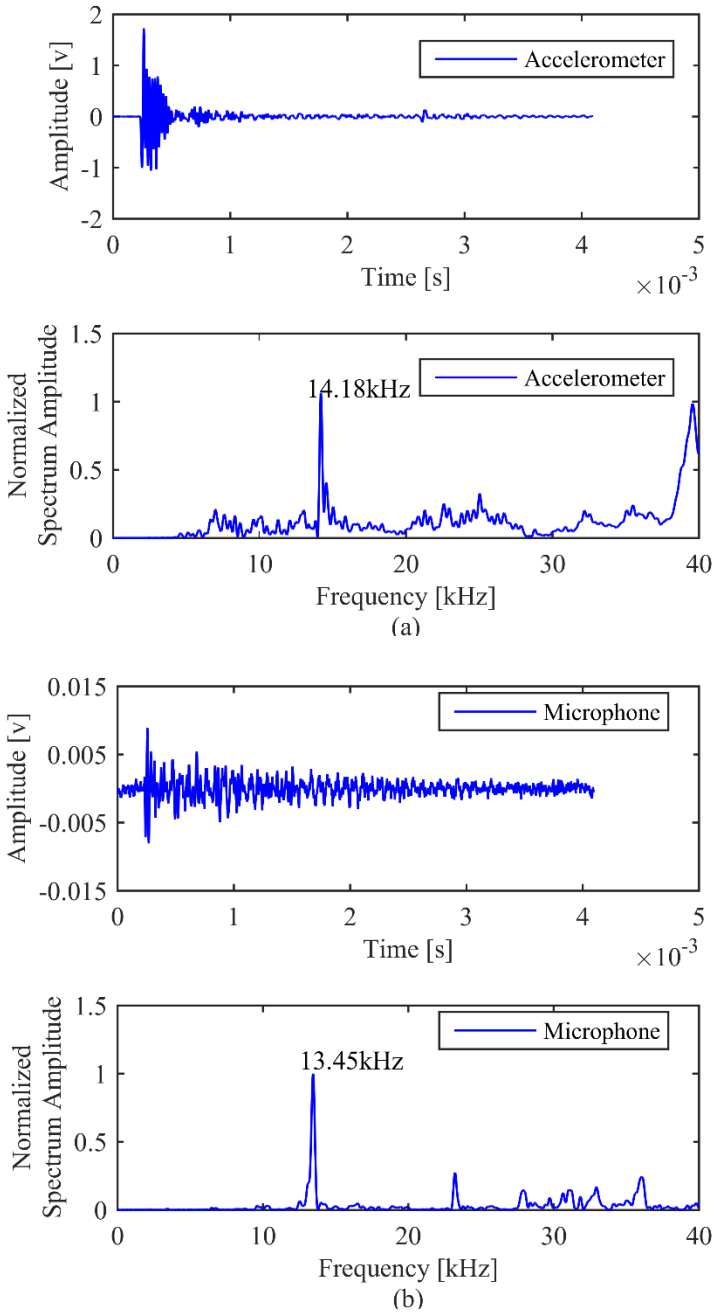

Figure 5.15. Results for impact-echo test on 7.6×5.8 in. deep delamination: (a) time-domain waveform and frequency spectrum obtained by accelerometer; (b) time-domain waveform and frequency spectrum obtained by microphone with enclosure.

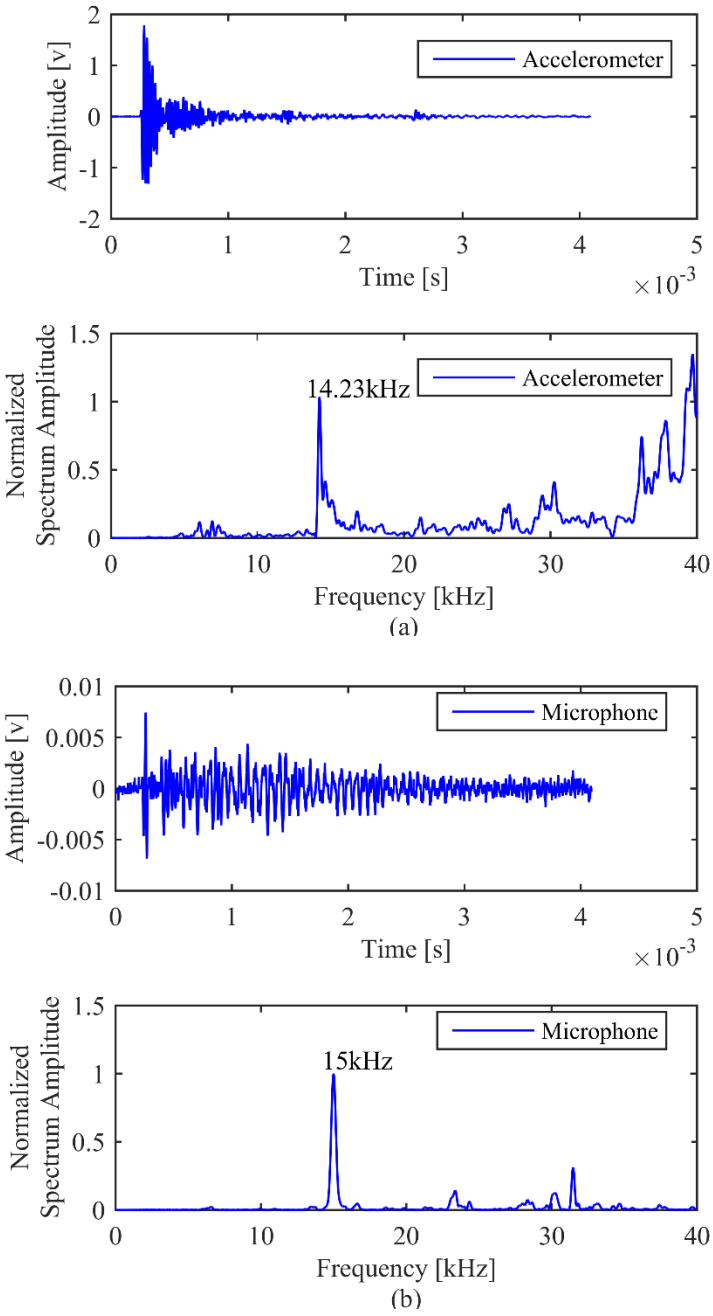

Figure 5.16. Results for impact-echo test on 12×12 in. deep delamination: (a) time-domain waveform and frequency spectrum obtained by accelerometer; (b) time-domain waveform and frequency spectrum obtained by microphone with enclosure.

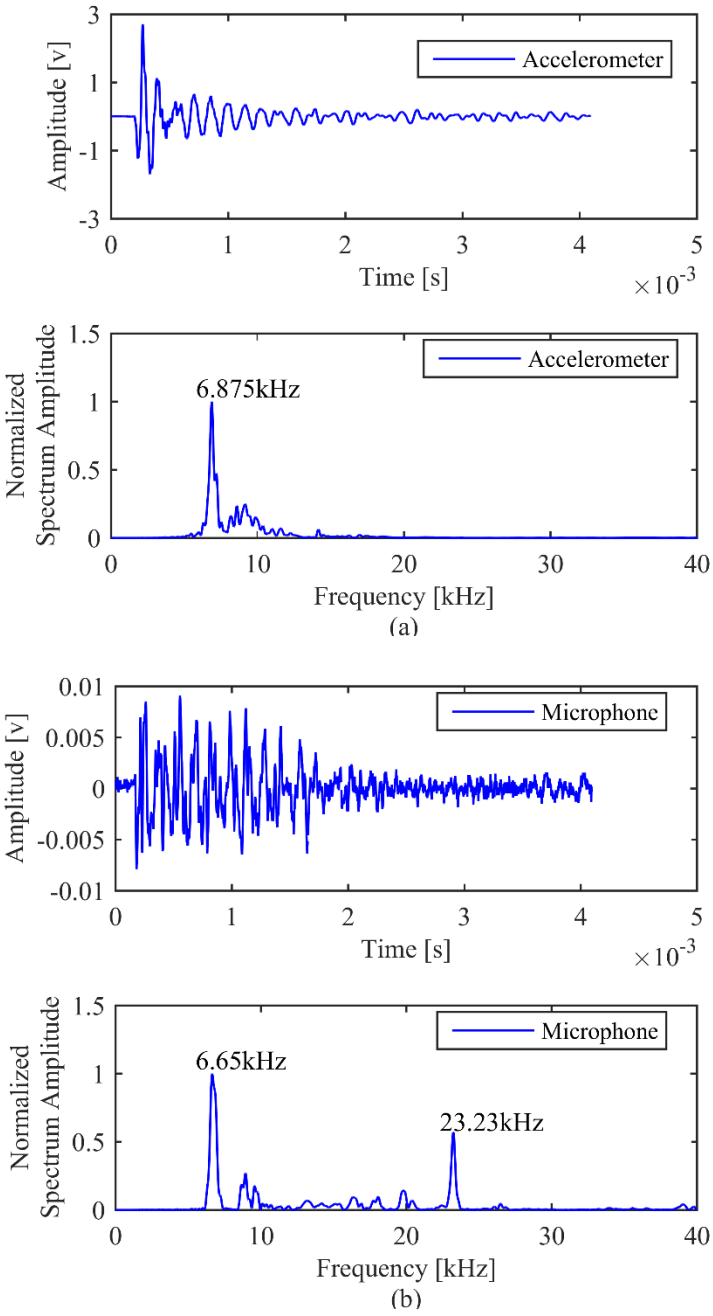

Figure 5.17. Results for impact-echo test on 4 in. diameter foam void: (a) time-domain waveform and frequency spectrum obtained by accelerometer; (b) time-domain waveform and frequency spectrum obtained by microphone with enclosure.

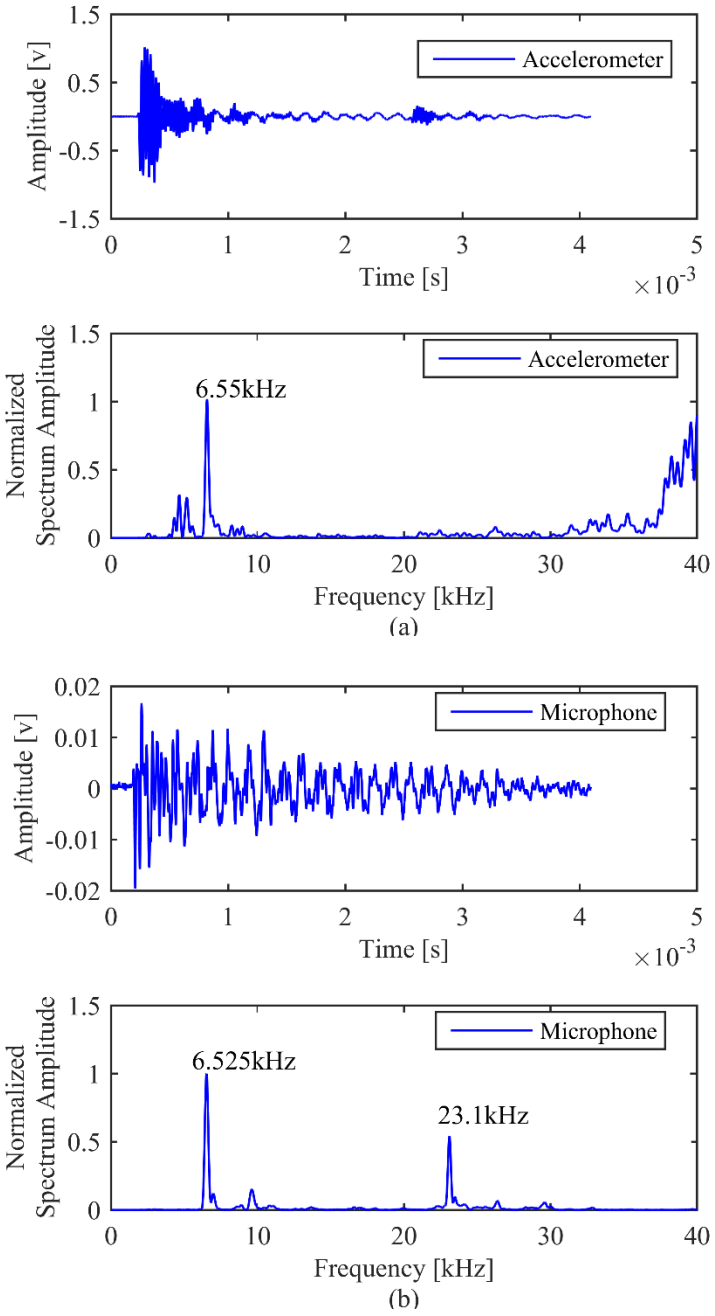

Figure 5.18. Results for impact-echo test on 12 in. diameter foam void: (a) time-domain waveform and frequency spectrum obtained by accelerometer; (b) time-domain waveform and frequency spectrum obtained by microphone with enclosure.

Table 5.2. Test results for measured depth of defects and solid thickness of concrete plate by accelerometer and microphone.

Defect Type	Size (in.)	Depth of Defects (in.) (measured from testing surface to top of defects)		
		As-built	Measured	
Shallow delamination	12×12	3.28	3.40–3.55 (microphone)	
Deep delamination	12×12	5.35	5.53–5.77 (accelerometer)	5.25–5.48 (microphone)
Shallow delamination	8×8	3.29	3.39–3.54 (microphone)	
Deep delamination	7.6×5.8	5.91	5.85–5.79 (accelerometer)	5.85–6.11 (microphone)
Shallow delamination	4×4	3.29	3.40–3.55 (microphone)	
Deep delamination	4×4	5.94	5.57–5.81 (accelerometer)	5.88–6.13 (microphone)
Void	Dia. = 4	3.44	3.39–3.54 (microphone)	
Void	Dia. = 12	3.27	3.41–3.56 (microphone)	
Solid	48×12	8.03	7.87–8.22 (accelerometer)	7.95–8.30 (microphone)

5.3.3 2D-scan of artificial defects by physically-coupled and air-coupled sensors

While the usefulness of impact-echo tests for indicating concrete thickness and defect depth has been demonstrated up to this point, one must first locate the defect in order to know where to perform the tests. Additionally, infrastructure owners are interested in knowing the distribution of defects within a structure, which can be communicated by a map of the structure's integrity. Both of these needs can be met by performing a two-dimensional (2D) array of impact-echo tests (or "2D scan") over the surface of a structure such as a bridge deck or tunnel lining.

To investigate the performance of the air-coupled method in 2D scans, the mock-up bridge deck was scanned using the physically-coupled and air-coupled impact-echo

methods. Scan tests were performed over a grid size of 2 by 2 in. over each of the eight defects using the microphone. For a direct comparison, four of the eight defects were also scanned by the accelerometer, including the 4×4 and 8×8 shallow delaminations, 4×4 deep delamination, and the 7.6×5.8 deep delamination. Contour maps of defect depth were then constructed in MATLAB by plotting the frequency of the tallest peak in the spectrum, for each test point in the grid. As mentioned in Chapter 2, the physically-coupled test method is time-consuming and labor intensive. The efficiency of 2D scanning was greatly improved via the air-coupled test method. For example, scanning a 2D grid of 25 points over one 4×4 defect required approximately 30 minutes with the accelerometer, and only 15 minutes with the microphone.

The two-dimensional contour maps for all defects scanned by the microphone and accelerometer are shown in Figs. 5.19–5.30, with the actual defect locations shown in black. The x and y directions represent the long and short dimension of the concrete plate, respectively. Based on the previous impact-echo test of the solid zone, the solid thickness frequency for the defect-free areas is within 9.81 to 10.23 kHz, represented by the middle of the color scale, which is green to light yellow in the contour maps. Low frequency peaks are represented by cold (blue) colors, meaning that an area may have shallow delaminations, with the frequency corresponding to the flexural mode. Similarly, high frequencies are represented by warm (red) colors, meaning that an area may have deep delaminations, with the frequency representing the thickness mode.

For all defects scanned, the presence of the defect can be identified clearly in the contour maps, and the mapped locations agree fairly well with the actual locations. The

frequency spectra for shallow delaminations are generally dominated by low-frequency peaks (cold colors) corresponding to the flexural mode of vibration. Furthermore, as mentioned previously, the flexural frequencies decrease as the lateral dimensions of the delaminations increase, as expected. Defect locations determined by the microphone are in good agreement with those obtained by the accelerometer. Finally, most defect extents on the 2D maps extend beyond the actual extents due to interpolation of the colors between points in the 2×2 in. grid, and because the stiffness of the surrounding areas is reduced in the presence of defects.

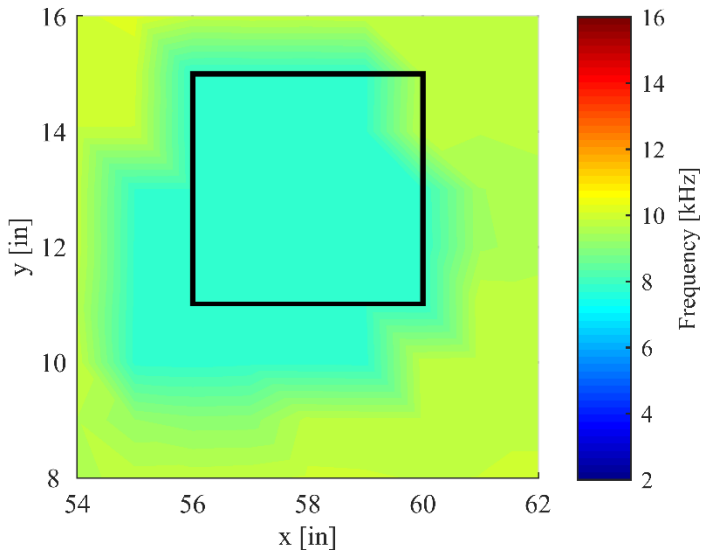

Figure 5.19. Two-dimensional contour map of 4×4 in. shallow delamination obtained by accelerometer.

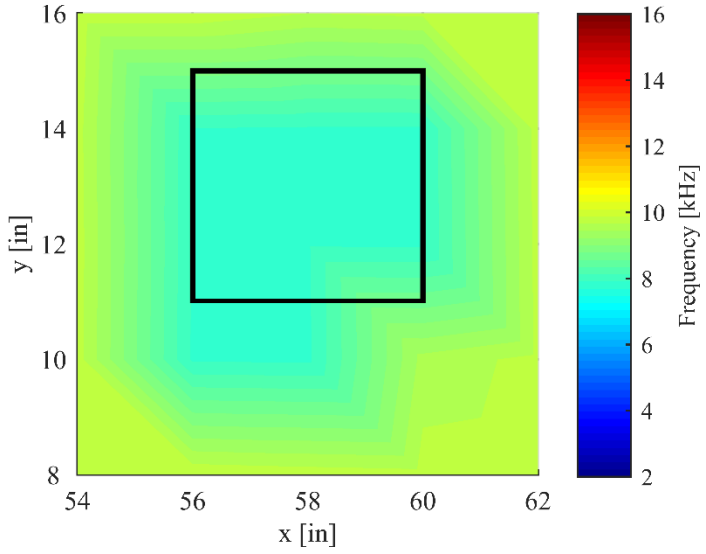

Figure 5.20. Two-dimensional contour map of 4×4 in. shallow delamination obtained by microphone with enclosure.

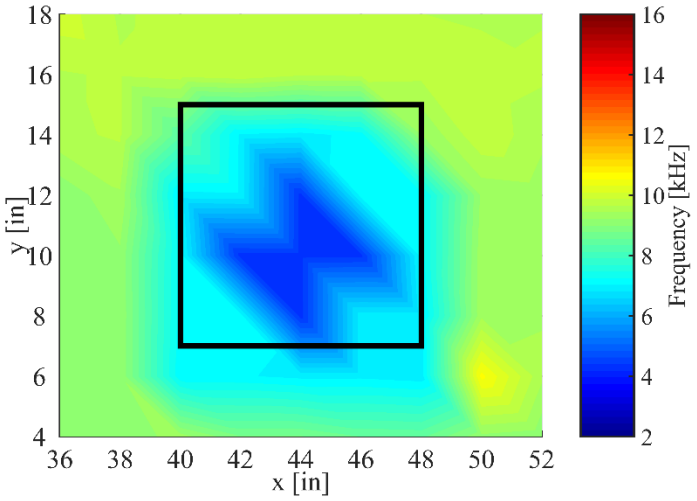

Figure 5.21. Two-dimensional contour map of 8×8 in. shallow delamination obtained by accelerometer.

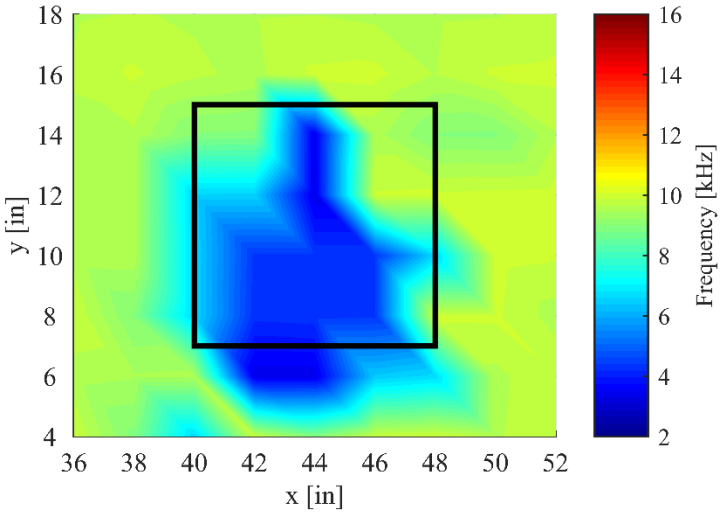

Figure 5.22. Two-dimensional contour map of 8×8 in. shallow delamination obtained by microphone with enclosure.

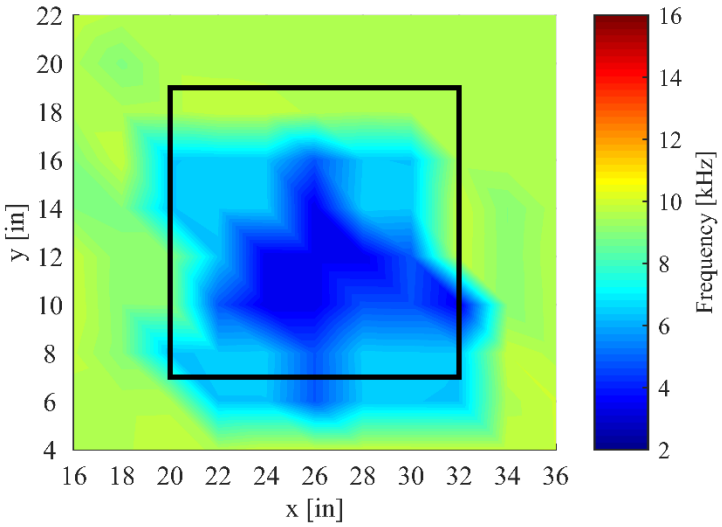

Figure 5.23. Two-dimensional contour map of 12×12 in. shallow delamination obtained by microphone with enclosure.

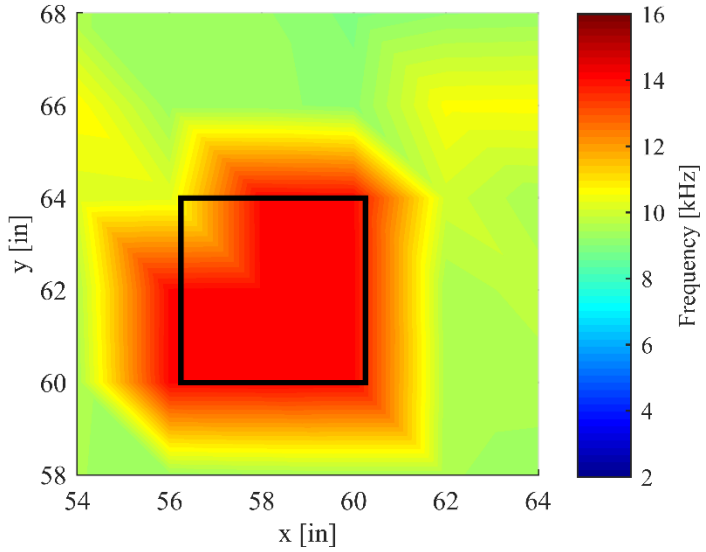

Figure 5.24. Two-dimensional contour map of 4×4 in. deep delamination obtained by accelerometer.

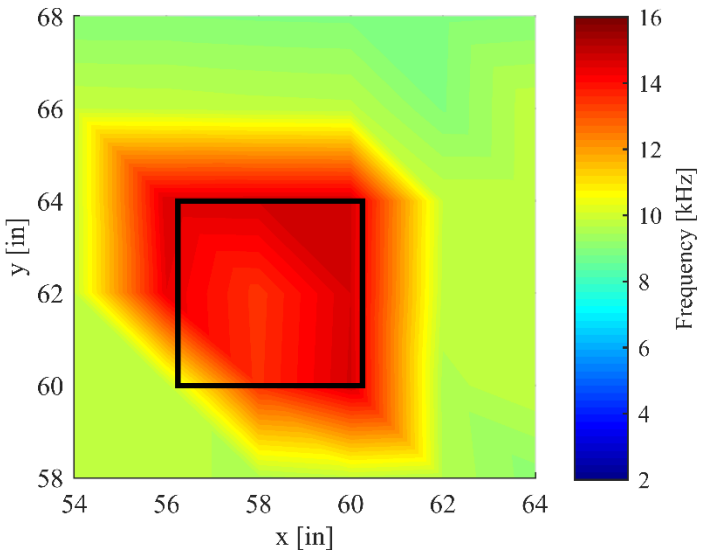

Figure 5.25. Two-dimensional contour map of 4×4 in. deep delamination obtained by microphone with enclosure.

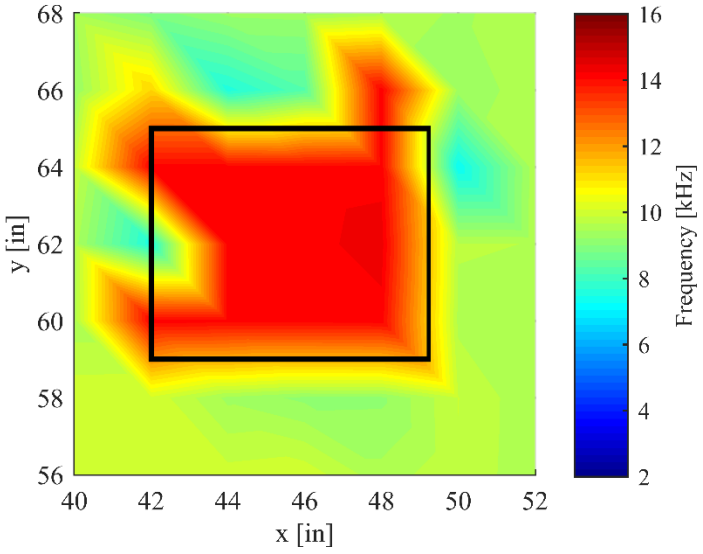

Figure 5.26. Two-dimensional contour map of 7.6×5.8 in. deep delamination obtained by accelerometer.

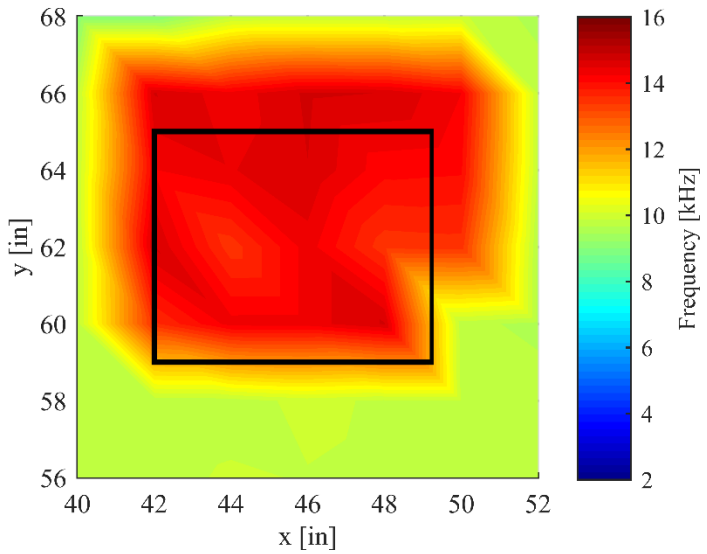

Figure 5.27. Two-dimensional contour map of 7.6×5.8 in. deep delamination obtained by microphone with enclosure.

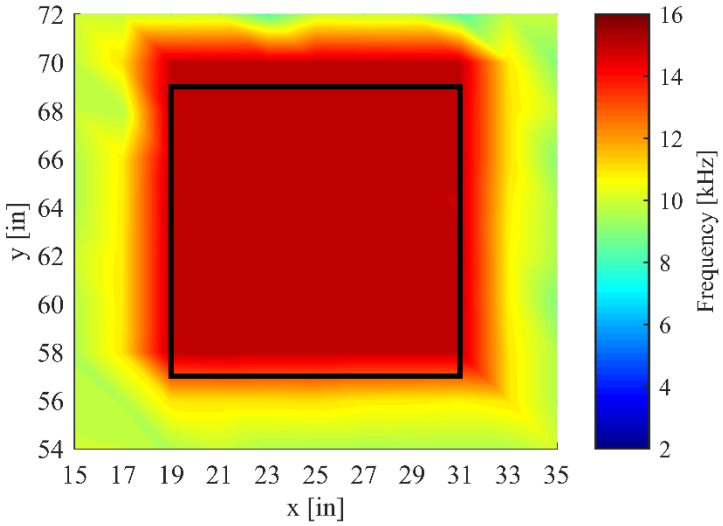

Figure 5.28. Two-dimensional contour map of 12×12 in. deep delamination obtained by microphone with enclosure.

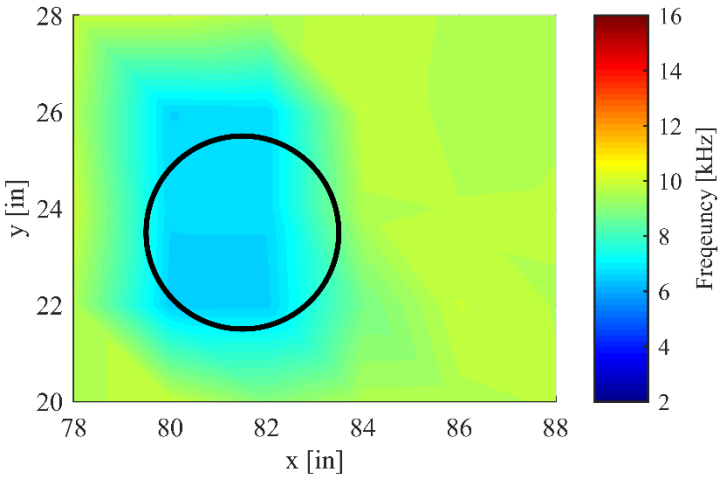

Figure 5.29. Two-dimensional contour map of 4 in. diameter foam-filled void obtained by microphone with enclosure.

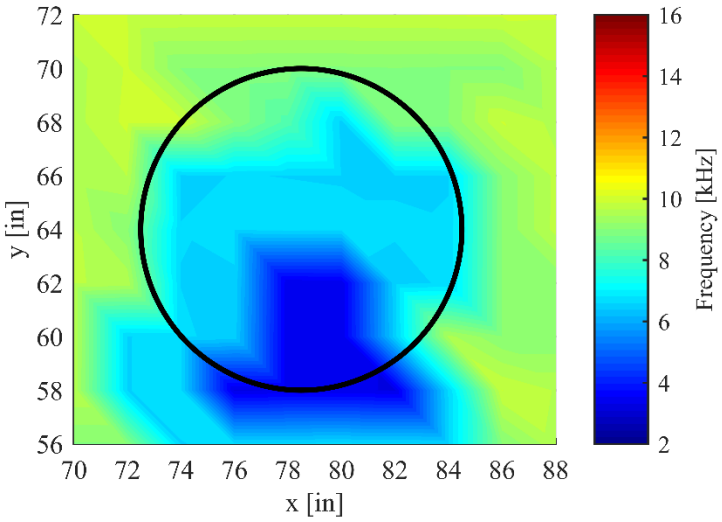

Figure 5.30. Two-dimensional contour map of 12 in. diameter foam-filled void obtained by microphone.

5.3.4 Application of passive and adaptive filters to air-coupled impact-echo test

Although the air-coupled test method greatly increases testing efficiency, it is more sensitive to effects of ambient noise from sources such as traffic and wind. Furthermore, extra peaks due to multiple reflections between the reflector and test surface may appear in the frequency spectrum if a parabolic reflector is used. Minimizing the effects of these noise sources will be indispensable for identifying the appropriate peak frequency in the spectrum.

As demonstrated in the tests of the previous section, a sound isolation enclosure can also provide a relatively quiet environment for the microphone during testing. The enclosure was quicker to set up than the reflector, and allowed closer proximity of the impact to the microphone. Beyond the use of the enclosure, filtering techniques were also examined in this study for application during analysis of the test data to further suppress the effects of noise when the frequency content of the noise is known. One may use the microphone to determine the spectral content of the ambient noise before testing, or even implement active filtering (during post-processing, so no information is lost) if a second microphone is used to record the external noise during an impact-echo test.

Alternatively, passive filters such as high-pass and band-pass filters, can be used for signal processing of an impact-echo test performed on a concrete structure where a reasonable estimate of the solid thickness is known. Once the P-wave speed is determined, the estimated solid thickness can be used to estimate the frequency peak corresponding to the solid thickness from Eq. (3.21). Then, a band-pass filter can be applied to the time-domain signal recorded by the microphone to isolate the solid thickness frequency more

precisely by filtering out all other frequencies outside the band. This process can be done during post-processing so that various filters can be examined without losing any of the original broadband data.

A comparison of the test results with and without band pass filters applied are shown in Fig. 5.31. The test was performed on the defect-free concrete calibration plate via the air-coupled test method. Test results were obtained in four ways; (1) microphone only, (2) microphone with sound isolation enclosure, (3) microphone with parabolic reflector, and (4) microphone with parabolic reflector with foam annulus. As detailed in Section 5.2.2, the solid thickness frequency was determined to be in the range 13.69–14.32 kHz using the measured P-wave speed and measured thickness in Eq. (3.21). A band pass filter was applied to the raw data of the time-domain signal using the filter function in MATLAB, with lower and upper cutoff frequencies of 13.0 and 14.5 kHz. After applying the filter, the time-domain waveforms become more harmonic and frequency spectra become clearer. The dominant solid thickness frequency peak can then be easily identified. However, the filter introduces a short-time delay and the amplitude decreases, meaning some energy is lost due to application of the filter. The delay time for the time-domain signal increases as the filter order increases.

For field air-coupled impact-echo tests, traffic and wind noise might become major issues and affect the quality of time-domain signals. To examine this issue, actual traffic noise was measured using the test microphone (Fig. 5.32). The sampling rate was the same as the air-coupled test method—500 kHz. Based on the frequency spectrum of the traffic noise, the majority of the energy lies below a frequency of 2 kHz. Consequently, a high

pass filter with a cut-off frequency of 2 kHz can be applied either in real-time or during post-processing of data, in conjunction with a sound isolation enclosure. This high pass filter can also be used for tests performed in the laboratory, to diminish noise below 2 kHz due to ambient sources as well as resonance of the sensor and enclosure assembly (Carino et al. 1986b). A comparison of test results with and without a 2 kHz high-pass filter is shown in Fig. 5.33, for an air-coupled test on the 12×12 in. shallow delamination. The low-frequency content is suppressed as expected after applying the high-pass filter. Although the usefulness of simple passive filters as shown here may be somewhat limited, they can be easily implemented if significant noise sources are encountered in the field. For this purpose, it is recommended to record the ambient noise immediately before or after performing a test. If warranted, active noise-cancelling algorithms might also be useful if a second triggered microphone is used to simultaneously record the external noise.

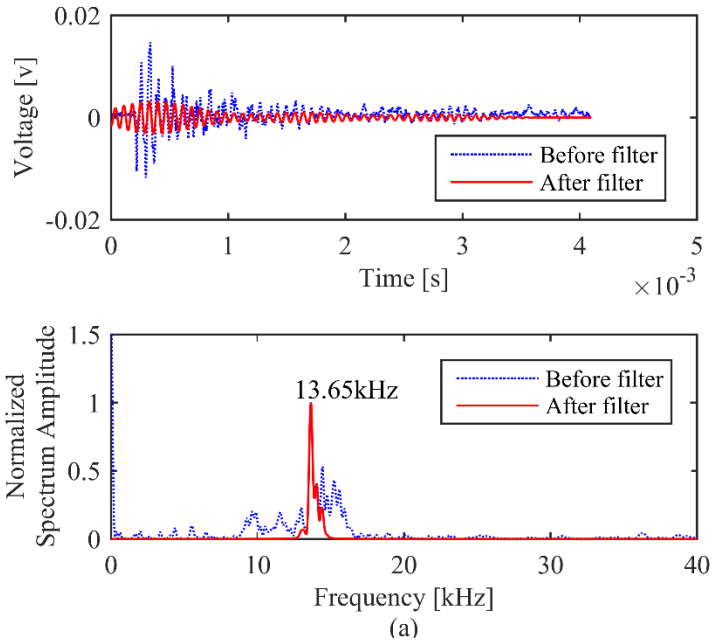

(a)

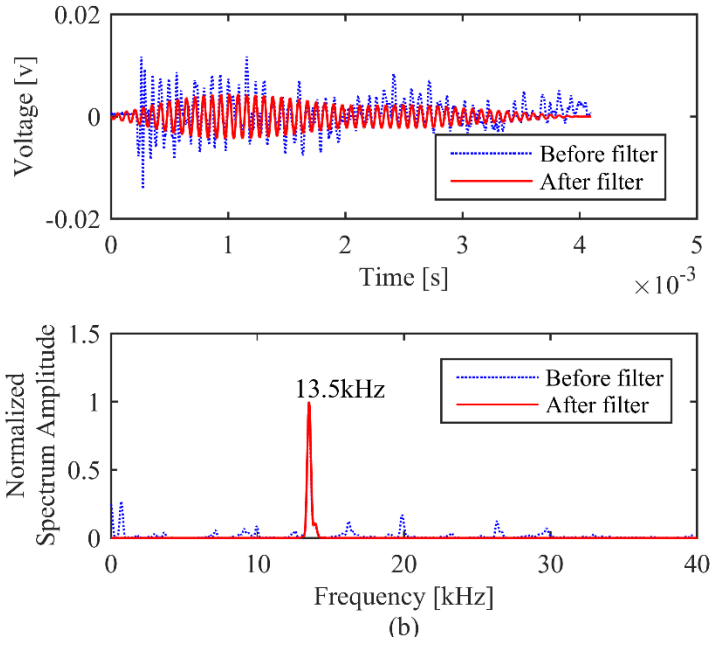
0.02
0
-0.02
Voltage [v]
0
1
2
3
4
5
Time [s]
×10-3
Before filter
After filter
1.5
1
0.5
0
Normalized Spectrum Amplitude
13.5kHz
0
10
20
30
40
Frequency [kHz]

(b)

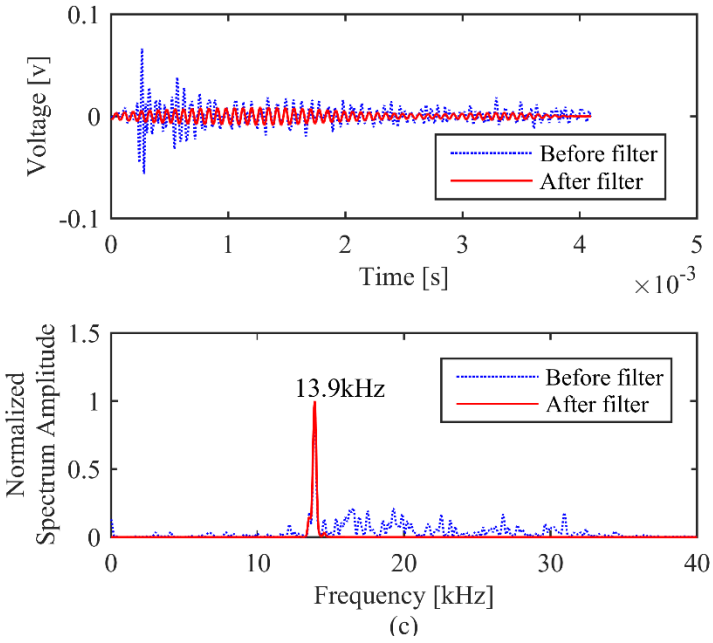
0.1
0
-0.1
Voltage [v]
0
1
2
3
4
5
Time [s]
×10-3
Before filter
After filter
1.5
1
0.5
0
Normalized Spectrum Amplitude
13.9kHz
0
10
20
30
40
Frequency [kHz]

(c)

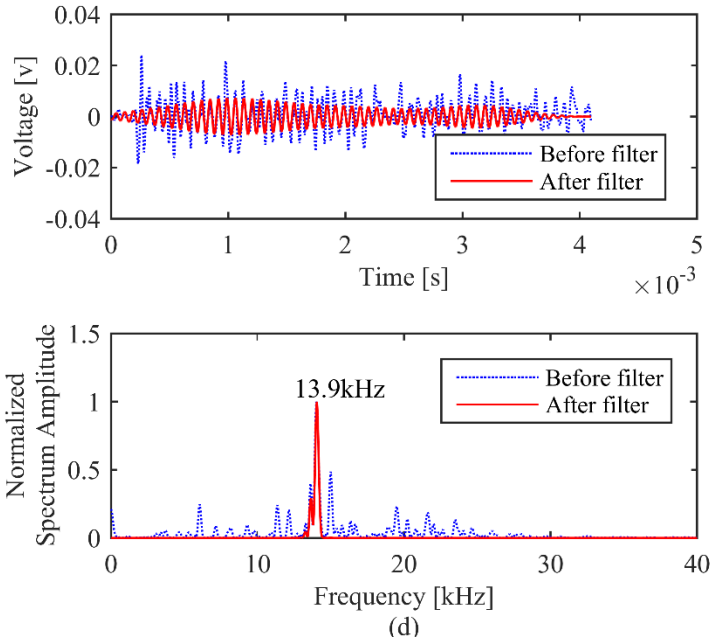

Figure 5.31. Comparison of air-coupled impact-echo tests on defect-free calibration plate, with and without band pass filters: (1) microphone only; (2) microphone with sound isolation enclosure; (3) microphone with parabolic reflector; (4) microphone with parabolic reflector with foam.

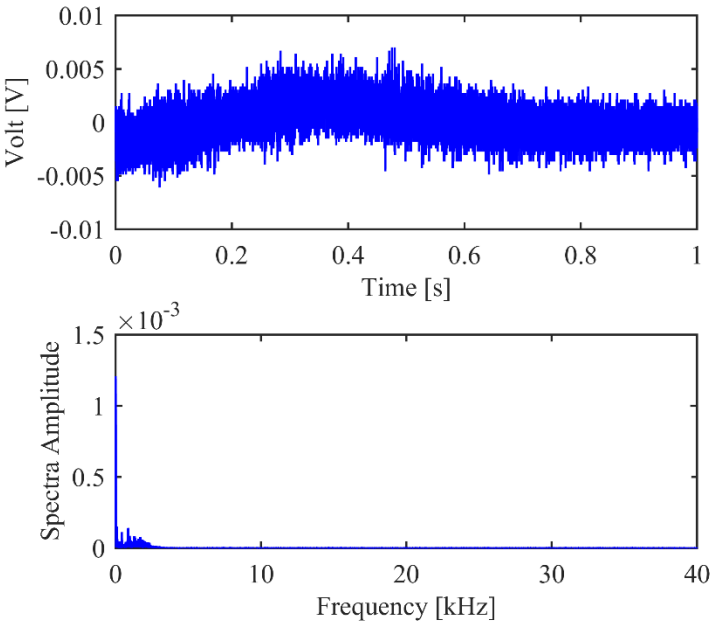

Figure 5.32. Traffic noise measured by microphone.

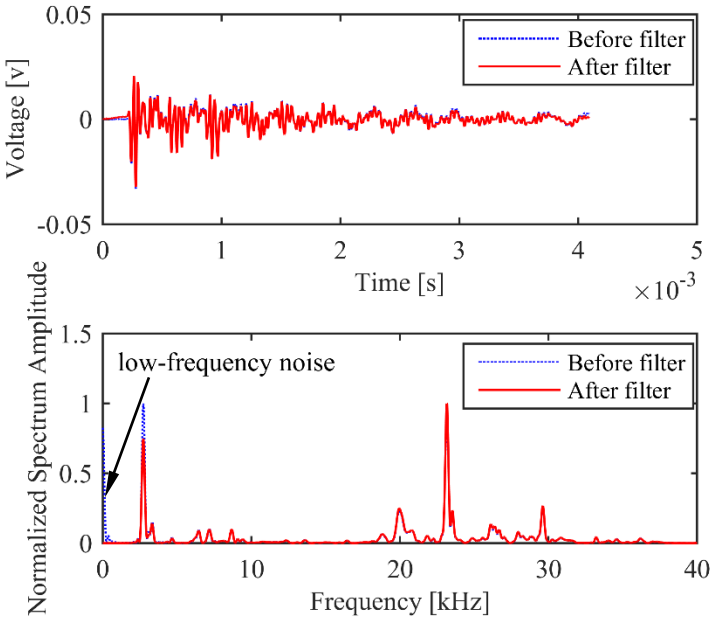

Figure 5.33. Comparison of air-coupled impact-echo tests with and without 2 kHz high-pass filter, performed over 12×12 in. shallow delamination in mock-up bridge deck.

CHAPTER 6. CONCLUSIONS

Practical limitations of the traditional physically-coupled impact-echo test method have led to the recent development of the air-coupled impact-echo test method. The air-coupled method can greatly improve testing efficiency, however, several challenges remain to be overcome before the air-coupled method can be routinely used in practice. These challenges relate to the optimum design of an air-coupled testing system to reduce the effects of ambient external noise from wind, traffic, and machinery. Other researchers have reported that the use of parabolic reflectors or sound isolating enclosures can increase the signal-to-noise ratio for air-coupled impact-echo tests. The performance of these noise reducing measures was further studied and verified in this study by new finite element numerical simulations using COMSOL Multiphysics software, as well as physical experiments in the laboratory. In the experiments, the performance of the air-coupled impact-echo method was verified using a mock-up bridge deck with reinforcing steel details from a typical structural bridge deck design. This is in contrast to most prior studies, which used little or no reinforcing steel, or only small wire mesh which is not representative of the steel content of actual bridge decks.

A new impact-echo testing system was independently developed for this study using an Omega OMB-DAQ-3000 data acquisition unit, a data acquisition program written in LabVIEW, and piezoelectric sensors from PCB Piezotronics, Inc., including two accelerometers, a piezoelectric measurement microphone, and a battery-powered signal conditioner. This new testing system will enable future impact-echo research developments, as the software control program can be freely customized. The testing system was

successfully used to conduct P-wave speed measurement and impact-echo tests by both physically-coupled and air-coupled testing approaches. Experimental issues of crosstalk caused by limitations of the data acquisition unit were resolved. A numerical integration of the Discrete Time Fourier Transform (DTFT) was implemented to in MATLAB to obtain the frequency spectrum of the time-domain measurements with more control than offered by the FFT. Test results indicated that excessively long sampling periods could introduce additional spurious frequency peaks.

A series of FEM-based numerical simulations of the coupled acoustic-structure interaction in air-coupled impact-echo tests with a parabolic reflector were performed using COMSOL to determine the optimum geometry of the parabolic reflector. The results verified that the time-domain signal can be amplified at the focal point and acoustic energy loss can be reduced due to multiple reflections between the reflector and concrete plate. Among four different rim angles examined for the parabolic reflector, a rim angle of 90^{o} was determined to provide the optimum signal enhancement. Additionally, the effect of the height from the receiver (focal) point to the testing surface was also investigated by FEM simulations. Results indicated that the height from the testing surface to receiver for a 90° reflector with a diameter of 0.2 m should be within the range 0.1–0.25 m, with 0.15 m recommended.

Comparisons of laboratory experiments using a microphone with either a parabolic reflector or a sound isolation enclosure revealed that the multiple reflections between the reflector and testing surface give rise to additional undesirable frequency peaks. The isolation enclosure was determined to provide a more practical and efficient testing

procedure than the parabolic reflector. Air-coupled and physically-coupled impact-echo tests were conducted on a defect-free concrete plate and the mock-up bridge deck section. Both methods were able to detect the presence of shallow defects as evidenced by low-frequencies corresponding to the flexural mode of vibration of the concrete section above the defect. Due to its limited frequency range of 20 kHz, however, the accelerometer was not able to measure the high-frequency peaks corresponding to the depth of the deep defects, whereas the microphone could easily measure these peaks. In addition, two-dimensional (2D) air-coupled scanning tests were conducted, and the results processed as 2D contour maps to detect the presence and delineate the extent of the eight artificial defects in the bridge deck. Four of the eight defects were also scanned by the traditional physically-coupled impact-echo approach to access the accuracy and feasibility of the new testing approach. Comparisons of test results between these two methods indicated good agreement, thus validating the air-coupled impact-echo test approach for application to actual reinforced concrete bridge decks. Additionally, post-processing filtering techniques were shown to be useful for isolating the solid thickness frequency for tests on structures for which a reasonable estimate of thickness is known. A high-pass filter with a cut-off frequency of 2 kHz was utilized to eliminate the effects caused by traffic noise or the sensor and isolation enclosure assembly's resonance.

For future studies, several recommendations or improvements can be proposed, based on test results from this study:

1. The accuracy and feasibility of the air-coupled impact-echo test were verified by comparing test results with the physically-coupled testing method. Relative to the

traditional coupled testing approach, the efficiency was greatly improved by the air-coupled test approach. To develop a more practical, simpler, faster, air-coupled, impact-echo test system for lab measurement or in-situ tests, a microphone array or a vehicle mounted test system should be investigated for future studies.

2. The air-coupled test method, in conjunction with a parabolic reflector, amplified the time domain signal and reduced acoustic energy loss. However, extra unwanted frequency peaks were included in the frequency spectrum, due to multiple reflections between reflector and testing surface. Additionally, the size of the reflector investigated in this study was not sufficiently small compared with the size of the test concrete plates constructed in the lab. This will result in inaccuracy and uncertainty of test results. As perfectly parabolic reflectors of arbitrary size and height are not easily found commercially, it is recommended to develop a parabolic reflector using a three-dimensional (3D) printing technique in conjunction with an appropriately sized foam annulus to investigate the effects of blocking ambient noise and improving the quality of the air-coupled impact-echo signal.

3. The application of passive filters to air-coupled impact-echo test data was successfully implemented. However, for considerations of efficiency and accuracy of in-situ tests, it is recommended to develop an active noise-cancellation technique to further improve signal quality.

BIBLIOGRAPHY

ASTM. (1999). "Test Method for Measuring the P-Wave Speed and the Thickness of Concrete Plates Using the Impact-Echo Method." Annual Book of ASTM Standards. ASTM C1383, West Conshohocken, PA.

Burger, H. R., Sheehan, A. F., and Jones, C. H. (2006). *Introduction to applied geophysics: Exploring the shallow subsurface*, WW Norton.

C-04, A. (2010). "Standard test method for measuring the P-Wave speed and the thickness of concrete plates using the impact-echo method." American Society for Testing And Materials (ASTM) USA.

Carino, N. J. "The impact-echo method: An overview." *Proc., 2001 Structures Congress and Exposition, Structures 2001, May 21, 2001 - May 23, 2001*, American Society of Civil Engineers.

Carino, N. J., Sansalone, M., and Hsu, N. N. (1986a). "A point source-point receiver technique for flaw detection in concrete." *Journal of the American Concrete Institute*, 83(2), 199-208.

Carino, N. J., Sansalone, M., and Hsu, N. N. (1986b). "Flaw detection in concrete by frequency spectrum analysis of impact-echo waveforms." *International Advances in Nondestructive Testing*, 12, 117-146.

Cheng, C., and Sansalone, M. (1993a). "Impact-echo response of concrete plates containing delaminations: numerical, experimental and field studies." *Materiaux et constructions*, 26(159), 274-285.

Dai, X., Zhu, J., Tsai, Y.-T., and Haberman, M. R. (2011). "Use of parabolic reflector to amplify in-air signals generated during impact-echo testing." *Journal of the Acoustical Society of America*, 130(4), EL167-EL172.

Gibson, A., and Popovics, J. S. (2005). "Lamb wave basis for impact-echo method analysis." *Journal of Engineering Mechanics*, 131(4), 438-443.

Goldsmith, W. (1965). "Impact: The Theory and Physical Behaviour of Colliding Solids." Edward Arnold Press, Ltd, 4-50.

Kee, S.-H., Gucunski, N., and Fetrat, F. A. "Developing an optimal acoustic reflector for air-coupled impact-echo sensor." *Proc., Nondestructive Characterization for Composite Materials, Aerospace Engineering, Civil Infrastructure, and Homeland Security 2012, March 12, 2012 - March 15, 2012*, SPIE, The Society of Photo-Optical Instrumentation Engineers (SPIE); American Society of Mechanical Engineers.

Krautkrämer, J., and Krautkrämer, H. (1990). *Ultrasonic testing of materials 4 ed*, Springer, Germany.

Kuo, S. M., Lee, B. H., and Tian, W. (2013). "Real-Time Digital Signal Processing: Fundamentals, Implementations and Applications." John Wiley & Sons, 195-209.

Lin, J. M., and Sansalone, M. (1996). "Impact-echo studies of interfacial bond quality in concrete: Part I - effects of unbonded fraction of area." *ACI Materials Journal*, 93(3), 223-232.

Lin, J. M., and Sansalone, M. (1997). "A Procedure for Determining P-Wave Speed in Concrete for Use in Impact-Echo Testing Using a Rayleigh Wave Speed Measurement Technique." *Special Publication*, 168, 137-166.

Luukkala, M., and Meriläinen, P. (1973). "Metal plate testing using airborne ultrasound." *Ultrasonics*, 11(5), 218-221.

Malhotra, V. M., and Carino, N. J. (1991). *CRC handbook on nondestructive testing of concrete*, CRC press.

Olson, H. F., and Wolff, I. (1930). "Sound concentrator for microphones." *The Journal of the Acoustical Society of America*, 1(2A), 173-173.

Proctor, T. (1982). "Some details on the NBS conical transducer." *Journal of Acoustic emission*, 1, 173-178.

Ryden, N., Lowe, M. J. S., Cawley, P., and Park, C. B. "Non-contact surface wave measurements using a microphone." *Proc., 19th Symposium on the Application of Geophysics to Engineering and Environmental Problems: Geophysical Applications for Environmental and Engineering Hazzards - Advances and Constraints, SAGEEP 2006, April 2, 2006 - April 6, 2006*, Environmental and Engineering Geophysical Society (EEGS), 1110-1115.

Sansalone, M. (1997). "Impact-echo: The complete story." *ACI Structural Journal*, 94(6), 777-786.

Sansalone, M., and Carino, N. J. (1986). *Impact-echo: a method for flaw detection in concrete using transient stress waves*, US Department of Commerce, National Bureau of Standards, Center for Building Technology, Structures Division.

Sansalone, M., and Carino, N. J. (1987). "Transient impact response of plates containing flaws." *Journal of Research of the National Bureau of Standards (United States)*, 92(6), 369-381.

Sansalone, M., Carino, N. J., and Hsu, N. N. (1987a). "A finite element study of transient

wave propagation in plates." *Journal of Research of the National Bureau of Standards (United States)*, 92(4), 267-278.

Sansalone, M., Carino, N. J., and Hsu, N. N. (1987b). "A finite element study of the interaction of transient stress waves with planar flaws." *Journal of Research of the National Bureau of Standards (United States)*, 92(4), 279-290.

Sansalone, M., and Streett, W. (1997). "Impact-echo: nondestructive testing of concrete and masonry." Bullbrier Press Jersey Shore, PA.

Schubert, F., and Köhler, B. (2008). "Ten lectures on impact-echo." *Journal of Nondestructive Evaluation*, 27(1-3), 5-21.

Sheriff, R. E., and Geldart, L. P. (1995). *Exploration seismology*, Cambridge university press.

Tinkey, Y., Olson, L. D., Miller, P. K., and Tanner, J. E. (2011). "Vehicle-Mounted Bridge Deck Scanner." *Transportation Research Board 90th Annual Meeting*Washington DC, 19p.

Viktorov, I. A. (1967). *Rayleigh and Lamb waves: physical theory and applications*, Plenum Press.

Wahlström, S. (1985). "The parabolic reflector as an acoustical amplifier." *AES: Journal of the Audio Engineering Society*, 33(6), 418-429.

Wassef, W. G., Smith, C., Clancy, C. M., and Smith, M. J. (2003). “Comprehensive Design Example for Prestressed Concrete (PSC) Girder Superstructure Bridge with Commentary”, Report to the Federal Highway Administration, Report No. FHWA NHI - 04-043, November, 2003.

Zhu, J. (2005). "Non-contact NDT of concrete structures using air coupled sensors." *phD dissertation*, University of Illinois at Urbana-Champaign.

Zhu, J., and Popovics, J. (2002). "Non-contact detection of surface waves in concrete using an air-coupled sensor." *AIP Conference Proceedings*, 615(1), 1261-1268.

Zhu, J., and Popovics, J. (2005). "Non-contact imaging for surface-opening cracks in concrete with air-coupled sensors." *Materials and structures*, 38(9), 801-806.

Zhu, J., and Popovics, J. S. (2007). "Imaging concrete structures using air-coupled impact-echo." *Journal of Engineering Mechanics*, 133(6), 628-640.

Zhu, J., Popovics, J. S., and Schubert, F. (2004). "Leaky Rayleigh and Scholte waves at the fluid-solid interface subjected to transient point loading." *Journal of the*

Acoustical Society of America, 116(4 I), 2101-2110.

Zoeppritz, K. (1919). "VII b. Über Reflexion und Durchgang seismischer Wellen durch Unstetigkeitsflächen." *Nachrichten von der Gesellschaft der Wissenschaften zu Göttingen, Mathematisch-Physikalische Klasse*, 1919, 66-84.

APPENDIX A. MATLAB CODE FOR PROCESSING IMPACT-ECHO TEST RESULTS

```
%% Numerical Integration Method Verification
clear all
close all
clc

% Global definition
Fs=1e6/2;
N=1024;
dt=1/Fs;
t=0:dt:(N-1)*dt;
w1=2*pi*5e3;
w2=2*pi*10e3;
% Sine function
Xt=0.5*sin(w1*t)+sin(w2*t);
% FFT
NFFT = 2^nextpow2(N); % Next power of 2 from length of y
Y_FFT=fft(Xt,NFFT)/N;
f_FFT = Fs/2*linspace(0,1,NFFT/2+1);

% Numerical integration
i=sqrt(-1);
f_min=0e3;
f_max=Fs/2;
df=50;
f=f_min:df:f_max;

for j=1:length(f)
```

```
    freq=f(j);
    Y_Xt=Xt.*exp(-i*2*pi*freq*t);
    TRP_Xt(j)=trapz(t,Y_Xt);
end;

figure(1)
subplot(211);
plot(t,Xt,'b');
xlabel({'Time [s]','(a)'});
ylabel('Amplitude');
axis([0 2048e-6 -2.0 2.0]);
set(gca,'xtick',0:512e-6:2048e-6);
fontstyle('times new roman');

subplot(212);
plot(f_FFT/1e3,2*abs(Y_FFT(1:NFFT/2+1))./max(2*abs(Y_FFT(1:NFFT/2+
1))),'r');hold on;...
    plot(f/1e3,abs(TRP_Xt)./max(abs(TRP_Xt)),'k');
xlabel({'Frequency [kHz]','(b)'});
ylabel({'Normalized','Amplitude Spectrum'});
axis([0 50 0 1.5]);
text(0,1,sprintf('4.883kHz\n(FFT)'));
text(15,0.75,'5kHz');
text(0,1.4,'9.766kHz(FFT)');
text(15,1.25,'10kHz');
legend('FFT',sprintf('Numerical\nIntegration'));
fontstyle('times new roman');

set(gcf, 'PaperPositionMode', 'manual');
```

```
set(gcf, 'PaperUnits', 'inches');
set(gcf, 'PaperPosition', [1 1 4 4]);
print(figure(1), '-r600', '-dtiff', 'FFTvsNumericalIntegration.tiff');
```

```
%% Physically coupled IE test performed by FFT & Numerical Integration
method
clear all
close all
clc

v1=xlsread('IE_test_Acc_500k_2048.xlsx','sheet1','A2:A2049');

%Global difinition
Fs=1e6/2;
N1=2048;
dt=1/Fs;
t1=0:dt:(N1-1)*dt;
i=sqrt(-1);
df=1;
f_min=0e3;
f_max=Fs/2;
f=f_min:df:f_max;

% FFT
NFFT = 2^nextpow2(N2); % Next power of 2 from length of y
Y_FFT_v2=fft(v2,NFFT)/N2;
f_FFT = Fs/2*linspace(0,1,NFFT/2+1);
% Numerical Integration (DTFT)
for j=1:length(f)
```

```
    freq=f(j);
    Yv1=v1'.*exp(-i*2*pi*freq*t1);
    TRPv1(j)=trapz(t1,Yv1);
end;

figure(1)
subplot(211);
plot(t2,v2,'b');
xlabel({'Time [s]','(a)'});
ylabel('Amplitude [v]');
axis([0 5e-3 -2 2]);
fontstyle('times new roman');

subplot(212);
c=2*abs(Y_FFT_v2(1:NFFT/2+1));
d=c(1:128,:);
[Max_v2,I_v2]=max(d);
 plot(f_FFT/1e3,(2*abs(Y_FFT_v2(1:NFFT/2+1))./Max_v2).^2,'r');hold
on;...
    plot(f/1e3,(abs(TRPv2)/max(abs(TRPv2))).^2,'b');
xlabel({'Frequency [kHz]','(b)'});
ylabel({'Normalized','Amplitude Spectrum'});
axis([0 f_max/1e3 -0.005 1.5]);
text(5,1.3,'14.16kHz(FFT)');
text(16,1.3,'14.2kHz');
legend('FFT','Numerical Integration','location','west');
fontstyle('times new roman');

set(gcf, 'PaperPositionMode', 'manual');
```

```
set(gcf, 'PaperUnits', 'inches');
set(gcf, 'PaperPosition', [1 1 4 4]);
print(figure(1), '-r600', '-dtiff', 'IE_test_Acc_FFT vs Numerical
IntegrationN=2048@500kHz.tiff');
```

```
%% IE test performed by Accelerometer @500kHz with different
...record lengths(2048, 4096,8192, 16384us)
clear all
close all
clc

v1=xlsread('IE_test_Acc_500k_1024.xlsx','sheet1','A2:A1025');
v2=xlsread('IE_test_Acc_500k_2048.xlsx','sheet1','A2:A2049');
v3=xlsread('IE_test_Acc_500k_4096.xlsx','sheet1','A2:A4097');
v4=xlsread('IE_test_Acc_500k_8192.xlsx','sheet1','A2:A8193');

Fs=1e6/2;
N1=1024;
N2=2048;
N3=4096;
N4=8192;
dt=1/Fs;
t1=0:dt:(N1-1)*dt;
t2=0:dt:(N2-1)*dt;
t3=0:dt:(N3-1)*dt;
t4=0:dt:(N4-1)*dt;
i=sqrt(-1);
df=50;
f_min=0e3;
```

```
f_max=20e3;
f=f_min:df:f_max;

for j=1:length(f)
    freq=f(j);
    Yv1=v1'.*exp(-i*2*pi*freq*t1);
    TRPv1(j)=trapz(t1,Yv1);
    Yv2=v2'.*exp(-i*2*pi*freq*t2);
    TRPv2(j)=trapz(t2,Yv2);
    Yv3=v3'.*exp(-i*2*pi*freq*t3);
    TRPv3(j)=trapz(t3,Yv3);
    Yv4=v4'.*exp(-i*2*pi*freq*t4);
    TRPv4(j)=trapz(t4,Yv4);
end;

figure(1)
subplot(421)
plot(t1,v1,'b');
xlabel('(a)');
ylabel('Amplitude [v]');
axis([0 2.048e-3 -2 2]);
set(gca,'xtick',0:1.024*1e-3:2.048*1e-3);
fontstyle('times new roman');

subplot(422)
 plot(f/1e3,(abs(TRPv1)/max(abs(TRPv1))).^2,'b');
xlabel('(b)');
ylabel({'Normalized';'Amplitude Spectrum'});
text(13,1.2,'14.3kHz');
```

```
axis([0 f_max/1e3 -0.005 1.5]);
fontstyle('times new roman');

subplot(423)
plot(t2,v2,'b');
xlabel('(c)');
ylabel('Amplitude [v]');
axis([0 4.096e-3 -2 2]);
set(gca,'xtick',0:1.024*1e-3:4.096*1e-3);
fontstyle('times new roman');

subplot(424)
 plot(f/1e3,(abs(TRPv2)/max(abs(TRPv2))).^2,'b');
xlabel('(d)');
ylabel({'Normalized';'Amplitude Spectrum'});
axis([0 f_max/1e3 -0.005 1.5]);
text(13,1.2,'14.2kHz');
fontstyle('times new roman');

subplot(425)
plot(t3,v3,'b');
xlabel('(e)');
ylabel('Amplitude [v]');
axis([0 8.192e-3 -2 2]);
set(gca,'xtick',0:2.048*1e-3:8.192*1e-3);
fontstyle('times new roman');

subplot(426)
 plot(f/1e3,(abs(TRPv3)/max(abs(TRPv3))).^2,'b');
```

```
xlabel('(f)');
ylabel({'Normalized';'Amplitude Spectrum'});
axis([0 f_max/1e3 -0.005 1.5]);
text(13,1.2,'14.15kHz');
fontstyle('times new roman');

subplot(427)
plot(t4,v4,'b');
xlabel({'Time [s]','(g)'});
ylabel('Amplitude [v]');
axis([0 16.384e-3 -2 2]);
set(gca,'xtick',0:4.096*1e-3:16.384*1e-3);
fontstyle('times new roman');

subplot(428)
 plot(f/1e3,(abs(TRPv4)/max(abs(TRPv4))).^2,'b');
xlabel({'Frequency [kHz]','(h)'});
ylabel({'Normalized';'Amplitude Spectrum'});
axis([0 f_max/1e3 -0.005 1.5]);
text(13,1.2,'14.1kHz');
fontstyle('times new roman');

set(gcf, 'PaperPositionMode', 'manual');
set(gcf, 'PaperUnits', 'inches');
set(gcf, 'PaperPosition', [1 1 6.5 7]);
print(figure(1), '-r600', '-dtiff',
'IE_test_Acc_Frequency_500kHz2@different time record length1.tiff');
```

```
%% P-wave Speed Measurement Test with Crosstalk Issues
```

```
clear all
close all
clc

% Global Defiition
Fs1=1e6/2;
Fs2=1e6/3;
dt1=1/Fs1;
dt2=1/Fs2;
N=1024;
T1=N/Fs1;
T2=N/Fs2;
t1=0:dt1:(N-1)*dt1;
t2=0:dt2:(N-1)*dt2;

% Fs=500kHz, 2 channels
v1=xlsread('P_wave_crosstalk_500k2ch_1024.xlsx','sheet1','A2:A1025');
v2=xlsread('P_wave_crosstalk_500k2ch_1024.xlsx','sheet1','B2:B1025');
% Fs=333kHz, 3 channels
v3=xlsread('P_wave_333k3ch_1024.xlsx','sheet1','A2:A1025');
v4=xlsread('P_wave_333k3ch_1024.xlsx','sheet1','C2:C1025');
% Fs=333kHz, 2 channels
v5=xlsread('P_wave_333k2ch_1024.xlsx','sheet1','A2:A1025');
v6=xlsread('P_wave_333k2ch_1024.xlsx','sheet1','B2:B1025');

figure(1)
subplot(321);
plot(t1,v1-v1(1),'b-');hold on;plot(t1,v2-v2(1),'r-');
xlabel('(a)');
```

```
ylabel('Amplitude [v]');
set(gca,'ytick',-2:1.0:2);
axis([0 2.5e-3 -2 2]);
fontstyle('times new roman');

subplot(322);
plot(t1,v1-v1(1),'b-');hold on;plot(t1,v2-v2(1),'r-');
xlabel('(b)');
ylabel('Amplitude [v]');
axis([2e-4 4.5e-4 -0.15 0.25]);
set(gca,'ytick',-0.15:0.1:0.25);
fontstyle('times new roman');

subplot(323);
plot(t2,v5-v5(1),'b-');hold on;plot(t2,v6-v6(1),'r-');
xlabel('(c)');
ylabel('Amplitude [v]');
axis([0 3.5e-3 -2 2]);
set(gca,'xtick',0:0.5*1e-3:3.5*1e-3);
set(gca,'ytick',-2:1:2);
fontstyle('times new roman');

subplot(324);
plot(t2,v5-v5(1),'b-');hold on;plot(t2,v6-v6(1),'r-');
xlabel('(d)');
ylabel('Amplitude [v]');
axis([2.5e-4 6.01e-4 -0.15 0.25]);
set(gca,'xtick',2.5*1e-4:0.5*1e-4:6.0*1e-4);
set(gca,'ytick',-0.15:0.1:0.25);
```

```
fontstyle('times new roman');

subplot(325);
plot(t2,v3-v3(1),'b-');hold on;plot(t2,v4-v4(1),'r-');
xlabel({'Time [s]','(e)'});
ylabel('Amplitude [v]');
axis([0 3.5e-3 -2.5 2.5]);
set(gca,'xtick',0:0.5*1e-3:3.5*1e-3);
set(gca,'ytick',-2.5:1.0:2.5);
legend('Accelerometer 1','Accelerometer 2','location','best');
legend('boxoff');
fontstyle('times new roman');

subplot(326);
plot(t2,v3-v3(1),'b-');hold on;plot(t2,v4-v4(1),'r-');
xlabel({'Time [s]','(f)'});
ylabel('Amplitude [v]');
set(gca,'xtick',2.5*1e-4:0.5*1e-4:6.01*1e-4);
axis([2.5e-4 6.01e-4 -0.15 0.25]);
set(gca,'ytick',-0.15:0.1:0.25);
fontstyle('times new roman');

set(gcf, 'PaperPositionMode', 'manual');
set(gcf, 'PaperUnits', 'inches');
set(gcf, 'PaperPosition', [1 1 6.5 6.5]);
print(figure(1), '-r600', '-dtiff', 'P-wave test with&without crosstalk3.tiff');
```

```
%% Time-force function of impact used in COMSOL
clear all
```

```
close all
clc

t=csvread('Impact Force.csv',8,0,[8,0,1007,0]);
F=csvread('Impact Force.csv',8,1,[8,1,1007,1]);

figure(1)
plot(t*1e6,-F,'b');
xlabel('Time [\mus]');
ylabel('Force [N]');
axis([0 50 0 300]);
fontstyle('times new roman');

set(gcf, 'PaperPositionMode', 'manual');
set(gcf, 'PaperUnits', 'inches');
set(gcf, 'PaperPosition', [1 1 4 3]);
print(figure(1), '-r600', '-dtiff', 'COMSOL_Force-Time.tiff');
```

```
%% Effect of parabolic reflector on measurements (with reflector vs. without
reflector)
clear all
close all
clc

% Global Definition
Fs=1e6/1;
N=2048;
dt=1/Fs;
t=0:dt:(N)*dt;
```

```
i=sqrt(-1);
df=10;
f_min=0e3;
f_max=40e3;
f=f_min:df:f_max;

% Time domain
% without acoustic reflector
t_wo=csvread('1us_2048us_2mmx2mm_0.1m_02252015_withoutreflector_
FocalPoint@0.15m_RimAngle90_TimeDomain.csv',8,0,[8,0,2056,0]);
y_wo=csvread('1us_2048us_2mmx2mm_0.1m_02252015_withoutreflector
_FocalPoint@0.15m_RimAngle90_TimeDomain.csv',8,1,[8,1,2056,1]);

% with acoustic reflector of rim angle=90 and focal point@0.15m(6cm offset
from impact point)
t_wi1=csvread('1us_2048us_2mmx2mm_0.1m_02252015_withreflector_Fo
calPoint@0.15m_RimAngle90_TimeDomain.csv',8,0,[8,0,2056,0]);
y_wi1=csvread('1us_2048us_2mmx2mm_0.1m_02252015_withreflector_F
ocalPoint@0.15m_RimAngle90_TimeDomain.csv',8,1,[8,1,2056,1]);

for j=1:length(f)
   freq=f(j);
   Yy_wo=y_wo'.*exp(-i*2*pi*freq*t);
   TRPy_wo(j)=trapz(t,Yy_wo);
   Yy_wi1=y_wi1'.*exp(-i*2*pi*freq*t);
   TRPy_wi1(j)=trapz(t,Yy_wi1);
end;

figure(1)
```

```
subplot(211);
plot(t_wo,y_wo,'b-');hold on;...
   plot(t_wi1,y_wi1,'r-');
xlabel({'Time [\mus]','(a)'});
ylabel('Amplitude [Pa]');
axis([0 2048 -0.5 0.5]);
set(gca,'xtick',0:512:2048);
legend('without parabolic reflector','with parabolic reflector',...
   'location','best');
legend('boxoff');
fontstyle('times new roman');

subplot(212);
plot(f/1e3,(abs(TRPy_wo)),'b-');hold on;...
   plot(f/1e3,(abs(TRPy_wi1)),'r-');
xlabel({'Frequency [kHz]','(b)'});
ylabel('Amplitude Spectrum');
axis([0 40 0 1.25e-4]);
set(gca,'ytick',0:0.25e-4:1.25e-4,'yticklabel',{"","","","",""});
legend(sprintf('without parabolic\nreflector'),sprintf('with
parabolic\nreflector'),'location','best');
legend('boxoff');
text(8,0.3e-4,'19.96kHz');
text(18.5,1.0e-4,'20.25kHz');
fontstyle('times new roman');

set(gcf, 'PaperPositionMode', 'manual');
set(gcf, 'PaperUnits', 'inches');
set(gcf, 'PaperPosition', [1 1 4 4]);
```

```
print(figure(1), '-r600', '-dtiff', 'WithoutReflector vs WithReflector.tiff');
```

```
%% Effect of parabolic reflector geometry
clear all
close all
clc

% Global Definition
Fs=1e6/1;
N=2048;
dt=1/Fs;
t=0:dt:(N)*dt;
i=sqrt(-1);
df=50;
f_min=0e3;
f_max=40e3;
f=f_min:df:f_max;

% Rim angle at 60
t_60=csvread('1us_2048us_2mmx2mm_0.1m_02252015_FocalPoint@0.11
m_RimAngle60_TimeDomain.csv',8,0,[8,0,2056,0]);
y_60=csvread('1us_2048us_2mmx2mm_0.1m_02252015_FocalPoint@0.11
m_RimAngle60_TimeDomain.csv',8,1,[8,1,2056,1]);
% Rim angle at 90
t_90=csvread('1us_2048us_2mmx2mm_0.1m_09192014_FocalPoint_Rim
Angle90_TimeDomain.csv',8,0,[8,0,2056,0]);
y_90=csvread('1us_2048us_2mmx2mm_0.1m_09192014_FocalPoint_Rim
Angle90_TimeDomain.csv',8,1,[8,1,2056,1]);
% Rim angle at 120
```

```
t_120=csvread('1us_2048us_2mmx2mm_0.1m_09192014_FocalPoint_Rim
Angle120_TimeDomain.csv',8,0,[8,0,2056,0]);
y_120=csvread('1us_2048us_2mmx2mm_0.1m_09192014_FocalPoint_Ri
mAngle120_TimeDomain.csv',8,1,[8,1,2056,1]);
% Rim angle at 150
t_150=csvread('1us_2048us_2mmx2mm_0.1m_09192014_FocalPoint_Rim
Angle150_TimeDomain.csv',8,0,[8,0,2056,0]);
y_150=csvread('1us_2048us_2mmx2mm_0.1m_09192014_FocalPoint_Ri
mAngle150_TimeDomain.csv',8,1,[8,1,2056,1]);

for j=1:length(f)
    freq=f(j);
    Y_y60=y_60'.*exp(-i*2*pi*freq*t);
    TRP_y60(j)=trapz(t,Y_y60);
    Y_y90=y_90'.*exp(-i*2*pi*freq*t);
    TRP_y90(j)=trapz(t,Y_y90);
    Y_y120=y_120'.*exp(-i*2*pi*freq*t);
    TRP_y120(j)=trapz(t,Y_y120);
    Y_y150=y_150'.*exp(-i*2*pi*freq*t);
    TRP_y150(j)=trapz(t,Y_y150);
end;

figure(1)
plot(t_60,(y_60)+1,'b');hold on;plot(t_90,(y_90)+2,'r');hold on;...
    plot(t_120,(y_120)+3,'k');hold on;plot(t_150,(y_150)+4,'c');hold on;...
    plot([100,115,115,100],[4.7,4.7,4.8,4.8],'k');hold on;...
    plot([130,115,115,130],[4.7,4.7,4.8,4.8],'k');
xlabel({'Time [\mus]','(a)'});
ylabel('Amplitude [Pa]');
```

```
axis([0 2048 0 5]);
set(gca,'xtick',0:512:2048);
set(gca,'ytick',0:1:5);
set(gca,'yticklabel',{'','','','','',''});
text(50,1.4,'Rim angle=60^o');
text(50,2.5,'Rim angle=90^o');
text(50,3.5,'Rim angle=120^o');
text(50,4.4,'Rim angle=150^o');
text(150,4.75,'0.1 Pa');
fontstyle('times new roman');
set(gcf, 'PaperPositionMode', 'manual');
set(gcf, 'PaperUnits', 'inches');
set(gcf, 'PaperPosition', [1 1 4 3]);
print(figure(1), '-r600', '-dtiff', 'DifferentGeometry_TimeDomain.tiff');

figure(2)
plot(f/1000,(abs(TRP_y60)),'b');hold on;...
   plot(f/1000,(abs(TRP_y90))+2e-4,'r');hold on;...
   plot(f/1000,(abs(TRP_y120))+4e-4,'k');hold on;...
   plot(f/1000,(abs(TRP_y150))+6e-4,'c');
xlabel({'Frequency [kHz]','(b)'});
ylabel('Amplitude Spectrum');
axis([0 40 0 8e-4]);
text(1,1e-4,'Rim angle=60^o');
text(1,3e-4,'Rim angle=90^o');
text(1,5e-4,'Rim angle=120^o');
text(1,7e-4,'Rim angle=150^o');
text(17,1.2e-4,'19.25kHz');
```

```
text(18,3.8e-4,'20.15kHz');
text(18.5,5.3e-4,'20.55kHz');
text(18.25,7.2e-4,'20.25kHz');
set(gca,'ytick',0:2e-4:8e-4);
set(gca,'yticklabel',{",",",",","});
fontstyle('times new roman');
set(gcf, 'PaperPositionMode', 'manual');
set(gcf, 'PaperUnits', 'inches');
set(gcf, 'PaperPosition', [1 1 4 3]);
print(figure(2), '-r600', '-dtiff', 'DifferentGeometry_FrequencyDomain.tiff');
```

```
%% Effect of reflector focus height
clear all
close all
clc

% Global Definition
Fs=1e6/1;
N=8192;
dt=1/Fs;
t=0:dt:(N)*dt;
i=sqrt(-1);
df=50;
f_min=0e3;
f_max=40e3;
f=f_min:df:f_max;

% Focal Point 1(0,0.15)
```

```
t_fp1=csvread('1us_8192us_2mmx2mm_0.1m_09012014_FocalPoint_1_TimeDomain.csv',8,0,[8,0,8200,0]);
y_fp1=csvread('1us_8192us_2mmx2mm_0.1m_09012014_FocalPoint_1_TimeDomain.csv',8,1,[8,1,8200,1]);
% Focal Point 2(0,0.20)
t_fp2=csvread('1us_8192us_2mmx2mm_0.1m_09012014_FocalPoint_2_TimeDomain.csv',8,0,[8,0,8200,0]);
y_fp2=csvread('1us_8192us_2mmx2mm_0.1m_09012014_FocalPoint_2_TimeDomain.csv',8,1,[8,1,8200,1]);
% Focal Point 3(0,0.25)
t_fp3=csvread('1us_8192us_2mmx2mm_0.1m_09012014_FocalPoint_3_TimeDomain.csv',8,0,[8,0,8200,0]);
y_fp3=csvread('1us_8192us_2mmx2mm_0.1m_09012014_FocalPoint_3_TimeDomain.csv',8,1,[8,1,8200,1]);
% Focal Point 4(0,0.30)
t_fp4=csvread('1us_8192us_2mmx2mm_0.1m_09012014_FocalPoint_4_TimeDomain.csv',8,0,[8,0,8200,0]);
y_fp4=csvread('1us_8192us_2mmx2mm_0.1m_09012014_FocalPoint_4_TimeDomain.csv',8,1,[8,1,8200,1]);
% Focal Point 5(0,0.35)
t_fp5=csvread('1us_8192us_2mmx2mm_0.1m_09012014_FocalPoint_5_TimeDomain.csv',8,0,[8,0,8200,0]);
y_fp5=csvread('1us_8192us_2mmx2mm_0.1m_09012014_FocalPoint_5_TimeDomain.csv',8,1,[8,1,8200,1]);

for j=1:length(f)
    freq=f(j);
    Y_fp1=y_fp1'.*exp(-i*2*pi*freq*t);
    TRP_fp1(j)=trapz(t,Y_fp1);
```

```
    Y_fp2=y_fp2'.*exp(-i*2*pi*freq*t);
    TRP_fp2(j)=trapz(t,Y_fp2);
    Y_fp3=y_fp3'.*exp(-i*2*pi*freq*t);
    TRP_fp3(j)=trapz(t,Y_fp3);
    Y_fp4=y_fp4'.*exp(-i*2*pi*freq*t);
    TRP_fp4(j)=trapz(t,Y_fp4);
    Y_fp5=y_fp5'.*exp(-i*2*pi*freq*t);
    TRP_fp5(j)=trapz(t,Y_fp5);
end;

figure(1)
plot(t_fp1,(y_fp1)+0.8,'b');hold on;plot(t_fp2,(y_fp2)+1.6,'r');hold on;...
    plot(t_fp3,(y_fp3)+2.4,'k');hold on;plot(t_fp4,(y_fp4)+3.2,'c');hold on;...
    plot(t_fp5,(y_fp5)+4.0,'g');hold on;...
    plot([300,350,350,300],[4.5,4.5,4.6,4.6],'k');hold on;...
    plot([400,350,350,400],[4.5,4.5,4.6,4.6],'k');
xlabel({'Time [\mus]','(a)'});
ylabel('Amplitude [Pa]');
text(5800,1.1,'Height=0.05m');
text(5800,1.8,'Height=0.1m');
text(5800,2.6,'Height=0.15m');
text(5800,3.4,'Height=0.2m');
text(5800,4.2,'Height=0.25m');
text(500,4.55,'0.1 Pa');
axis([0 8192 0 4.8]);
set(gca,'xtick',0:2048:8192);
set(gca,'ytick',0:0.8:4.8);
set(gca,'yticklabel',{",",",",",",",","});
fontstyle('times new roman');
```

```
set(gcf, 'PaperPositionMode', 'manual');
set(gcf, 'PaperUnits', 'inches');
set(gcf, 'PaperPosition', [1 1 4 3]);
print(figure(1), '-r600', '-dtiff', 'Parabolic Reflecor with rim
angle=90@different height_TimeDomain.tiff');

figure(2)
plot(f/1000,(abs(TRP_fp1))+0,'b');hold on;plot(f/1000,(abs(TRP_fp2))+2.5e-
4,'r');hold on;...
   plot(f/1000,(abs(TRP_fp3))+5e-4,'k');hold
on;plot(f/1000,(abs(TRP_fp4))+7.5e-4,'c');hold on;...
   plot(f/1000,(abs(TRP_fp5))+10e-4,'g');
xlabel({'Frequency [kHz]','(b)'});
ylabel('Amplitude Spectrum');
text(29,1e-4,'Height=0.05m');
text(29,3.5e-4,'Height=0.1m');
text(29,6e-4,'Height=0.15m');
text(29,8.5e-4,'Height=0.2m');
text(29,11e-4,'Height=0.25m');
text(18.25,2.25e-4,'20.7kHz');
text(18,4e-4,'20.15kHz');
text(18,6.4e-4,'20.15kHz');
text(18,8.9e-4,'20.15kHz');
text(18,11.4e-4,'20.15kHz');
axis([0 40 0 1.25e-3]);
set(gca,'ytick',0:2.5e-4:1.25e-3);
set(gca,'yticklabel',{",",",",",",","});
fontstyle('times new roman');
set(gcf, 'PaperPositionMode', 'manual');
```

```
set(gcf, 'PaperUnits', 'inches');
set(gcf, 'PaperPosition', [1 1 4 3]);
print(figure(2), '-r600', '-dtiff', 'Parabolic Reflecor with rim
angle=90@different height_FrequencyDomain.tiff');
```

```
%% P-wave speed measurement test performed on defect-free concrete
plate
clear all
close all
clc

% Global Definition
Fs=1e6/3;
dt=1/Fs;
N=1024;
T=N/Fs;
t=0:dt:(N-1)*dt;

% Fs=333kHz, 3 channels
v1=xlsread('P_wave_333k3ch_1024.xlsx','sheet1','A2:A1025');
v2=xlsread('P_wave_333k3ch_1024.xlsx','sheet1','C2:C1025');

figure(1)
subplot(211);
plot(t,v1-v1(1),'b.-');hold on;...
    plot(t1,v2-v2(1),'r.-');
xlabel({'Time [s]','(a)'});
ylabel('Amplitude [v]');
axis([0 3.5e-3 -2.5 2.5]);
```

```
set(gca,'xtick',0:0.5*1e-3:3.5*1e-3);
set(gca,'ytick',-2.5:1.0:2.5);
legend('Accelerometer 1','Accelerometer 2','location','best');
legend('boxoff');
fontstyle('times new roman');

subplot(212);
plot(t,v1-v1(1),'b.-');hold on;...
    plot(t,v2-v2(1),'r.-');
xlabel({'Time [s]','(b)'});
ylabel('Amplitude [v]');
set(gca,'xtick',2.5*1e-4:0.5*1e-4:6.01*1e-4);
axis([2.5e-4 6.01e-4 -0.15 0.25]);
set(gca,'ytick',-0.15:0.1:0.25);
legend('Accelerometer 1','Accelerometer 2','location','best');
legend('boxoff');
fontstyle('times new roman');

set(gcf, 'PaperPositionMode', 'manual');
set(gcf, 'PaperUnits', 'inches');
set(gcf, 'PaperPosition', [1 1 4 3.5]);
print(figure(1), '-r600', '-dtiff', 'P-wave test on solid concrete1.tiff');
```

```
%% Physsially coupled impact-echo test performed on defect-free concrete
plate
clear all
close all
clc
```

```
v1=xlsread('IE_test_Acc_500k_2048.xlsx','sheet1','A2:A2049');

%Global difinition
Fs=1e6/2;
N=2048;
dt=1/Fs;
t=0:dt:(N-1)*dt;
i=sqrt(-1);
df=1;
f_min=0e3;
f_max=Fs/2;
f=f_min:df:f_max;

for j=1:length(f)
    freq=f(j);
    Yv1=v1'.*exp(-i*2*pi*freq*t);
    TRPv1(j)=trapz(t,Yv1);
end;

figure(1)
subplot(211);
plot(t,v1,'b');
xlabel({'Time [s]','(a)'});
ylabel('Amplitude [v]');
% axis([-0.1e-3 2.3e-3 -2 2]);
fontstyle('times new roman');

subplot(212);
plot(f/1e3,(abs(TRPv1)/max(abs(TRPv1))).^2,'b');
```

```
xlabel({'Frequency [kHz]','(b)'});
ylabel({'Normalized','Amplitude Spectrum'});
axis([0 f_max/1e3 -0.005 1.5]);
text(13,1.1,'14.2kHz');
fontstyle('times new roman');

set(gcf, 'PaperPositionMode', 'manual');
set(gcf, 'PaperUnits', 'inches');
set(gcf, 'PaperPosition', [1 1 4 3.5]);
print(figure(1), '-r600', '-dtiff',
'IE_test_Acc_Frequency_500kHz@4096us.tiff');
```

```
%% Test results for air-coupled, impact-echo test performed on defect-free
concrete plate
...(Microphone vs. Microphone+sound isolation foam
vs.Microphone+prabolic reflector vs. Microphone+parabolic reflector+foam)
clear all
close all
clc

% Global Definition
Fs=1e6/2;
N=2048;
dt=1/Fs;
t=0:dt:(N-1)*dt;
i=sqrt(-1);
df=50;
f_min=0e3;
f_max=80e3;
```

```
f=f_min:df:f_max;

v1=xlsread('IE_test_Mic_beforepassivefilter.xlsx','sheet1','A2:A2049'); %
Microphone only
v2=xlsread('IE_test_Mic_500k_2048.xlsx','sheet1','A2:A2049'); %
Microphone+sound isolation
v3=xlsread('IE_test_Mic+reflector_beforepassivefilter.xlsx','sheet1','A2:A204
9'); % Microphone+parabolic reflector
v4=xlsread('IE_test_Mic+reflector+foam_beforepassivefilter.xlsx','sheet1','A2
:A2049'); % Microphone+parabolic reflector+foam

for j=1:length(f)
    freq=f(j);
    Yv1=v1'.*exp(-i*2*pi*freq*t);
    TRPv1(j)=trapz(t,Yv1);
    Yv2=v2'.*exp(-i*2*pi*freq*t);
    TRPv2(j)=trapz(t,Yv2);
    Yv3=v3'.*exp(-i*2*pi*freq*t);
    TRPv3(j)=trapz(t,Yv3);
    Yv4=v4'.*exp(-i*2*pi*freq*t);
    TRPv4(j)=trapz(t,Yv4);
end;

figure(1)
plot(t,v1+0.1,'b');hold on;...
    plot(t,v2+0.2,'r');hold on;...
    plot(t,v3+0.3,'k');hold on;...
    plot(t,v4+0.4,'c');
xlabel({'Time [s]','(a)'});
```

```
ylabel('Amplitude [v]');
axis([0 4.5e-3 0.05 0.5]);
set(gca,'xtick',0:1.5e-3:4.5e-3);
set(gca,'ytick',0.05:0.05:0.5);
set(gca,'yticklabel',{'','','','','','','','','',''});
text(2.2e-3,0.13,'Microphone only');
text(2.2e-3,0.25,{'Microphone with sound','isolation enclosure'});
text(2.2e-3,0.35,{'Microphone with','parabolic reflector'});
text(2.2e-3,0.45,{'Microphone with parabolic','reflector and foam'});
fontstyle('times new roman');
set(gcf, 'PaperPositionMode', 'manual');
set(gcf, 'PaperUnits', 'inches');
set(gcf, 'PaperPosition', [1 1 4 3.5]);
print(figure(1), '-r600', '-dtiff',
'IE_test_Mic_4DifferentMethod_Time@500kHz.tiff');

figure(2)
plot(f/1e3,(abs(TRPv1)).^2,'b');hold on;...
   plot(f/1e3,(abs(TRPv2)).^2+1.2e-10,'r');hold on;...
   plot(f/1e3,(abs(TRPv3)).^2+2.4e-10,'k');hold on;...
   plot(f/1e3,(abs(TRPv4)).^2+3.6e-10,'c');
xlabel({'Frequency [kHz]','(b)'});
ylabel('Spectrum Amplitude');
axis([0 40 0 4.8e-10]);
set(gca,'ytick',0:1.2e-4:4.8e-4);
set(gca,'yticklabel',{'','','','',''});
text(12,0.5e-10,'13.6kHz');
text(12,1.6e-10,'13.5kHz');
text(5,3.3e-10,'13.9kHz');
```

```
text(13,4.3e-10,'14kHz');
text(22,0.3e-10,'Microphone only');
text(22,1.6e-10,{'Microphone with sound','isolation enclosure'});
text(22,3e-10,{'Microphone with','parabolic reflector'});
text(20,4.1e-10,{'Microphone with parabolic','reflector and foam'});
fontstyle('times new roman');

set(gcf, 'PaperPositionMode', 'manual');
set(gcf, 'PaperUnits', 'inches');
set(gcf, 'PaperPosition', [1 1 4 3.5]);
print(figure(2), '-r600', '-dtiff',
'IE_test_Mic_4DifferentMethod_Frequency@500kHz.tiff');
```

```
%% Test results for physical-coupled and air-coupled, impact-echo tests
performed on a defect-free concrete plate
...(Microphone vs. Microphone+sound isolation foam vs.
Microphone+prabolic reflector vs. Microphone+parabolic reflector+foam)
clear all
close all
clc

% Global Definition
Fs=1e6/2;
N=2048;
dt=1/Fs;
t=0:dt:(N-1)*dt;
i=sqrt(-1);
df=50;
f_min=0e3;
```

```
f_max=20e3;
f=f_min:df:f_max;

% Physically coupled method
v1=xlsread('IE_test_Acc_500k_2048.xlsx','sheet1','A2:A2049'); %
Accelerometer
% Air-coupled method
v2=xlsread('IE_test_Mic_beforepassivefilter.xlsx','sheet1','A2:A2049'); %
Microphone only
v3=xlsread('IE_test_Mic_500k_2048.xlsx','sheet1','A2:A2049'); %
Microphone+sound isolation
v4=xlsread('IE_test_Mic+reflector_beforepassivefilter.xlsx','sheet1','A2:A204
9'); % Microphone+parabolic reflector
v5=xlsread('IE_test_Mic+reflector+foam_beforepassivefilter.xlsx','sheet1','A2
:A2049'); % Microphone+parabolic reflector+foam

for j=1:length(f)
    freq=f(j);
    Yv1=v1'.*exp(-i*2*pi*freq*t);
    TRPv1(j)=trapz(t,Yv1);
    Yv2=v2'.*exp(-i*2*pi*freq*t);
    TRPv2(j)=trapz(t,Yv2);
    Yv3=v3'.*exp(-i*2*pi*freq*t);
    TRPv3(j)=trapz(t,Yv3);
    Yv4=v4'.*exp(-i*2*pi*freq*t);
    TRPv4(j)=trapz(t,Yv4);
    Yv5=v5'.*exp(-i*2*pi*freq*t);
    TRPv5(j)=trapz(t,Yv5);
end;
```

```
figure(1)
plot(t,v1/max(v1)+3,'b');hold on;...
    plot(t,v2/max(v2)+6,'r');hold on;...
    plot(t,v3/max(v3)+9,'k');hold on;...
    plot(t,v4/max(v4)+12,'c');hold on;...
    plot(t,v5/max(v5)+15,'g');
xlabel({'Time [s]','(a)'});
ylabel('Normalized Amplitude');
axis([0 4.5e-3 0 18]);
set(gca,'xtick',0:1.5e-3:4.5e-3);
set(gca,'ytick',0:3:18);
set(gca,'yticklabel',{"","","","","",""});
text(0.75e-3,3.7,'Accelerometer');
text(0.75e-3,6.9,'Microphone only');
text(0.75e-3,10.6,'Microphone with sound isolation enclosure');
text(0.75e-3,13.3,'Microphone with parabolic reflector');
text(0.75e-3,16.6,'Microphone with parabolic reflector and foam');
fontstyle('times new roman');

set(gcf, 'PaperPositionMode', 'manual');
set(gcf, 'PaperUnits', 'inches');
set(gcf, 'PaperPosition', [1 1 4 3.5]);
print(figure(1), '-r600', '-dtiff', 'IE_test_Mic_physical coupled vs air-
coupled_Time@500kHz.tiff');

figure(2)
a=abs(TRPv2);
b=a(:,50:end);
```

```
[A,B]=max(b);
plot(f/1e3,(abs(TRPv1)/max(abs(TRPv1))).^2,'b');hold on;...
    plot(f/1e3,(abs(TRPv2)/A).^2+2,'r');hold on;...
    plot(f/1e3,(abs(TRPv3)/max(abs(TRPv3))).^2+4,'k');hold on;...
    plot(f/1e3,(abs(TRPv4)/max(abs(TRPv4))).^2+6,'c');hold on;...
    plot(f/1e3,(abs(TRPv5)/max(abs(TRPv5))).^2+8,'g');
xlabel({'Frequency [kHz]','(b)'});
ylabel('Normalized Spectrum Amplitude');
axis([0 20 0 10]);
set(gca,'ytick',0:2:10);
set(gca,'yticklabel',{"","","","","",""});
text(13,1.3,'14.2kHz');
text(12.5,3.5,'13.6kHz');
text(12.5,5.4,'13.5kHz');
text(13,7.5,'13.9kHz');
text(13,9.5,'14.0kHz');
text(2,0.5,'Accelerometer');
text(2,2.8,'Microphone only');
text(2,4.8,{'Microphone with sound','isolation enclosure'});
text(2,6.8,{'Microphone with','parabolic reflector'});
text(2,8.9,{'Microphone with parabolic','reflector and foam'});
fontstyle('times new roman');

set(gcf, 'PaperPositionMode', 'manual');
set(gcf, 'PaperUnits', 'inches');
set(gcf, 'PaperPosition', [1 1 4 3.5]);
print(figure(2), '-r600', '-dtiff', 'IE_test_Mic_physical coupled vs air-
coupled_Frequency@500kHz.tiff');
```

```
%% Test results of P-wave speed measurement test performed on a concrete
plate with artificial defects
clear all
close all
clc

% Global Definition
Fs=1e6/3;
N=1024;
dt=1/Fs;
t=0:dt:(N-1)*dt;

v1=xlsread('P_wave_333k3ch_1024_3rd.xlsx','sheet1','A2:A1025');
v2=xlsread('P_wave_333k3ch_1024_3rd.xlsx','sheet1','C2:C1025');

figure(1)
subplot(211);
plot(t,v1-e,'b.-');hold on;...
    plot(t,v2-f,'r.-');
xlabel({'Time[s]','(a)'});
ylabel('Amplitude [v]');
legend('Accelerometer 1','Accelerometer 2','location','best');
fontstyle('times new roman');

subplot(212);
plot(t,v1-e,'b.-');hold on;...
    plot(t,v2-f,'r.-');
xlabel({'Time[s]','(b)'});
ylabel('Amplitude [v]');
```

```
axis ([2.5e-4 5.0e-4 -0.05 0.05]);
legend('Accelerometer 1','Accelerometer 2','location','best');
fontstyle('times new roman');

set(gcf, 'PaperPositionMode', 'manual');
set(gcf, 'PaperUnits', 'inches');
set(gcf, 'PaperPosition', [1 1 4 3.5 ]);
print(figure(1), '-r600', '-dtiff', 'P-wave
test_ConcretewithArtificialDefects.tiff');
```

```
%% Test results for the impact-echo test for concrete plate with artificial
defects by physically coupled and air-coupled methods
% IE test on solid
clear all
close all
clc

% Global Definition
Fs=1e6/2;
N=2048;
dt=1/Fs;
t=0:dt:(N-1)*dt;
i=sqrt(-1);
f_Acc_max=Fs/2;
f_Mic_max=Fs/2;
df=25;
f_Acc=0:df:f_Acc_max;
f_Mic=0:df:f_Mic_max;
```

```
% Acc
v1=xlsread('IE_test_Acc_solid_2nd.xlsx','sheet1','A2:A2049');
% Mic
v2=xlsread('IE_test_Mic_solid_1st.xlsx','sheet1','A2:A2049');

for j=1:length(f_Acc)
    freq_Acc=f_Acc(j);
    Yv1=v1'.*exp(-i*2*pi*freq_Acc*t);
    TRPv1(j)=trapz(t,Yv1);
end;
for k=1:length(f_Mic)
    freq_Mic=f_Mic(k);
    Yv2=v2'.*exp(-i*2*pi*freq_Mic*t);
    TRPv2(k)=trapz(t,Yv2);
end;

figure(1)
subplot(211);
plot(t,v1,'b');
xlabel('Time [s]');
ylabel('Amplitude [v]');
axis([0 5e-3 -1.5 1.5]);
set(gca,'ytick',-1.5:1:1.5);
legend('Accelerometer');
fontstyle('times new roman');

subplot(212);
plot(f_Acc/1e3,(abs(TRPv1)/max(abs(TRPv1))).^2,'b');
xlabel({'Frequency [kHz]','(a)'});
```

```
ylabel({'Normalized','Spectrum Amplitude'});
axis([0 40 0 1.5]);
text(9,1.1,'10kHz');
legend('Accelerometer','location','best');
fontstyle('times new roman');

set(gcf, 'PaperPositionMode', 'manual');
set(gcf, 'PaperUnits', 'inches');
set(gcf, 'PaperPosition', [1 1 4 3.5]);
print(figure(1), '-r600', '-dtiff', 'IE_test_PhysicalCoupled vs
AirCoupled_Solid1.tiff');

figure(2)
subplot(211);
plot(t,v2,'b');
xlabel('Time [s]');
ylabel('Amplitude [v]');
axis([0 5e-3 -0.02 0.02]);
legend('Microphone','location','best');
fontstyle('times new roman');

subplot(212);
plot(f_Mic/1e3,(abs(TRPv2)/max(abs(TRPv2))).^2,'b');
xlabel({'Frequency [kHz]','(b)'});
ylabel({'Normalized','Spectrum Amplitude'});
axis([0 40 0 1.5]);
text(9,1.1,'9.9kHz');
legend('Microphone','location','best');
fontstyle('times new roman');
```

```
set(gcf, 'PaperPositionMode', 'manual');
set(gcf, 'PaperUnits', 'inches');
set(gcf, 'PaperPosition', [1 1 4 3.5]);
print(figure(2), '-r600', '-dtiff', 'IE_test_PhysicalCoupled vs
AirCoupled_Solid2.tiff');

%% IE test on 4x4shallow
clear all
close all
clc

% Global Definition
Fs=1e6/2;
N=2048;
dt=1/Fs;
t=0:dt:(N-1)*dt;
i=sqrt(-1);
f_Acc_max=Fs/2;
f_Mic_max=Fs/2;
df=25;
f_Acc=0:df:f_Acc_max;
f_Mic=0:df:f_Mic_max;

% Acc_4x4 shallow delamination
v1=xlsread('IE_test_Acc_290060_4x4shallow.xlsx','sheet1','A2:A2049');
% Mic_4x4 shallow delamination
v2=xlsread('IE_test_Mic_290060_4x4shallow.xlsx','sheet1','A2:A2049');
```

```
for j=1:length(f_Acc)
    freq_Acc=f_Acc(j);
    Yv1=v1'.*exp(-i*2*pi*freq_Acc*t);
    TRPv1(j)=trapz(t,Yv1);
end;
for k=1:length(f_Mic)
    freq_Mic=f_Mic(k);
    Yv2=v2'.*exp(-i*2*pi*freq_Mic*t);
    TRPv2(k)=trapz(t,Yv2);
end;

figure(1)
subplot(211);
plot(t,v1,'b');
xlabel('Time [s]');
ylabel('Amplitude [v]');
set(gca,'ytick',-3:2:3);
axis([0 5e-3 -3 3]);
legend('Accelerometer');
fontstyle('times new roman');

subplot(212);
plot(f_Acc/1e3,(abs(TRPv1)/max(abs(TRPv1))).^2,'b');
xlabel({'Frequency [kHz]','(a)'});
ylabel({'Normalized','Spectrum Amplitude'});
axis([0 40 0 1.5]);
text(7,1.1,'7.875kHz');
legend('Accelerometer','location','best');
fontstyle('times new roman');
```

```
set(gcf, 'PaperPositionMode', 'manual');
set(gcf, 'PaperUnits', 'inches');
set(gcf, 'PaperPosition', [1 1 4 3.5]);
print(figure(1), '-r600', '-dtiff', 'IE_test_PhysicalCoupled vs
AirCoupled_4x4shallow1.tiff');

figure(2)
subplot(211);
plot(t,v2,'b');
xlabel('Time [s]');
ylabel('Amplitude [v]');
axis([0 5e-3 -0.02 0.02]);
set(gca,'ytick',-0.02:0.01:0.02);
legend('Microphone','location','best');
fontstyle('times new roman');

subplot(212);
plot(f_Mic/1e3,(abs(TRPv2)/max(abs(TRPv2))).^2,'b');
xlabel({'Frequency [kHz]','(b)'});
ylabel({'Normalized','Spectrum Amplitude'});
axis([0 40 0 1.5]);
text(7,1.1,'7.875kHz');
text(22,0.25,'23.15kHz');
legend('Microphone','location','best');
fontstyle('times new roman');

set(gcf, 'PaperPositionMode', 'manual');
set(gcf, 'PaperUnits', 'inches');
```

```
set(gcf, 'PaperPosition', [1 1 4 3.5]);
print(figure(2), '-r600', '-dtiff', 'IE_test_PhysicalCoupled vs
AirCoupled_4x4shallow2.tiff');

%% IE test on 8x8shallow
clear all
close all
clc

% Global Definition
Fs=1e6/2;
N=2048;
dt=1/Fs;
t=0:dt:(N-1)*dt;
i=sqrt(-1);
f_Acc_max=Fs/2;
f_Mic_max=Fs/2;
df=25;
f_Acc=0:df:f_Acc_max;
f_Mic=0:df:f_Mic_max;

% Acc_8x8 shallow delamination
v1=xlsread('IE_test_Acc_220060_8x8shallow.xlsx','sheet1','A2:A2049');
% Mic_8x8 shallow delamination
v2=xlsread('IE_test_Mic_220060_8x8shallow.xlsx','sheet1','A2:A2049');

for j=1:length(f_Acc)
    freq_Acc=f_Acc(j);
    Yv1=v1'.*exp(-i*2*pi*freq_Acc*t);
```

```
    TRPv1(j)=trapz(t,Yv1);
end;
for k=1:length(f_Mic)
    freq_Mic=f_Mic(k);
    Yv2=v2'.*exp(-i*2*pi*freq_Mic*t);
    TRPv2(k)=trapz(t,Yv2);
end;

figure(1)
subplot(211);
plot(t,v1,'b');
xlabel('Time [s]');
ylabel('Amplitude [v]');
axis([0 5e-3 -3 3]);
set(gca,'ytick',-3:2:3);
legend('Accelerometer');
fontstyle('times new roman');

subplot(212);
plot(f_Acc/1e3,(abs(TRPv1)/max(abs(TRPv1))).^2,'b');
xlabel({'Frequency [kHz]','(a)'});
ylabel({'Normalized','Spectrum Amplitude'});
axis([0 40 0 1.5]);
text(3.5,1.1,'4.325kHz');
text(6,0.74,'6.925kHz');
legend('Accelerometer','location','best');
fontstyle('times new roman');

set(gcf, 'PaperPositionMode', 'manual');
```

```
set(gcf, 'PaperUnits', 'inches');
set(gcf, 'PaperPosition', [1 1 4 3.5]);
print(figure(1), '-r600', '-dtiff', 'IE_test_PhysicalCoupled vs
AirCoupled_8x8shallow1.tiff');

figure(2)
subplot(211);
plot(t,v2,'b');
xlabel('Time [s]');
ylabel('Amplitude [v]');
axis([0 5e-3 -0.02 0.02]);
set(gca,'ytick',-0.02:0.01:0.02);
legend('Microphone','location','best');
fontstyle('times new roman');

subplot(212);
plot(f_Mic/1e3,(abs(TRPv2)/max(abs(TRPv2))).^2,'b');
xlabel({'Frequency [kHz]','(b)'});
ylabel({'Normalized','Spectrum Amplitude'});
axis([0 40 0 1.5]);
text(2.3,1.1,'3.325kHz');
text(5.5,0.7,'6.525kHz');
text(22.4,0.8,'23.2kHz');
legend('Microphone','location','best');
fontstyle('times new roman');

set(gcf, 'PaperPositionMode', 'manual');
set(gcf, 'PaperUnits', 'inches');
set(gcf, 'PaperPosition', [1 1 4 3.5]);
```

```
print(figure(2), '-r600', '-dtiff', 'IE_test_PhysicalCoupled vs
AirCoupled_8x8shallow2.tiff');

%% IE test on 12x12shallow
clear all
close all
clc

% Global Definition
Fs=1e6/2;
N=2048;
dt=1/Fs;
t=0:dt:(N-1)*dt;
i=sqrt(-1);
f_Acc_max=Fs/2;
f_Mic_max=Fs/2;
df=25;
f_Acc=0:df:f_Acc_max;
f_Mic=0:df:f_Mic_max;

% Acc_12x12 shallow delamination
v1=xlsread('IE_test_Acc_130070_12x12shallow.xlsx','sheet1','A2:A2049');
% Mic_12x12 shallow delamination
v2=xlsread('IE_test_Mic_130070_12x12shallow1.xlsx','sheet1','A2:A2049');

for j=1:length(f_Acc)
    freq_Acc=f_Acc(j);
    Yv1=v1'.*exp(-i*2*pi*freq_Acc*t);
    TRPv1(j)=trapz(t,Yv1);
```

```
end;
for k=1:length(f_Mic)
   freq_Mic=f_Mic(k);
   Yv2=v2'.*exp(-i*2*pi*freq_Mic*t);
   TRPv2(k)=trapz(t,Yv2);
end;

figure(1)
subplot(211);
plot(t,v1,'b');
xlabel('Time [s]');
ylabel('Amplitude [v]');
axis([0 5e-3 -1 1]);
set(gca,'ytick',-1:0.5:1);
legend('Accelerometer');
fontstyle('times new roman');

subplot(212);
plot(f_Acc/1e3,(abs(TRPv1)/max(abs(TRPv1))).^2,'b');
xlabel({'Frequency [kHz]','(a)'});
ylabel({'Normalized','Spectrum Amplitude'});
axis([0 40 0 1.5]);
text(1.7,1.1,'2.7kHz');
legend('Accelerometer','location','best');
fontstyle('times new roman');

set(gcf, 'PaperPositionMode', 'manual');
set(gcf, 'PaperUnits', 'inches');
set(gcf, 'PaperPosition', [1 1 4 3.5]);
```

```
print(figure(1), '-r600', '-dtiff', 'IE_test_PhysicalCoupled vs
AirCoupled_12x12shallow1.tiff');

figure(2)
subplot(211);
plot(t,v2,'b');
xlabel('Time [s]');
ylabel('Amplitude [v]');
axis([0 5e-3 -0.03 0.03]);
set(gca,'ytick',-0.03:0.02:0.03);
legend('Microphone','location','best');
fontstyle('times new roman');

subplot(212);
plot(f_Mic/1e3,(abs(TRPv2)/max(abs(TRPv2))).^2,'b');
xlabel({'Frequency [kHz]','(b)'});
ylabel({'Normalized','Spectrum Amplitude'});
axis([0 40 0 1.5]);
text(1.8,0.93,'2.725kHz');
text(22.3,1.1,'23.15kHz');
legend('Microphone','location','northwest');
fontstyle('times new roman');

set(gcf, 'PaperPositionMode', 'manual');
set(gcf, 'PaperUnits', 'inches');
set(gcf, 'PaperPosition', [1 1 4 3.5]);
print(figure(2), '-r600', '-dtiff', 'IE_test_PhysicalCoupled vs
AirCoupled_12x12shallow2.tiff');
```

```
%% IE test on 4x4deep
clear all
close all
clc

Fs=1e6/2;
N=2048;
dt=1/Fs;
t=0:dt:(N-1)*dt;
i=sqrt(-1);
f_Acc_max=Fs/2;
f_Mic_max=Fs/2;
df=25;
f_Acc=0:df:f_Acc_max;
f_Mic=0:df:f_Mic_max;

% Acc_4x4 deep delamination
v1=xlsread('IE_test_Acc_290310_4x4deep.xlsx','sheet1','A2:A2049');
% Mic_4x4 deep delamination
v2=xlsread('IE_test_Mic_290310_4x4deep.xlsx','sheet1','A2:A2049');

for j=1:length(f_Acc)
    freq_Acc=f_Acc(j);
    Yv1=v1'.*exp(-i*2*pi*freq_Acc*t);
    TRPv1(j)=trapz(t,Yv1);
    Yv1CLP=v1CLP'.*exp(-i*2*pi*freq_Acc*t);
    TRPv1CLP(j)=trapz(t,Yv1CLP);
end;
for k=1:length(f_Mic)
```

```
    freq_Mic=f_Mic(k);
    Yv2=v2'.*exp(-i*2*pi*freq_Mic*t);
    TRPv2(k)=trapz(t,Yv2);
end;

figure(1)
subplot(211);
plot(t,v1,'b');
xlabel('Time [s]');
ylabel('Amplitude [v]');
axis([0 5e-3 -1.5 1.5]);
set(gca,'ytick',-1.5:1:1.5);
legend('Accelerometer');
fontstyle('times new roman');

subplot(212);
plot(f_Acc/1e3,(abs(TRPv1)/max(abs(TRPv1))).^2,'b');
xlabel('Frequency [kHz]');
ylabel({'Normalized','Spectrum Amplitude'});
axis([0 40 0 1.5]);
text(13.2,1.1,'14.15kHz');
legend('Accelerometer');
fontstyle('times new roman');

set(gcf, 'PaperPositionMode', 'manual');
set(gcf, 'PaperUnits', 'inches');
set(gcf, 'PaperPosition', [1 1 4 3.5]);
print(figure(1), '-r600', '-dtiff', 'IE_test_PhysicalCoupled vs
AirCoupled_4x4deep1.tiff');
```

```
figure(2)
subplot(211);
plot(t,v2,'b');
xlabel('Time [s]');
ylabel('Amplitude [v]');
axis([0 5e-3 -0.02 0.02]);
set(gca,'ytick',-0.02:0.01:0.02);
legend('Microphone','location','best');
fontstyle('times new roman');

subplot(212);
plot(f_Mic/1e3,(abs(TRPv2)/max(abs(TRPv2))).^2,'b');
xlabel({'Frequency [kHz]','(b)'});
ylabel({'Normalized','Spectrum Amplitude'});
axis([0 40 0 1.5]);
text(12.5,1.1,'13.4kHz');
legend('Microphone','location','best');
fontstyle('times new roman');

set(gcf, 'PaperPositionMode', 'manual');
set(gcf, 'PaperUnits', 'inches');
set(gcf, 'PaperPosition', [1 1 4 3.5]);
print(figure(2), '-r600', '-dtiff', 'IE_test_PhysicalCoupled vs
AirCoupled_4x4deep2.tiff');

%% IE test on 8x8deep  Acc vs. Mic
clear all
close all
```

```
clc

% Global Definition
Fs=1e6/2;
N=2048;
dt=1/Fs;
t=0:dt:(N-1)*dt;
i=sqrt(-1);
f_Acc_max=Fs/2;
f_Mic_max=Fs/2;
df=25;
f_Acc=0:df:f_Acc_max;
f_Mic=0:df:f_Mic_max;

% Acc_8x8 deep delamination
v1=xlsread('IE_test_Acc_230310_8x8deep.xlsx','sheet1','A2:A2049');
% Mic_8x8 deep delamination
v2=xlsread('IE_test_Mic_230310_8x8deep.xlsx','sheet1','A2:A2049');

for j=1:length(f_Acc)
    freq_Acc=f_Acc(j);
    Yv1=v1'.*exp(-i*2*pi*freq_Acc*t);
    TRPv1(j)=trapz(t,Yv1);
end;
for k=1:length(f_Mic)
    freq_Mic=f_Mic(k);
    Yv2=v2'.*exp(-i*2*pi*freq_Mic*t);
    TRPv2(k)=trapz(t,Yv2);
end;
```

```
% Find the maximum value of non-resonance frequency spectra for
accelerometer
a=abs(TRPv1);
b=a(:,1:1500);
[c,d]=max(b);
e=b(d-1);

figure(1)
subplot(211);
plot(t,v1,'b');
xlabel('Time [s]');
ylabel('Amplitude [v]');
axis([0 5e-3 -2 2]);
set(gca,'ytick',-2:1:2);
legend('Accelerometer');
fontstyle('times new roman');

subplot(212);
plot(f_Acc/1e3,(abs(TRPv1)/e).^2,'b');
xlabel({'Frequency [kHz]','(a)'});
ylabel({'Normalized','Spectrum Amplitude'});
axis([0 40 0 1.5]);
text(13.2,1.1,'14.18kHz');
legend('Accelerometer','location','northwest');
fontstyle('times new roman');

set(gcf, 'PaperPositionMode', 'manual');
set(gcf, 'PaperUnits', 'inches');
set(gcf, 'PaperPosition', [1 1 4 3.5]);
```

```
print(figure(1), '-r600', '-dtiff', 'IE_test_PhysicalCoupled vs
AirCoupled_8x8deepw1.tiff');

figure(2)
subplot(211);
plot(t,v2,'b');
xlabel('Time [s]');
ylabel('Amplitude [v]');
axis([0 5e-3 -0.015 0.015]);
set(gca,'ytick',-0.015:0.01:0.015);
legend('Microphone','location','best');
fontstyle('times new roman');

subplot(212);
plot(f_Mic/1e3,(abs(TRPv2)/max(abs(TRPv2))).^2,'b');
xlabel({'Frequency [kHz]','(b)'});
ylabel({'Normalized','Spectrum Amplitude'});
axis([0 40 0 1.5]);
text(12.5,1.1,'13.45kHz');
legend('Microphone','location','best');
fontstyle('times new roman');

set(gcf, 'PaperPositionMode', 'manual');
set(gcf, 'PaperUnits', 'inches');
set(gcf, 'PaperPosition', [1 1 4 3.5]);
print(figure(2), '-r600', '-dtiff', 'IE_test_PhysicalCoupled vs
AirCoupled_8x8deep2.tiff');

%% IE test on 12x12deep
```

```
clear all
close all
clc

Fs=1e6/2;
N=2048;
dt=1/Fs;
t=0:dt:(N-1)*dt;
i=sqrt(-1);
f_Acc_max=Fs/2;
f_Mic_max=Fs/2;
df=25;
f_Acc=0:df:f_Acc_max;
f_Mic=0:df:f_Mic_max;

% Acc_12x12 deep delamination
v1=xlsread('IE_test_Acc_120310_12x12deep.xlsx','sheet1','A2:A2049');
% Mic_12x12 deep delamination
v2=xlsread('IE_test_Mic_120310_12x12deep.xlsx','sheet1','A2:A2049');

for j=1:length(f_Acc)
    freq_Acc=f_Acc(j);
    Yv1=v1'.*exp(-i*2*pi*freq_Acc*t);
    TRPv1(j)=trapz(t,Yv1);
end;
for k=1:length(f_Mic)
    freq_Mic=f_Mic(k);
    Yv2=v2'.*exp(-i*2*pi*freq_Mic*t);
    TRPv2(k)=trapz(t,Yv2);
```

```
end;
% Find the maximum value of non-resonance frequency spectra for
accelerometer
a=abs(TRPv1);
b=a(:,1:1500);
[c,d]=max(b);
e=b(d-1);

figure(1)
subplot(211);
plot(t,v1,'b');
xlabel('Time [s]');
ylabel('Amplitude [v]');
axis([0 5e-3 -2 2]);
set(gca,'ytick',-2:1:2);
legend('Accelerometer');
fontstyle('times new roman');

subplot(212);
plot(f_Acc/1e3,(abs(TRPv1)/e).^2,'b');
xlabel({'Frequency [kHz]','(a)'});
ylabel({'Normalized','Spectrum Amplitude'});
axis([0 40 0 1.5]);
text(13.3,1.1,'14.23kHz');
legend('Accelerometer','location','northwest');
fontstyle('times new roman');

set(gcf, 'PaperPositionMode', 'manual');
set(gcf, 'PaperUnits', 'inches');
```

```
set(gcf, 'PaperPosition', [1 1 4 3.5]);
print(figure(1), '-r600', '-dtiff', 'IE_test_PhysicalCoupled vs
AirCoupled_12x12deep1.tiff');

figure(2)
subplot(211);
plot(t,v2,'b');
xlabel('Time [s]');
ylabel('Amplitude [v]');
axis([0 5e-3 -0.01 0.01]);
set(gca,'ytick',-0.01:0.005:0.01);
legend('Microphone','location','best');
fontstyle('times new roman');

subplot(212);
plot(f_Mic/1e3,(abs(TRPv2)/max(abs(TRPv2))).^2,'b');
xlabel({'Frequency [kHz]','(b)'});
ylabel({'Normalized','Spectrum Amplitude'});
axis([0 40 0 1.5]);
text(14.2,1.1,'15kHz');
legend('Microphone','location','best');
fontstyle('times new roman');

set(gcf, 'PaperPositionMode', 'manual');
set(gcf, 'PaperUnits', 'inches');
set(gcf, 'PaperPosition', [1 1 4 3.5]);
print(figure(2), '-r600', '-dtiff', 'IE_test_PhysicalCoupled vs
AirCoupled_12x12deep2.tiff');
```

```
%% IE test on Dia. 4in.
clear all
close all
clc

Fs=1e6/2;
N=2048;
dt=1/Fs;
t=0:dt:(N-1)*dt;
i=sqrt(-1);
f_Acc_max=Fs/2;
f_Mic_max=Fs/2;
df=25;
f_Acc=0:df:f_Acc_max;
f_Mic=0:df:f_Mic_max;

% Acc_Dia 4in. voids
v1=xlsread('IE_test_Acc_420120_Dia4.xlsx','sheet1','A2:A2049');
% Mic_Dia 4in. voids
v2=xlsread('IE_test_Mic_420120_Dia4.xlsx','sheet1','A2:A2049');

for j=1:length(f_Acc)
    freq_Acc=f_Acc(j);
    Yv1=v1'.*exp(-i*2*pi*freq_Acc*t);
    TRPv1(j)=trapz(t,Yv1);
end;
for k=1:length(f_Mic)
    freq_Mic=f_Mic(k);
    Yv2=v2'.*exp(-i*2*pi*freq_Mic*t);
```

```
    TRPv2(k)=trapz(t,Yv2);
end;

figure(1)
subplot(211);
plot(t,v1,'b');
xlabel('Time [s]');
ylabel('Amplitude [v]');
axis([0 5e-3 -3 3]);
set(gca,'ytick',-3:2:3);
legend('Accelerometer');
fontstyle('times new roman');

subplot(212);
plot(f_Acc/1e3,(abs(TRPv1)/max(abs(TRPv1))).^2,'b');
xlabel({'Frequency [kHz]','(a)'});
ylabel({'Normalized','Spectrum Amplitude'});
axis([0 40 0 1.5]);
text(5.8,1.1,'6.875kHz');
legend('Accelerometer','location','best');
fontstyle('times new roman');

set(gcf, 'PaperPositionMode', 'manual');
set(gcf, 'PaperUnits', 'inches');
set(gcf, 'PaperPosition', [1 1 4 3.5]);
print(figure(1), '-r600', '-dtiff', 'IE_test_PhysicalCoupled vs
AirCoupled_Dia41.tiff');

figure(2)
```

```
subplot(211);
plot(t,v2,'b');
xlabel('Time [s]');
ylabel('Amplitude [v]');
axis([0 5e-3 -0.01 0.01]);
set(gca,'ytick',-0.01:0.005:0.01);
legend('Microphone','location','best');
fontstyle('times new roman');

subplot(212);
plot(f_Mic/1e3,(abs(TRPv2)/max(abs(TRPv2))).^2,'b');
xlabel({'Frequency [kHz]','(b)'});
ylabel({'Normalized','Spectrum Amplitude'});
axis([0 40 0 1.5]);
text(5.5,1.1,'6.65kHz');
text(22.3,0.65,'23.23kHz');
legend('Microphone','location','best');
fontstyle('times new roman');

set(gcf, 'PaperPositionMode', 'manual');
set(gcf, 'PaperUnits', 'inches');
set(gcf, 'PaperPosition', [1 1 4 3.5]);
print(figure(2), '-r600', '-dtiff', 'IE_test_PhysicalCoupled vs
AirCoupled_Dia42.tiff');

%% IE test on Dia. 12in.
clear all
close all
clc
```

```
Fs=1e6/2;
N=2048;
dt=1/Fs;
t=0:dt:(N-1)*dt;
i=sqrt(-1);
f_Acc_max=Fs/2;
f_Mic_max=Fs/2;
df=25;
f_Acc=0:df:f_Acc_max;
f_Mic=0:df:f_Mic_max;

% Acc_Dia 12in. voids
v1=xlsread('IE_test_Acc_390320_Dia12.xlsx','sheet1','A2:A2049');
% Mic_Dia 12in. voids
v2=xlsread('IE_test_Mic_390320_Dia12.xlsx','sheet1','A2:A2049');

for j=1:length(f_Acc)
    freq_Acc=f_Acc(j);
    Yv1=v1'.*exp(-i*2*pi*freq_Acc*t);
    TRPv1(j)=trapz(t,Yv1);
end;
for k=1:length(f_Mic)
    freq_Mic=f_Mic(k);
    Yv2=v2'.*exp(-i*2*pi*freq_Mic*t);
    TRPv2(k)=trapz(t,Yv2);
end;
% Find the maximum value of non-resonance frequency spectra for
accelerometer
```

```
a=abs(TRPv1);
b=a(:,1:1500);
[c,d]=max(b);
e=b(d-1);

figure(1)
subplot(211);
plot(t,v1,'b');
xlabel('Time [s]');
ylabel('Amplitude [v]');
axis([0 5e-3 -1.5 1.5]);
set(gca,'ytick',-1.5:1:1.5);
legend('Accelerometer');
fontstyle('times new roman');

subplot(212);
plot(f_Acc/1e3,(abs(TRPv1)/e).^2,'b');
xlabel({'Frequency [kHz]','(a)'});
ylabel({'Normalized','Spectrum Amplitude'});
axis([0 40 0 1.5]);
text(5.75,1.1,'6.55kHz');
legend('Accelerometer','location','best');
fontstyle('times new roman');

set(gcf, 'PaperPositionMode', 'manual');
set(gcf, 'PaperUnits', 'inches');
set(gcf, 'PaperPosition', [1 1 4 3.5]);
print(figure(1), '-r600', '-dtiff', 'IE_test_PhysicalCoupled vs
AirCoupled_Dia121.tiff');
```

```
figure(2)
subplot(211);
plot(t,v2,'b');
xlabel('Time [s]');
ylabel('Amplitude [v]');
axis([0 5e-3 -0.02 0.02]);
set(gca,'ytick',-0.02:0.01:0.02);
legend('Microphone','location','best');
fontstyle('times new roman');

subplot(212);
plot(f_Mic/1e3,(abs(TRPv2)/max(abs(TRPv2))).^2,'b');
xlabel({'Frequency [kHz]','(b)'});
ylabel({'Normalized','Spectrum Amplitude'});
axis([0 40 0 1.5]);
text(5.5,1.1,'6.525kHz');
text(22.3,0.7,'23.1kHz');
legend('Microphone','location','best');
fontstyle('times new roman');

set(gcf, 'PaperPositionMode', 'manual');
set(gcf, 'PaperUnits', 'inches');
set(gcf, 'PaperPosition', [1 1 4 3.5]);
print(figure(2), '-r600', '-dtiff', 'IE_test_PhysicalCoupled vs
AirCoupled_Dia122.tiff');
```

```
%% Two-dimensional contour map
```

```
% Contour map of a 4in. x 4in. shallow delamination obtained by
accelerometer
clear all
close all
clc
load Acc_4x4Sshallow_rawdata.mat
[m, n]=size(Y);
plotintx=2;
plotinty=2;
figure(1)
surf(Y);
axis equal;
box off;
shading interp;
view(2);
hold on;
x=[3,7,7,3,3];
y=[4,4,8,8,4];
z=[20,20,20,20,20];
plot3(x,y,z,'k','linewidth',2.0);
axis equal;
set(gca,'xtick',1:plotintx:n,'xticklabel',54:2:62);
set(gca,'ytick',1:plotinty:m,'yticklabel',8:2:16);
xlabel('x [in]');
ylabel('y [in]');
colorbar('eastoutside');
h=colorbar;
set(get(h,'xlabel'),'string','Frequency [kHz]');
set(gca,'CLim',[2,16]);
```

```
colormap jet;
fontstyle('times new roman');

set(gcf, 'PaperPositionMode', 'manual');
set(gcf, 'PaperUnits', 'inches');
set(gcf, 'PaperPosition', [1 1 4 3]);
print(figure(1), '-r1200', '-dtiff', 'IE_test_2D scan of 4x4Sshallow_Acc.tiff');

%% Contour map of a 4in. x 4in. shallow delamination obtained by
microphone
clear all
close all
clc
load Mic_4x4shallow_rawdata.mat
[m, n]=size(Y);
plotintx=1;
plotinty=1;
figure(1)
surf(Y);
axis equal;
box off;
shading interp;
view(2);
hold on;
x=[2,4,4,2,2];
y=[2.5,2.5,4.5,4.5,2.5];
z=[20,20,20,20,20];
plot3(x,y,z,'k','linewidth',2.0);
axis equal;
```

```
set(gca,'xtick',1:plotintx:n,'xticklabel',54:2:62);
set(gca,'ytick',1:plotinty:m,'yticklabel',8:2:16);
xlabel('x [in]');
ylabel('y [in]');
colorbar('eastoutside');
h=colorbar;
set(get(h,'xlabel'),'string','Frequency [kHz]');
set(gca,'CLim',[2,16]);
colormap jet;
fontstyle('times new roman');

set(gcf, 'PaperPositionMode', 'manual');
set(gcf, 'PaperUnits', 'inches');
set(gcf, 'PaperPosition', [1 1 4 3]);
print(figure(1), '-r1200', '-dtiff', 'IE_test_2D scan of 4x4shallow_Mic.tiff');

%% Contour map of a 8in. x 8in. shallow delamination obtained by
accelerometer
clear all
close all
clc
load Acc_8x8shallow_rawdata.mat
[m, n]=size(Y);
plotintx=1;
plotinty=1;
figure(1)
surf(Y);
axis equal;
box off;
```

```
shading interp;
view(2);
hold on;
x=[3,7,7,3,3];
y=[2.5,2.5,6.5,6.5,2.5];
z=[20,20,20,20,20];
plot3(x,y,z,'k','linewidth',2.0);
axis equal;
set(gca,'xtick',1:plotintx:n,'xticklabel',36:2:52);
set(gca,'ytick',1:plotinty:m,'yticklabel',4:2:18);
xlabel('x [in]');
ylabel('y [in]');
colorbar('eastoutside');
h=colorbar;
set(get(h,'xlabel'),'string','Frequency [kHz]');
set(gca,'CLim',[2 16]);
colormap jet;
fontstyle('times new roman');

set(gcf, 'PaperPositionMode', 'manual');
set(gcf, 'PaperUnits', 'inches');
set(gcf, 'PaperPosition', [1 1 4 3]);
print(figure(1), '-r1200', '-dtiff', 'IE_test_2D scan of 8x8shallow_Acc.tiff');

%% Contour map of a 8in. x 8in. shallow delamination obtained by
microphone
clear all
close all
clc
```

```
load Mic_8x8shallow_rawdata.mat
[m, n]=size(Y);
plotintx=1;
plotinty=1;
figure(1)
surf(Y);
axis equal;
box off;
shading interp;
view(2);
hold on;
x=[3,7,7,3,3];
y=[2.5,2.5,6.5,6.5,2.5];
z=[20,20,20,20,20];
plot3(x,y,z,'k','linewidth',2.0);
axis equal;
set(gca,'xtick',1:plotintx:n,'xticklabel',36:2:52);
set(gca,'ytick',1:plotinty:m,'yticklabel',4:2:18);
xlabel('x [in]');
ylabel('y [in]');
colorbar('eastoutside');
h=colorbar;
set(get(h,'xlabel'),'string','Frequency [kHz]');
set(gca,'CLim',[2 16]);
colormap jet;
fontstyle('times new roman');

set(gcf, 'PaperPositionMode', 'manual');
set(gcf, 'PaperUnits', 'inches');
```

```
set(gcf, 'PaperPosition', [1 1 4 3]);
print(figure(1), '-r1200', '-dtiff', 'IE_test_2D scan of 8x8shallow_Mic.tiff');

%% Contour map of a 12in. x 12in. shallow delamination obtained by
microphone
clear all
close all
clc
load Mic_12x12shallow_rawdata.mat
[m, n]=size(Y);
plotintx=1;
plotinty=1;
figure(1)
surf(Y);
axis equal;
box off;
shading interp;
view(2);
hold on;
x=[3,9,9,3,3];
y=[2.5,2.5,8.5,8.5,2.5];
z=[20,20,20,20,20];
plot3(x,y,z,'k','linewidth',2.0);
axis equal;
set(gca,'xtick',1:plotintx:n,'xticklabel',16:2:36);
set(gca,'ytick',1:plotinty:m,'yticklabel',4:2:22);
xlabel('x [in]');
ylabel('y [in]');
colorbar('eastoutside');
```

```
h=colorbar;
set(get(h,'xlabel'),'string','Frequency [kHz]');
set(gca,'CLim',[2,16]);
colormap jet;
fontstyle('times new roman');

set(gcf, 'PaperPositionMode', 'manual');
set(gcf, 'PaperUnits', 'inches');
set(gcf, 'PaperPosition', [1 1 4 3]);
print(figure(1), '-r1200', '-dtiff', 'IE_test_2D scan of
12x12shallow_Mic.tiff');

%% Contour map of a 4in. x 4in. deep delamination obtained by
accelerometer
clear all
close all
clc
load Acc_4x4deep_rawdata.mat
[m, n]=size(Y);
plotintx=1;
plotinty=1;
figure(1)
surf(Y);
axis equal;
box off;
shading interp;
view(2);
hold on;
x=[2.125,4.125,4.125,2.125,2.125];
```

```
y=[2,2,4,4,2];
z=[18,18,18,18,18];
plot3(x,y,z,'k','linewidth',2.0);
axis equal;
set(gca,'xtick',1:plotintx:n,'xticklabel',54:2:64);
set(gca,'ytick',1:plotinty:m,'yticklabel',58:2:68);
xlabel('x [in]');
ylabel('y [in]');
colorbar('eastoutside');
h=colorbar;
set(get(h,'xlabel'),'string','Frequency [kHz]');
set(gca,'CLim',[2 16]);
colormap jet;
fontstyle('times new roman');

set(gcf, 'PaperPositionMode', 'manual');
set(gcf, 'PaperUnits', 'inches');
set(gcf, 'PaperPosition', [1 1 4 3]);
print(figure(1), '-r1200', '-dtiff', 'IE_test_2D scan of 4x4deep_Acc.tiff');

%% Contour map of a 4in. x 4in. deep delamination obtained by
microphone
clear all
close all
clc
load Mic_4x4deep_rawdata.mat
[m, n]=size(Y);
plotintx=1;
plotinty=1;
```

```
figure(1)
surf(Y);
axis equal;
box off;
shading interp;
view(2);
hold on;
x=[2.125,4.125,4.125,2.125,2.125];
y=[2,2,4,4,2];
z=[20,20,20,20,20];
plot3(x,y,z,'k','linewidth',2.0);
axis equal;
set(gca,'xtick',1:plotintx:n,'xticklabel',54:2:64);
set(gca,'ytick',1:plotinty:m,'yticklabel',58:2:68);
xlabel('x [in]');
ylabel('y [in]');
colorbar('eastoutside');
h=colorbar;
set(get(h,'xlabel'),'string','Frequency [kHz]');
set(gca,'CLim',[2 16]);
colormap jet;
fontstyle('times new roman');

set(gcf, 'PaperPositionMode', 'manual');
set(gcf, 'PaperUnits', 'inches');
set(gcf, 'PaperPosition', [1 1 4 3]);
print(figure(1), '-r1200', '-dtiff', 'IE_test_2D scan of 4x4deep_Mic.tiff');
```

```
%% Contour map of a 7.6in. x 5.8in. deep delamination obtained by
accelerometer
clear all
close all
clc
load Acc_7.6x5.8deep_rawdata.mat
[m, n]=size(Y);
plotintx=1;
plotinty=1;
figure(1)
surf(Y);
axis equal;
box off;
shading interp;
view(2);
hold on;
x=[2,5.625,5.625,2,2];
y=[2.5,2.5,5.5,5.5,2.5];
z=[15.5,15.5,15.5,15.5,15.5];
plot3(x,y,z,'k','linewidth',2.0);
axis equal;
set(gca,'xtick',1:plotintx:n,'xticklabel',40:2:52);
set(gca,'ytick',1:plotinty:m,'yticklabel',56:2:68);
xlabel('x [in]');
ylabel('y [in]');
colorbar('eastoutside');
h=colorbar;
set(get(h,'xlabel'),'string','Frequency [kHz]');
set(gca,'CLim',[2 16]);
```

```
colormap jet;
fontstyle('times new roman');

set(gcf, 'PaperPositionMode', 'manual');
set(gcf, 'PaperUnits', 'inches');
set(gcf, 'PaperPosition', [1 1 4 3]);
print(figure(1), '-r1200', '-dtiff', 'IE_test_2D scan of 8x8deep_Acc.tiff');

%% Contour map of a 7.6in. x 5.8in. deep delamination obtained by
microphone
clear all
close all
clc
load Mic_7.6x5.8deep_rawdata.mat
[m, n]=size(Y);
plotintx=1;
plotinty=1;
figure(1)
surf(Y);
axis equal;
box off;
shading interp;
view(2);
hold on;
x=[2,5.625,5.625,2,2];
y=[2.5,2.5,5.5,5.5,2.5];
z=[15.5,15.5,15.5,15.5,15.5];
plot3(x,y,z,'k','linewidth',2.0);
axis equal;
```

```
set(gca,'xtick',1:plotintx:n,'xticklabel',40:2:52);
set(gca,'ytick',1:plotinty:m,'yticklabel',56:2:68);
xlabel('x [in]');
ylabel('y [in]');
colorbar('eastoutside');
h=colorbar;
set(get(h,'xlabel'),'string','Frequency [kHz]');
set(gca,'CLim',[2 16]);
colormap jet;
fontstyle('times new roman');

set(gcf, 'PaperPositionMode', 'manual');
set(gcf, 'PaperUnits', 'inches');
set(gcf, 'PaperPosition', [1 1 4 3]);
print(figure(1), '-r1200', '-dtiff', 'IE_test_2D scan of 8x8deep_Mic.tiff');

%% Contour map of a 12in. x 12in. deep delamination obtained by
microphone
lear all
close all
clc
load Mic_12x12deep_rawdata.mat
[m, n]=size(Y);
plotintx=1;
plotinty=1;
figure(1)
surf(Y);
axis equal;
box off;
```

```
shading interp;
view(2);
hold on;
x=[3,9,9,3,3];
y=[2.5,2.5,8.5,8.5,2.5];
z=[15.11,15.11,15.11,15.11,15.11];
plot3(x,y,z,'k','linewidth',2.0);
axis equal;
set(gca,'xtick',1:plotintx:n,'xticklabel',15:2:35);
set(gca,'ytick',1:plotinty:m,'yticklabel',54:2:72);
xlabel('x [in]');
ylabel('y [in]');
colorbar('eastoutside');
h=colorbar;
set(get(h,'xlabel'),'string','Frequency [kHz]');
set(gca,'CLim',[2,16]);
colormap jet;
fontstyle('times new roman');

set(gcf, 'PaperPositionMode', 'manual');
set(gcf, 'PaperUnits', 'inches');
set(gcf, 'PaperPosition', [1 1 4 3]);
print(figure(1), '-r1200', '-dtiff', 'IE_test_2D scan of 12x12deep_Mic.tiff');

%% Contour map of a 4in. Dia. void obtained by microphone
clear all
close all
clc
load Mic_Dia4_rawdata.mat
```

```
[m, n]=size(Y);
plotintx=1;
plotinty=1;
figure(1)
surf(Y);
axis equal;
box off;
shading interp;
view(2);
hold on;
circle(2.75,2.75,18,1);
set(gca,'xtick',1:plotintx:n,'xticklabel',78:2:88);
set(gca,'ytick',1:plotinty:m,'yticklabel',20:2:28);
xlabel('x [in]');
ylabel('y [in]');
colorbar('eastoutside');
h=colorbar;
set(get(h,'xlabel'),'string','Freqeuncy [kHz]');
set(gca,'CLim',[2,16]);
colormap jet;
fontstyle('times new roman');

set(gcf, 'PaperPositionMode', 'manual');
set(gcf, 'PaperUnits', 'inches');
set(gcf, 'PaperPosition', [1 1 4 3]);
print(figure(1), '-r1200', '-dtiff', 'IE_test_2D scan of Dia4_Mic.tiff');

%% Contour map of a 12in. Dia. void obtained by microphone
clear all
```

```
close all
clc
load Mic_Dia12_rawdata.mat
[m, n]=size(Y);
plotintx=1;
plotinty=1;
figure(1)
surf(Y);
axis equal;
box off;
shading interp;
view(2);
hold on;
circle(5.25,5,18,3);
set(gca,'xtick',1:plotintx:n,'xticklabel',70:2:88);
set(gca,'ytick',1:plotinty:m,'yticklabel',56:2:72);
xlabel('x [in]');
ylabel('y [in]');
colorbar('eastoutside');
h=colorbar;
set(get(h,'xlabel'),'string','Frequency [kHz]');
set(gca,'CLim',[2,16]);
colormap jet;
fontstyle('times new roman');

set(gcf, 'PaperPositionMode', 'manual');
set(gcf, 'PaperUnits', 'inches');
set(gcf, 'PaperPosition', [1 1 4 3]);
print(figure(1), '-r1200', '-dtiff', 'IE_test_2D scan of Dia12_Mic.tiff');
```

```
%% A comparison of test results for the air-coupled, impact-echo test
between with and without band pass filter
clear all
close all
clc

% Global Definition
Fs=1e6/2;
N=2048;
dt=1/Fs;
t=0:dt:(N-1)*dt;
i=sqrt(-1);
df=50;
f_min=0e3;
f_max=Fs/2;
f=f_min:df:f_max;

% before bandpass filter
v1f=xlsread('IE_test_Mic_beforepassivefilter.xlsx','sheet1','A2:A2049'); %
Microphone only
v2f=xlsread('IE_test_Mic_500k_2048.xlsx','sheet1','A2:A2049'); %
Microphone+sound isolation
v3f=xlsread('IE_test_Mic+reflector_beforepassivefilter.xlsx','sheet1','A2:A20
49'); % Microphone+parabolic reflector
v4f=xlsread('IE_test_Mic+reflector+foam_beforepassivefilter.xlsx','sheet1','A
2:A2049'); % Microphone+parabolic reflector+foam

% bandpass filter
fN1=13e3/(Fs/2);
```

```
fN2=14.5e3/(Fs/2);
[B,A]=butter(3,[fN1,fN2],'bandpass');

% after bandpass filter
v1=filtfilt(B,A,v1f);
v2=filtfilt(B,A,v2f);
v3=filtfilt(B,A,v3f);
v4=filtfilt(B,A,v4f);

% before filter
for j=1:length(f)
    freq=f(j);
    Yv1f=v1f'.*exp(-i*2*pi*freq*t);
    TRPv1f(j)=trapz(t,Yv1f);
    Yv2f=v2f'.*exp(-i*2*pi*freq*t);
    TRPv2f(j)=trapz(t,Yv2f);
    Yv3f=v3f'.*exp(-i*2*pi*freq*t);
    TRPv3f(j)=trapz(t,Yv3f);
    Yv4f=v4f'.*exp(-i*2*pi*freq*t);
    TRPv4f(j)=trapz(t,Yv4f);
end;
% after filter
for j=1:length(f)
    freq=f(j);
    Yv1=v1'.*exp(-i*2*pi*freq*t);
    TRPv1(j)=trapz(t,Yv1);
    Yv2=v2'.*exp(-i*2*pi*freq*t);
    TRPv2(j)=trapz(t,Yv2);
    Yv3=v3'.*exp(-i*2*pi*freq*t);
```

```
    TRPv3(j)=trapz(t,Yv3);
    Yv4=v4'.*exp(-i*2*pi*freq*t);
    TRPv4(j)=trapz(t,Yv4);
end;

figure(1)
subplot(211);
plot(t,v1f,'b:');hold on;...
    plot(t,v1,'r');
xlabel('Time [s]');
ylabel('Voltage [v]');
legend('Before filter','After filter','location','best');
fontstyle('times new roman');

subplot(212);
a=abs(TRPv1f);
b=a(:,200:end);
c=max(b);
plot(f/1e3,(abs(TRPv1f)/c).^2,'b:');hold on;...
    plot(f/1e3,(abs(TRPv1)/max(abs(TRPv1))).^2,'r');
xlabel({'Frequency [kHz]','(a)'});
ylabel({'Normalized','Spectrum Amplitude'});
axis([0 40 0 1.5]);
text(12.5,1.1,'13.65kHz');
legend('Before filter','After filter');
fontstyle('times new roman');

set(gcf, 'PaperPositionMode', 'manual');
set(gcf, 'PaperUnits', 'inches');
```

```
set(gcf, 'PaperPosition', [1 1 4 3.5]);
print(figure(1), '-r600', '-dtiff', 'IE_test_Mic_BeforeFilter vs
AfterFilter_Mic.tiff');

figure(2)
subplot(211);
plot(t,v2f,'b:');hold on;...
   plot(t,v2,'r');
xlabel('Time [s]');
ylabel('Voltage [v]');
legend('Before filter','After filter','location','best');
fontstyle('times new roman');

subplot(212);
plot(f/1e3,(abs(TRPv2f)/max(abs(TRPv2f))).^2,'b:');hold on;...
   plot(f/1e3,(abs(TRPv2)/max(abs(TRPv2))).^2,'r');
xlabel({'Frequency [kHz]','(b)'});
ylabel({'Normalized','Spectrum Amplitude'});
axis([0 40 0 1.5]);
text(12.5,1.1,'13.5kHz');
legend('Before filter','After filter');
fontstyle('times new roman');

set(gcf, 'PaperPositionMode', 'manual');
set(gcf, 'PaperUnits', 'inches');
set(gcf, 'PaperPosition', [1 1 4 3.5]);
print(figure(2), '-r600', '-dtiff', 'IE_test_Mic_BeforeFilter vs
AfterFilter_MicIosolationEnclosure.tiff');
```

```
figure(3)
subplot(211);
plot(t,v3f,'b:');hold on;...
   plot(t,v3,'r');
xlabel('Time [s]');
ylabel('Voltage [v]');
legend('Before filter','After filter','location','best');
fontstyle('times new roman');

subplot(212);
plot(f/1e3,(abs(TRPv3f)/max(abs(TRPv3f))).^2,'b:');hold on;...
   plot(f/1e3,(abs(TRPv3)/max(abs(TRPv3))).^2,'r');
xlabel({'Frequency [kHz]','(c)'});
ylabel({'Normalized','Spectrum Amplitude'});
axis([0 40 0 1.5]);
text(12.5,1.1,'13.9kHz');
legend('Before filter','After filter');
fontstyle('times new roman');

set(gcf, 'PaperPositionMode', 'manual');
set(gcf, 'PaperUnits', 'inches');
set(gcf, 'PaperPosition', [1 1 4 3.5]);
print(figure(3), '-r600', '-dtiff', 'IE_test_Mic_BeforeFilter vs
AfterFilter_MicParabolicReflector.tiff');

figure(4)
subplot(211);
plot(t,v4f,'b:');hold on;...
   plot(t,v4,'r');
```

```
xlabel('Time [s]');
ylabel('Voltage [v]');
axis([0 5e-3 -0.04 0.04]);
set(gca,'ytick',-0.04:0.02:0.04);
legend('Before filter','After filter','location','best');
fontstyle('times new roman');

subplot(212);
plot(f/1e3,(abs(TRPv4f)/max(abs(TRPv4f))).^2,'b:');hold on;...
   plot(f/1e3,(abs(TRPv4)/max(abs(TRPv4))).^2,'r');
xlabel({'Frequency [kHz]','(d)'});
ylabel({'Normalized','Spectrum Amplitude'});
axis([0 40 0 1.5]);
text(12.5,1.1,'13.9kHz');
legend('Before filter','After filter');
fontstyle('times new roman');

set(gcf, 'PaperPositionMode', 'manual');
set(gcf, 'PaperUnits', 'inches');
set(gcf, 'PaperPosition', [1 1 4 3.5]);
print(figure(4), '-r600', '-dtiff', 'IE_test_Mic_BeforeFilter vs
AfterFilter_MicParabolicReflector&Foam.tiff');
```

```
%% A comparison of test results for the air-coupled, impact-echo test
between with and without high pass filter
clear all
close all
clc
```

```
Fs=1e6/2;
N=2048;
dt=1/Fs;
t=0:dt:(N-1)*dt;
i=sqrt(-1);
f_max=Fs/2;
df=25;
f=0:df:f_max;

v1f=xlsread('IE_test_Mic_130070_12x12shallow.xlsx','sheet1','A2:A2049');

% highpass filter
fN1=2e3/(Fs/2);
[B,A]=butter(3,fN1,'high');
v1=filtfilt(B,A,v1f);

for j=1:length(f)
   freq=f(j);
   Yv1f=v1f'.*exp(-i*2*pi*freq*t); % before filter
   TRPv1f(j)=trapz(t,Yv1f);
   Yv1=v1'.*exp(-i*2*pi*freq*t); % after filter
   TRPv1(j)=trapz(t,Yv1);
end;

figure(1)
subplot(211);
plot(t,v1f-v1f(1),'b:');hold on;...
   plot(t,v1-v1(1),'r');
xlabel('Time [s]');ylabel('Voltage [v]');
```

```
legend('Before filter','After filter');
fontstyle('times new roman');

subplot(212);
plot(f/1e3,(abs(TRPv1f)/max(abs(TRPv1f))).^2,'b:');hold on;...
   plot(f/1e3,(abs(TRPv1)/max(abs(TRPv1))).^2,'r');
xlabel('Frequency [kHz]');
ylabel('Normalized Spectrum Amplitude');
legend('Before filter','After filter','location','northeast');
text(1,1.3,'low-frequency noise');
axis([0 40 0 1.5]);
fontstyle('times new roman');

set(gcf, 'PaperPositionMode', 'manual');
set(gcf, 'PaperUnits', 'inches');
set(gcf, 'PaperPosition', [1 1 4 3.5]);
print(figure(1), '-r600', '-dtiff',
'IE_test_HighpassFilter__AirCoupled_12x12shallow.tiff');
```

APPENDIX B. LABVIEW CONTROL PROGRAM FOR IMPACT-ECHO TEST

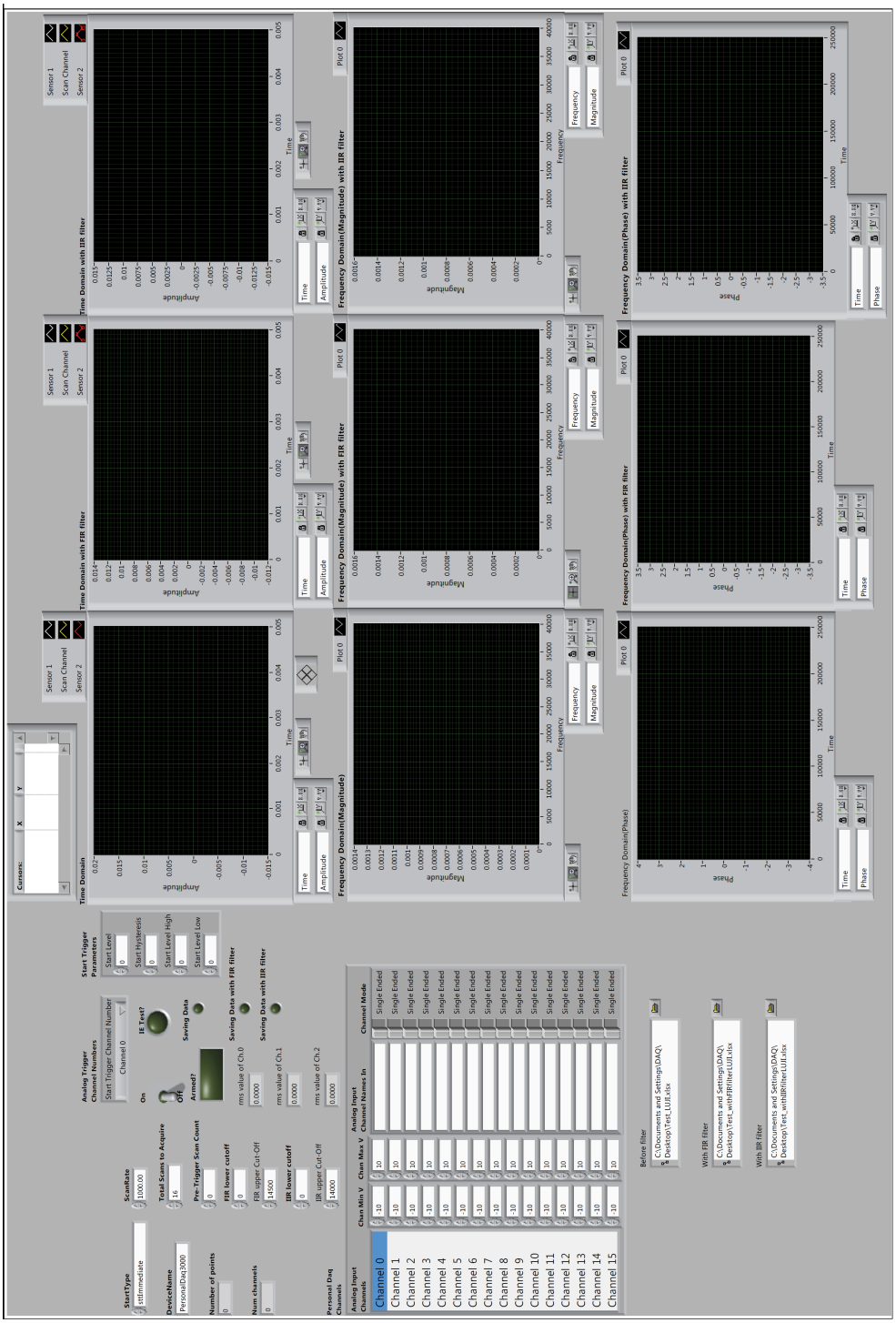

Figure B.1. Front panel of the LabVIEW control program.

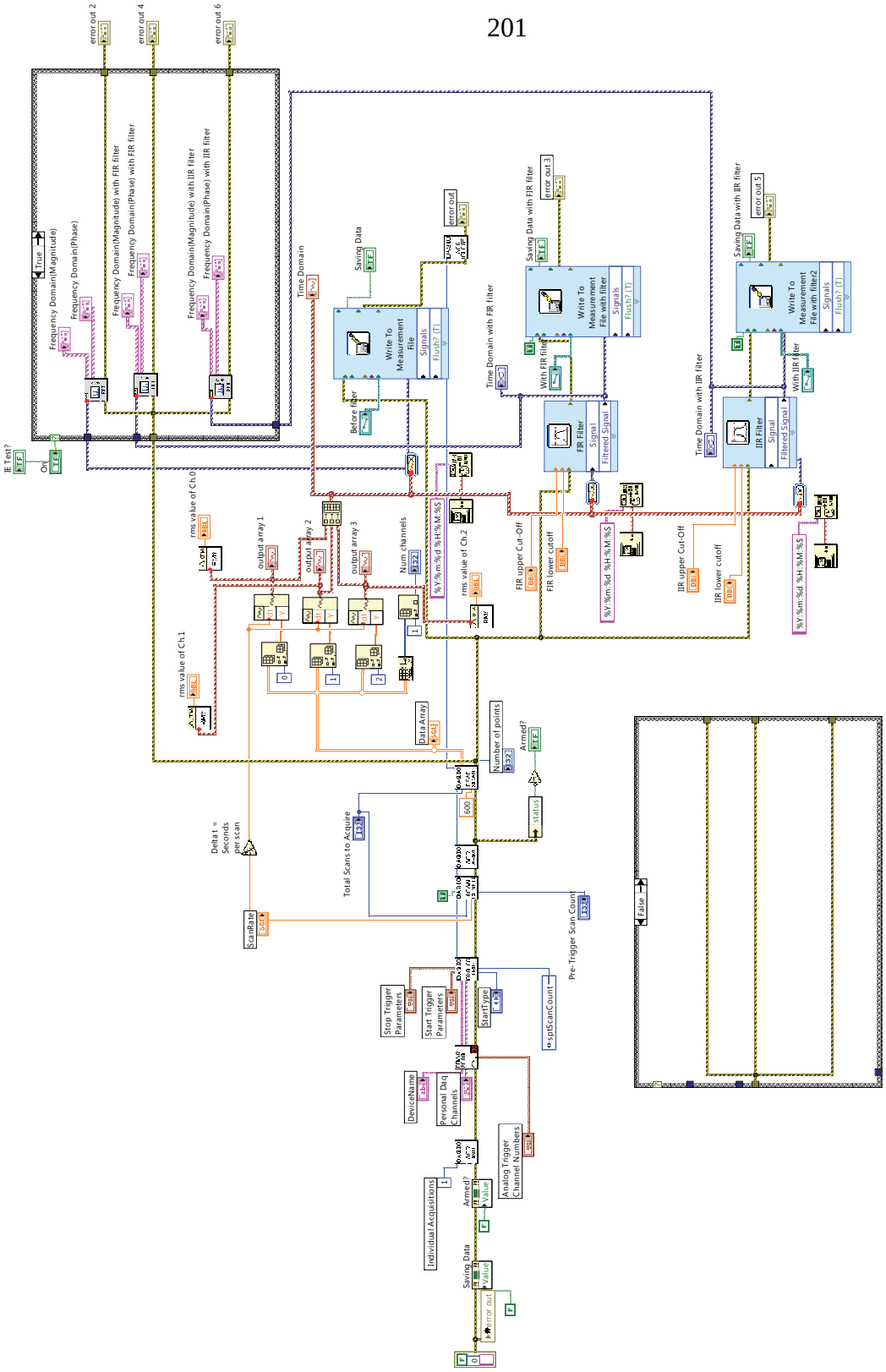

Figure B.2. Block diagram of the LabVIEW control program.